

國立交通大學
物 理 研 究 所
博 士 論 文

大亞灣反應堆微中子實驗宇宙射線導致之中子研究

Measurement of the Neutron Yield Induced by Cosmic
Muon in the Daya Bay Reactor Neutrino Experiment



指導教授：林貴林 教授

中 華 民 國 一 零 三 年 一 月

大亞灣反應堆微中子實驗宇宙射線導致之中子研究

研究 生：葉永順

Student: Yung-Shun Yeh

指 導 教 授：林貴林

Advisor: Guey-Lin Lin

國立交通大學
物 理 研 究 所
博 士 論 文

A Thesis
Submitted to Institute of Physics
National Chiao Tung University
in Partial Fulfillment of the Requirements
for the Degree of
Doctor in Philosophy
in
Physics
January, 2014
Hsinchu, Taiwan

中華民國一零三年一月

大亞灣反應堆微中子實驗宇宙射線導致之中子研究

學生：葉永順

指導教授：林貴林

國立交通大學物理研究所

摘要

宇宙射線渺子通過介質時所反應產生的快中子往往是地底實驗一個重要的背景。在大亞灣反應堆微中子實驗，微中子是透過反 β 衰變，產生一個正子與中子，正子與中子之後再與探測器反應產生快慢訊號。而快中子正好提供了一個假的慢訊號。為了了解宇宙射線渺子導致的中子產量，我們利用大亞灣實驗三個實驗大廳中的六個微中子探測器捕捉宇宙射線渺子導致中子。我們分析了從2011年12月24日到2012年07月28日的數據，得出宇宙射線渺子導致中子在三個實驗大廳的產量分別為： $(1.0510 \pm 0.0026) \times 10^{-4}$ 、 $(1.0165 \pm 0.0033) \times 10^{-4}$ 和 $(1.6845 \pm 0.0054) \times 10^{-4}$ ($n/\mu/(\text{g}/\text{cm}^2)$)。經由擬合大亞灣實驗與其他地底實驗的結果，我們可以得到擬合函數為 $Y_n = (7.45 \pm 1.03) \times 10^{-6} \times E_\mu^{0.64 \pm 0.03}$ ，其中 Y_n 是中子產量，單位是 $(n/\mu/(\text{g}/\text{cm}^2))$ ，而 E_μ 是平均渺子能量，單位是 GeV。

Measurement of the Neutron Yield Induced by Cosmic Muon in the Daya Bay Reactor Neutrino Experiment

Student: Yung-Shun Yeh

Advisor: Guey-Lin Lin

Submitted to Institute of Physics
National Chiao Tung University

ABSTRACT

The cosmogenic activation and the fast neutrons produced by cosmic-ray muons are very important sources of background for all underground low rate experiments, such as the Daya Bay reactor neutrino experiment. The Daya Bay experiment is the first experiment presenting a measurement of non-zero value for the neutrino mixing angle θ_{13} . To understand the muon-induced backgrounds in the Daya Bay experiment, the antineutrino detectors(ADs) deployed in three experimental halls (EHs) are served as the target. We analyze the data of 6 ADs in 3 EHs in a period of time from December 24, 2011 to July 28, 2012. Our measurement finds the neutron production rates: $(1.0510 \pm 0.0026) \times 10^{-4}$, $(1.0166 \pm 0.0033) \times 10^{-4}$, and $(1.6845 \pm 0.0054) \times 10^{-4}$ neutrons per muon per g/cm^2 in 3 EHs, respectively. The neutron production parameterization function can be obtained, $Y_n = (7.45 \pm 1.03) \times 10^{-6} \times E_\mu^{0.64 \pm 0.03} n/\mu / (\text{g/cm}^2)$, where Y_n is the neutron yield and E_μ is the mean muon energy in a unit of GeV.

誌謝

誌謝。

Contents

中文摘要	iii
Abstract	iv
誌謝	v
1 Introduction	1
1.1 Introduction to Neutrino Physics	1
1.2 Cosmic Muon-induced backgrounds	2
1.3 My Contributions to the Daya Bay Experiment	2
1.4 Thesis Outline	3
2 Neutrino Physics	5
2.1 Historical Introduction	5
2.2 Neutrino Oscillation	7
2.2.1 Standard deviation of neutrino oscillation probability	8
2.2.2 Two-neutrino mixing	11
2.2.3 Three-neutrino oscillation	13
2.3 Reactor Neutrinos	14
3 Daya Bay Reactor Neutrino Experiment	17
3.1 The Site Description	17
3.2 Antineutrino Detector	20
3.3 The Muon System	25

3.4	The Measurement of the Mixing Angle θ_{13}	27
3.4.1	Event selection and the efficiencies	27
3.4.2	Backgrounds	31
3.4.3	θ_{13} Analysis	38
4	Data Acquisition System	43
4.1	Hardware Architecture	43
4.2	Software Architecture	44
4.2.1	Data flow software	46
4.2.2	Readout system	47
4.2.3	Online software	48
4.2.4	Online database	49
4.3	The Automatic Controller	51
4.3.1	Automatic Controller in AD calibration	53
4.4	Status	56
5	Event Reconstruction of Antineutrino Detectors	59
5.1	PMT Calibration	60
5.1.1	Calibration using the low-intensity LED	60
5.1.2	Calibration using the dark noise	61
5.1.3	The fine gain calibration	63
5.2	Flasher Events	66
5.3	Vertex Reconstruction	68
5.3.1	Charge-weighted mean with an empirical correction	68
5.3.2	Charge templates	70
5.4	Energy Reconstruction	71
5.4.1	Calculation of the total charge	71
5.4.2	Visible energy	71
5.4.3	The non-uniformity correction	73
5.4.4	Energy resolution	75

6 Muon-induced Neutron	77
6.1 Neutron Production	77
6.2 Simulation Setup	79
6.2.1 Muon simulation	79
6.2.2 Simulation of neutron production and transportation	83
6.3 Measurement of muon-induced neutron production	91
6.3.1 The neutron yield	93
6.3.2 Comparison with results from other experiments	112
7 Conclusion	113

List of Figures

2.1	The beta ray spectrum of Radium E (called ^{210}Bi today), which is measured in 1935 by Scott [1].	6
2.2	The transition probability of $\nu_\alpha \rightarrow \nu_\beta$ with $\sin^2 2\theta = 1$ as a function of $\langle L/E \rangle$. The green curve indicates a unaveraged transition probability; while the blue one indicates the smeared transition probability with $\sigma_{L/E} = 0.2 \langle L/E \rangle$	12
3.1	Layout of the Daya Bay experiment.	18
3.2	The disappearance probability of $\bar{\nu}_e$, as a function of the distance between the reactor core and the detector. The blue and the green curves represent the contribution from θ_{13} and θ_{12} respectivley, while the red curve shows the sum of these two.	19
3.3	Schematic of the Daya Bay near hall (EH1) including the ADs, water shields, and RPCs.	21
3.4	Schematic drawing of the antineutrino detector.	22
3.5	The 3D model of the MCS installed on the AD.	24
3.6	Schematic drawing of an RPC module structure.	26
3.7	Prompt energy spectrum from EH1-AD1.	29
3.8	Delayed energy spectrum from EH1-AD1.	30
3.9	Prompt energy spectrum of IBD candidates with the upper limit relaxed. The energy spectrum of the fast neutron backgrounds tagged by the OWS muons or RPC-only muons is shown in the inset.	32

3.10 An example of the time distribution of the ${}^9\text{Li}/{}^8\text{He}$ background since the last muon	34
3.11 The fitted ${}^9\text{Li}$ yield as a function of the muon deposited energy in the 3 EHs. The open circles represent the fit with all muons included. Due to high muon rate, the fit is done only for $E_\mu > 2.5$ GeV. The filled circles are the results obtained by requiring a neutron following the muon as described in the text. In the bottom panel the prediction from the near site measurements is shown as a solid line.	35
3.12 Top: Measured prompt energy spectrum of the far hall (sum of ADs) compared with the no-oscillation prediction based on the measurements of the near halls. Bottom: the ratio of measured and predicted spectrum. Red curve indicates the best fit with $\sin^2 2\theta_{13} = 0.089$; while the dashed curve is the non-oscillation prediction.	38
3.13 Ratio of measured versus expected signals in each detector, assuming no oscillation.	40
3.14 The measured daily IBD rate per AD in the three experimental halls.	41
4.1 The hardware architechure of the DAQ.	45
4.2 The structure of the DAQ software.	45
4.3 the data flow component diagram in DAQ software.	46
4.4 The interaction between the online software packages.	49
4.5 The java-based GUI of DAQ for the onsite shifter.	50
4.6 The web-based GUI of DAQ for the remote shifter.	50
4.7 Example shows the table which store run number information.	51
4.8 The web interface of the online database.	52
4.9 The relationship of the AutoCtrl, DIM, and sub-packages in DAQ . .	53
4.10 The communication protocol between AutoCtrl and ACU.	54

4.11	The live times in 3 EHs. The light green region was the data used for this analysis.	57
5.1	A flowchart showing the steps of event reconstruction in the AD.	60
5.2	The occupancies of 192 PMTs at AD1 in an LED calibraiton run.	61
5.3	TDC distribution of a PMT in a LED calibration run. The blue lines indicate the selection region.	62
5.4	A typical TDC distribution of a PMT. The vertical line indicates the noise region in which the the dark noise is selected.	63
5.5	Fit to a single PMT SPE distribution using the realistic PMT response function after subtracting the preADC. Dashed curves show the SPE and double PE components. The units are in raw ADC counts.	65
5.6	Distribution of SPE peaks (Q_1) for AD1 and AD2.	65
5.7	The stability of the peak in the SPE distributions averaged in AD1 and AD2 using the calibration data taken in a period of three months.	66
5.8	An example showing the flasher charge pattern.	67
5.9	Discrimination of flasher events ($FID > 0$) and IBD delayed signals ($FID < 0$). The delayed signals of IBDs have the same distribution for all six ADs while the flashers are different. The $FID < 0$ distributions have been scaled to equal area.	68
5.10	Distributions of ΔR (left) and ΔZ (right).	69
5.11	Examples for charge distribution for each PMT. The left figure shows the distribution for $0.2 < r^2 < 0.4(m^2)$ and $-1.2 < z < -1.0(m)$ and the right one shows that for $3.0 < r^2 < 3.2(m^2)$ and $0.8 < z < 1.0(m)$	70
5.12	Gd-capture neutron peak fitted with a double Crystal Ball function. The red curve is the fitting result of ^{155}Gd , while the blue one is that of ^{157}Gd . The black one is the sum of those two.	73

5.13	The variation of E_{vis} for the ^{60}Co sources as a function of position in ADs. The charge ratio denotes $E_{vis}(Z)/E_{vis}(Z = 0)$. The R -positions of each ACU are 0 m (ACU A), 1.35 m (ACU B), and 1.77 m (ACU C).	74
5.14	The variation of E_{rec} for the ^{60}Co sources as a function of position in ADs. The charge ratio denotes $E_{rec}(Z)/E_{rec}(Z = 0)$. The R -positions of each ACU are 0 m (ACU A), 1.35 m (ACU B), and 1.77 m (ACU C).	75
5.15	Resolution of reconstructed energy.	76
6.1	The Feynman diagram of a muon spallation process.	78
6.2	The 3D topographic map of the Daya Bay area. The tunnel entrance is at the base of the mountain at the left side of the figure.	80
6.3	Simulated muon trajectories. The upper figure shows the cosine distribution of zenith angle; while the bottom figure shows the azimuthal angular distribution.	81
6.4	Simulated muon energy distributions.	82
6.5	The fitting of the $\pi - k$ model to the data of MINOS and L3+C [44].	83
6.6	The scheme of the FLUKA simulation. Muons are injected into a cylinder filled with Gd-doped liquid scintillator.	85
6.7	The neutron production rate as a function of muon track length. We injected 25 million muons with realistic spectrum for this simulation. Neutron samples are selected in the shadow region.	86
6.8	The kinetic energy spectrum of muon-induced neutron in EH1. . . .	87
6.9	The angular distribution of muon-induced neutron in EH1. The angle is relative to the muon direction.	87
6.10	The lateral profile for neutron produced by cosmic muons in a liquid scintillator in EH1.	89
6.11	The illustration of muon-induced neutron captured on Gd	91

6.12 A 2D map showing the time since the last muon versus the energy of the spallation products.	92
6.13 The deposited energy spectrum of muon candidates in EH3-AD3. The red curve indicates the fitted function.	94
6.14 The energy spectra between 0 and 20 MeV before and after cuts in EH1-AD1. Black curve indicates the energy spectrum of all triggers; Blue curve indicates the energy spectrum for events located in the signal time window of an isolated muon; Red curve indicates the en- ergy spectrum for events passing the the flasher removal cut; Green curve indicates the energy spectrum after the side-band subtraction. .	96
6.15 The spatial distributions of the nGd candidates in the singal and background time windows.	97
6.16 The energy spectrum of nGd after the selection cuts in EH1-AD1. .	98
6.17 The energy spectrum in EH1-AD1 with a logarithmic scale on y axis.	100
6.18 The MC simulation of muon track length in EH1-AD1.	101
6.19 The <i>FID</i> distribution from the MC simulation. The red dashed vertical line indicates <i>FID</i> = 0.	104
6.20 The capture time distribution in MC data.	105
6.21 The capture time distribution in the data of EH1-AD1.	106
6.22 The capture time constants in the 6 ADs.	107
6.23 The energy spectrum of nGd in EH1 in MC.	108
6.24 The neutron yields in 6 ADs of 3 EHs. For visual clarity, the ADs in EH1 and EH3 are separated by 1 GeV. The red curve indicates the parameterization formula obtained by FLUKA simulation [46], and the blue curve is from GEANT4 simulation [14].	111

6.25 Measurement of the neutron production rate as a function of the mean muon energy. The experimental points, with abscissa corresponding to the average energy at the experiment's depth: A) 20 meter water equivalent (m.w.e.) [67], B) 32 m.w.e by the Palo Verde experiment[68] C) 25 m.w.e. [69], D) 316 m.w.e. [69], E) 570 m.w.e [70], F) 2700 m.w.e by KamLAND experiment [71], G) 3650 m.w.e. by the LVD experiment at Gran Sasso [65], H) 3800 m.w.e by the Borexino experiment at Gran Sasso [66], I) 5200 m.w.e. by the LSD detector at Mont Blanc [72] and the data points from the Daya Bay experiment. The black curve is the fitted function. Our measurements are denoted by DYB Near and DYB Far, respectively. 112

List of Tables

3.1	Site information including baselines and overburdens. D1/D2, L1/L2, and L3/L4 mean the reactor cores and Figure 3.1 shows the layout.	20
3.2	Lists of calibration sources. (*) indicates the energy of capture gammas.	25
3.3	Summary of absolute efficiencies, and correlated and uncorrelated systematic uncertainties.	28
3.4	Summary of signal and background in ADs in the 3 EHs.	37
4.1	The performance of the readout systems in EH1.	47
4.2	The summary of running types of ROSs in differnt run modes. “Y” indicates that this detector works according to the run mode.	48
4.3	The parameters and status that are exchanged between the DAQ and ACU sides.	55
4.4	Summary of the event rates in the 3 EHs.	56
5.1	caption	72
6.1	The overburden (m w.e.), the muon flux R_μ (Hz/m ²) and the average energy E_μ (GeV) of the 3 EHs from MUSIC simulation.	81
6.2	The composition of Gd-doped LS.	85
6.3	The number of the isolated muon candidates in the ADs of 3 EHs. σ_{stats} indicates the statistical uncertainty, while σ_{syst} indicates the systematic uncertainty due to the errors from the fitted function.	95

6.4	The number of nGd candidates in the ADs of the 3 EHs. σ_{stats} indicates the statistical uncertainty.	98
6.5	The average energy loss per unit track length for cosmic-ray muons in the 3 EHs	100
6.6	The average track lengths of muon in the 3 EHs.	101
6.7	The spill in/out correction factors in the 3 EHs. $\overline{C_{in/out}}$ denotes the spill in/out correction factor. σ_{stats} indicates the statistical uncertainty, σ_{syst} indicates the systematical uncertainty by comparing results obtained from two methods.	103
6.8	The Gd-capture ratio using two different methods, where ϵ_{Gd} and σ_{Gd} are Gd-capture efficiency and the associated statistical uncertainty.	103
6.9	The timing cut efficiencies in the 3 EHs. σ_{stat} , σ_{abs_syst} , and σ_{rel_syst} denote the statistical, absolute systematic and relative systematic uncertainties, respectively.	107
6.10	The ratio of events in a subset region to that in 6-12 MeV.	109
6.11	The energy cut efficiencies in the 3 EHs. σ_{stat} , σ_{abs_syst} , and σ_{rel_syst} denote the statistical, absolute systematic and relative systematic uncertainties, respectively.	109
6.12	Summary of muon-induced neutrons in ADs in the 3 EHs.	110
6.13	The neutron production rate in the 6 ADs of the 3 EHs. Y_n , σ_{stat} and σ_{syst} denote the neutron yield, statistical and systematic uncertainties. The uncertainties are also in unit of $n/\mu/(g/cm^2)$	110
7.1	Summary of the neutron yield in the 3 EHs where the overburden is given in the unit of m w.e., the average energy of muon E_μ is given in the unit of GeV and the neutron yield is given in the unit of $n/\mu/(g/cm^2)^2$	113

Chapter 1

Introduction

1.1 Introduction to Neutrino Physics

Neutrino, which has been considered one of fundamental particles, plays a very important role in both microscopic view of particle physics and the macroscopic view of the evolution of the Universe. The last decade has seen a tremendous advance in the understanding of the neutrino sector. There is now a robust evidence for neutrino flavor conversion from solar, atmospheric [3, 4], reactor [7, 8] and accelerator [5, 6] experiments, using a wide variety of detector technologies. The only consistent explanation for these results is that neutrinos are massive and that the neutrino mass eigenstates are not the same as the flavor eigenstates (neutrino mixing). Neutrino oscillations depend on two mass-squared differences and three neutrino mixing angles and one CP violation phase δ_{cp} . Two of the mixing angles θ_{12} and θ_{23} , and the mass-squared differences have been measured with reasonable precision by solar, atmospheric, reactor and accelerator neutrino experiments.

The Daya Bay Reactor Neutrino Experiment [33] is designed to perform a precision measurement of the last mixing angle θ_{13} by searching for the disappearance of electron antineutrinos from the nuclear reactor complex in Daya Bay, Shenzhen, China. In March 2012, the Daya Bay discovered a non-zero θ_{13} with a significance of 5.2 standard deviations [22]. In May, the Daya Bay experiment published an

improved measurement on θ_{13} that $\sin^2 2\theta_{13} = 0.089 \pm 0.010(\text{stat.}) \pm 0.005(\text{syst.})$ in rate-only analysis [45].

1.2 Cosmic Muon-induced backgrounds

Radioactive isotopes produced through cosmic muon spallation are backgrounds for rare-event detection in ν detectors, double β decay experiments, and dark-matter searches. Understanding the nature of cosmogenic backgrounds is essential for underground experiments, such as the Daya Bay experiment. In this thesis, the cosmic muon-induced neutron production rate is discussed. To detect the muon-induced neutrons in the Daya Bay experiment, the Gadolinium-doped liquid scintillator (GdLS) region in the antineutrino detectors (ADs) deployed in the 3 experimental halls are served as the target. The neutrons produced by cosmic-ray muons, after thermalized in a few microseconds, are captured on Gd in the GdLS region. The detection efficiencies and their uncertainties are carefully calculated. The average track length of the cosmic muon inside the AD as it passes through the detector is statistically estimated by Monte Carlo (MC) simulation and its uncertainty is given by comparing the simulated track length with that inferred from the average muon deposited energy in the AD. The measurement of neutron yield will be presented in Chapter 6.

1.3 My Contributions to the Daya Bay Experiment

During the construction stage of the Daya Bay experiment, one of my major contribution is to develop the data acquisition system (DAQ). The online software of Daya Bay DAQ is migrated from ATLAS Trigger/DAQ [37] and modified to fit with the requirements of Daya Bay DAQ. The online database, served as a storage of non-data information is set up by using MySQL [35] database server. I also

developed an automatic controller of DAQ to work with external subsystems, such as automatic calibration unit (ACU) in AD.

I also involve the fabrication of the inner acrylic vessel (IAV) and the installation of the AD. the characterization measurements of the IAVs are performed during the fabrication. the IAVs are cleaned before the delivery to onsite and during the installation of the AD to remove possible radioactivity isotopes from environmental dusts.

After assembly of the AD and before filling liquids, an LED calibration data (dry run) is taken to see if all subsystems work well with each other. During the dry run, I perform the gain calibrations of PMTs in AD to make sure PMTs in AD working normally. To comparing MC and experimental data, I perform gain calibrations of PMTs with MC data.

For the physics analysis, I measure the muon-induced neutron production rate at 3 EHs. In this analysis, the number of detected muons and spallation neutrons are selected based on the selection criteria. The average muon track lengths in AD are obtained by the MC simulation and the uncertainties are given by comparing the simulated track length with that inferred from the average muon deposited energy in the AD. A semi-realistic MC simulation is done for calculating the detection efficiencies, the correction factors and the relevant uncertainties.

1.4 Thesis Outline

Chapter 2 begins with a historic introduction of neutrino physics and the theory of neutrino mixing. Two-neutrino and three-neutrino mixings are both discussed. At the end of Chapter 2, the physics of reactor neutrino is described.

In Chapter 3, we introduce the Daya Bay Reactor Neutrino Experiment. The layout of the experiment is presented at first. The design of detectors, including antineutrino detectors and the muon veto systems are introduced. At the end of this chapter, we discuss the updated measurement on the neutrino mixing angle θ_{13} .

Chapter 4 shows the architecture of the data acquisition system. The hardware and software perspectives are both introduced. The automatic controller of DAQ to work with external subsystems is introduced, too. The status of DAQ is presented at the end.

Chapter 5 gives a description of the PMT gain calibration and the event reconstruction. At beginning, the technique of the PMT gain calibration is discussed. The removal of the instrumental backgrounds is also discussed. At the end, the event reconstruction, including energy and vertex reconstructions are presented.

In Chapter 6, we turn to the muon-induced neutron study. At first, the production mechanisms of muon-induced neutron are introduced. We then introduce the simulation setup which can be separated into two parts: muon and spallation simulations. The measurement of the muon-induced neutron production is presented in Section 6.3. The number of detected neutron and muon, correction factors and the efficiencies, as well as the relevant uncertainties are discussed in Section 6.3. We present a comparison between our results and those from other experiments at the end.

The measurements of the cosmic muon-induced neutron are summarised in the concluding chapter.

Chapter 2

Neutrino Physics

2.1 Historical Introduction

Neutrino was first postulated in 1930 by Wolfgang Pauli to explain the continuous energy spectrum of electron in β decay observed by James Chadwick in 1914. At that time, the process of β decay was understood as a neutron decaying into a proton plus an electron (β particle).

$$n \rightarrow p + \beta^- \quad (2.1)$$

However, if the β decay is simply a two-body decay, the emitting β particle should have a fixed energy, just like α and γ spectra. Figure 2.1 gives an example of the beta decay energy spectrum and it shows the spectrum is continuous. To explain the continuous energy spectrum of β particle, N. Bohr even suggested that the conservation of energy is held only in statistical sense.

To remedy the energy conservation law and explain the spin statistics in β decay, Pauli wrote an open letter [2] to a physics conference in Tubingen. He proposed that there exists a neutral weakly interacting fermion, which we called “neutrino” today, participating in β decay.

In 1934, E. Fermi established his theory on weak interaction which also de-

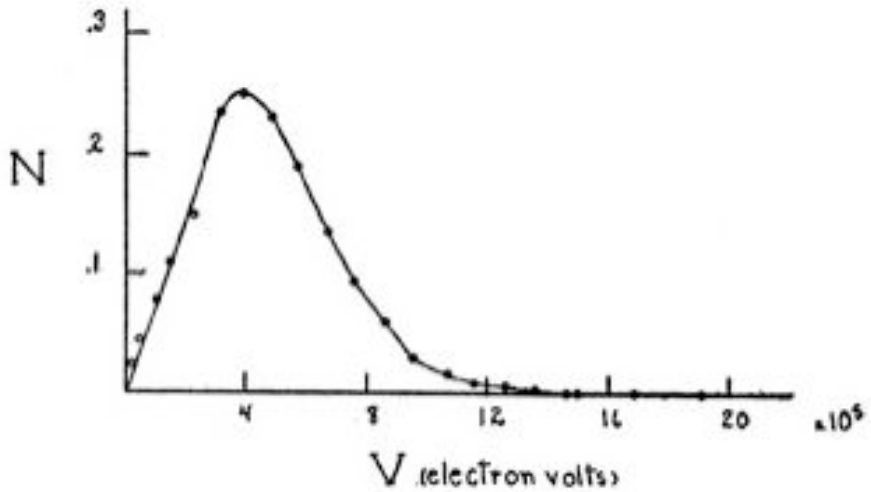


Figure 2.1: The beta ray spectrum of Radium E (called ${}^{210}\text{Bi}$ today), which is measured in 1935 by Scott [1].

scribes the interaction of neutrino. Based on Fermi's theory, H. Bethe and R. Peierls claimed that neutrino might never be observed due to the extremely small cross sections.

The detection of neutrinos was thought to be impossible until F. Reines and C. Cowan in 1956 detected the electron antineutrino ($\bar{\nu}_e$) from reactor cores by measuring the inverse β decay [23]. The second type of neutrino, muon neutrino, was later discovered by L. M. Lederman, M. Schwartz, J. Steinberger using accelerator beam in 1962 [24]. The third neutrino in the Standard Model, ν_τ was not directly detected until 2000 by DONUT collaboration [25].

In the late 1960s, the Homestake experiment measured the flux of neutrino from Sun and found a deficit between experimental data and theoretical prediction [26]. The solar neutrino rate measured by Homestake is about 1/3 of the prediction from the Standard Solar Model, with a discrepancy more than 3σ . This discrepancy, so called the solar neutrino problem (SNP), was later confirmed by other experiments. In 2001, the SNO experiment demonstrated that the SNP can be explained by the theory of neutrino mixing which implies that neutrinos are massive [27].

The atmospheric neutrinos was first regarded as unwanted background for the

experiments that had been designed to search proton decay. In the late 1980s, the larger underground Kamiokande [28] and IMB [29] water Cherenkov experiments observed a number of atmospheric muon neutrino events which was significantly smaller than the predicted event number. This deficit was referred to as the atmospheric neutron anomaly for many years. The Super-Kamiokade [4] experiment established that the atmospheric neutrino anomaly is due to the $\nu_\mu - \nu_\tau$ oscillation.

In the past decade, the results from atmospheric, solar, KamLAND [7], and K2K [5] neutrino experiments can be nicely explained by the theory of neutrino oscillation within the framework of three types of neutrinos. The rather precise measurements are done on the neutrino mixing angle θ_{12} and θ_{23} , the values of neutrino mass differences Δm_{21}^2 and $|\Delta m_{31}^2|$. We only have an upper bound on the last neutrino mixing angle θ_{13} set by the reactor long-baseline experiments Chooz [15] and Palo Verde [16] until Double Chooz [19] and T2K [18] experiments give implications of non-zero θ_{13} . In March 2012, the Daya Bay experiment publishes a non-zero measurement on the mixing angle θ_{13} with a significance of 5.2 standard deviations [22] and the result from RENO experiment [17] shows a good agreement with that of Daya Bay experiment.

2.2 Neutrino Oscillation

Neutrino oscillation is a quantum mechanical phenomenon proposed in 1950s by Pontecorvo in analogy with $K^0 - \bar{K}^0$ oscillations. The oscillations are generated by the interference of different massive neutrinos, which are produced and detected coherently because of their very small mass differences. At that time, there are only one active neutrino known, the electron neutrino. Pontecorvo's neutrino oscillation was between neutrino and sterile neutrino [20], which does not participate the weak interaction. After discovering muon neutrino in 1962, Maki, Nakagawa, and Sakata extended the Pontecorvo's idea to incorporate the transition between different neutrino flavors [21].

2.2.1 Standard deviation of neutrino oscillation probability

The underlying principle for neutrino oscillation is that that neutrino weak eigenstates do not correspond to the neutrino mass eigenstates, but are mixture of each other.

$$|\nu_\alpha\rangle = \sum_{i=1}^3 U_{\alpha i}^* |\nu_i\rangle \quad (\alpha = e, \mu, \tau) \quad (2.2)$$

where U is 3×3 unitary matrix known as the Pontecorvo-Maki-Nakagawa-Sakata (PMNS) mixing matrix. $|\nu_\alpha\rangle$ represents the weak eigenstate, and $|\nu_i\rangle$ is the mass eigenstate. The massive neutrino states $|\nu_i\rangle$ are eigenstates of the Hamiltonian,

$$\mathcal{H}|\nu_i\rangle = E_k |\nu_i\rangle \quad (2.3)$$

with energy eigenvalues

$$E_i = \sqrt{\vec{p}^2 + m_i^2}. \quad (2.4)$$

From the Schrödinger equation

$$i \frac{d}{dt} |\nu_k(t)\rangle = \mathcal{H} |\nu_k(t)\rangle, \quad (2.5)$$

we can get that the massive neutrino states evolve in time as plane waves

$$|\nu_k(t)\rangle = e^{-iE_k t} |\nu_k\rangle \quad (2.6)$$

Because neutrino are produced and detected as flavor eigenstates. we consider a flavor state $|\nu_\alpha(t)\rangle$ which describes a neutrino created with a definite flavor α at time $t = 0$. From Equation 2.2 and Equation 2.6, we can get the time evolution of this state

$$|\nu_\alpha(t)\rangle = \sum_k U_{\alpha k}^* e^{-iE_k t} |\nu_k\rangle. \quad (2.7)$$

such that

$$|\nu_\alpha(t=0)\rangle = |\nu_\alpha\rangle. \quad (2.8)$$

From the unitary relation of Equation 2.2, the massive eigenstates can be expressed in terms of flavor eigenstates by inverting Equation 2.2,

$$|\nu_k\rangle = \sum_k U_{\alpha k} |\nu_\alpha\rangle. \quad (2.9)$$

Substituting Equation 2.9 into Equation 2.7, we obtain

$$|\nu_\alpha(t)\rangle = \sum_{\beta=e,\nu,\tau} \left(\sum_k U_{\alpha k}^* e^{-iE_k t} U_{\beta k} \right) |\nu_\beta\rangle. \quad (2.10)$$

Equation 2.10 shows that the pure flavor state at $t = 0$ becomes a superposition of different flavor states at $t > 0$. If the mixing matrix U is not diagonal, neutrinos are mixed. The transition amplitude of $\nu_\alpha \rightarrow \nu_\beta$ as a function of time is given by

$$A_{\nu_\alpha \rightarrow \nu_\beta}(t) \equiv \langle \nu_\beta | \nu_\alpha(t) \rangle = \sum_k U_{\alpha k}^* U_{\beta k} e^{-iE_k t}. \quad (2.11)$$

The transition probability is then,

$$P_{\nu_\alpha \rightarrow \nu_\beta}(t) = |A_{\nu_\alpha \rightarrow \nu_\beta}(t)|^2 = \sum_{k,j} U_{\alpha k}^* U_{\beta k} U_{\alpha j}^* U_{\beta j} e^{-i(E_k - E_j)t}. \quad (2.12)$$

For ultrarelativistic neutrinos, Equation 2.3 can be approximated by

$$E_k \simeq E + \frac{m_k^2}{2E}, \quad (2.13)$$

where $E = |\vec{p}|$ is the neutrino energy neglecting the contribution of mass. The difference of energy between two massive neutrinos can be expressed as

$$E_k - E_j \simeq \frac{\Delta m_{kj}^2}{2E}, \quad (2.14)$$

where Δm_{kj}^2 is the squared-mass difference

$$\Delta m_{kj}^2 \equiv m_k^2 - m_j^2. \quad (2.15)$$

The transition probability in Equation 2.12 can be approximated as

$$P_{\nu_\alpha \rightarrow \nu_\beta}(t) = |A_{\nu_\alpha \rightarrow \nu_\beta}(t)|^2 = \sum_{k,j} U_{\alpha k}^* U_{\beta k} U_{\alpha j}^* U_{\beta j} \exp\left(-i \frac{\Delta m_{kj}^2 L}{2E}\right). \quad (2.16)$$

In neutrino oscillation experiments, the propagation time t is not measured, and what we know is the distance L between the source and the detector. By approximating $t = L$ for ultrarelativistic neutrinos, the transition probability can be expressed as

$$P_{\nu_\alpha \rightarrow \nu_\beta}(L, E) = |A_{\nu_\alpha \rightarrow \nu_\beta}(t)|^2 = \sum_{k,j} U_{\alpha k}^* U_{\beta k} U_{\alpha j}^* U_{\beta j} \exp\left(-i \frac{\Delta m_{kj}^2 L}{2E}\right). \quad (2.17)$$

The oscillation probabilities of the channels with $\alpha \neq \beta$ are usually called transition probabilities. For channels with $\alpha = \beta$, they are usually called survival probabilities. In the case of the survival probabilities, the quadratic products $U_{\alpha k}^* U_{\beta k} U_{\alpha j}^* U_{\beta j}$ are real and equal to $|U_{\alpha k}|^2 |U_{\alpha j}|^2$. The survival probabilities can be written in a simple form

$$P_{\nu_\alpha \rightarrow \nu_\alpha}(L, E) = 1 - 4 \sum_{k>j} |U_{\alpha k}|^2 |U_{\alpha j}|^2 \sin^2\left(-i \frac{\Delta m_{kj}^2 L}{4E}\right). \quad (2.18)$$

We have discussed about the oscillation probabilities of neutrinos. For the case of antineutrinos, the mixing matrix between flavor and mass eigenstates becomes

$$|\bar{\nu}_\alpha\rangle = \sum_i U_{\alpha i} |\bar{\nu}_i\rangle \quad (\alpha = e, \mu, \tau) \quad (2.19)$$

Considering the probability of $\bar{\nu}_\alpha \rightarrow \bar{\nu}_\beta$ oscillations. Since the kinematic properties of massive antineutrinos are the same as those of neutrinos, the only difference is

that the elements of mixing matrix are complex conjugated with respect to those in neutrino case. Applying the same transformation in Equation 2.17, we obtain the antineutrino oscillation probability

$$P_{\bar{\nu}_\alpha \rightarrow \bar{\nu}_\beta} (L, E) = \sum_{k,j} U_{\alpha k} U_{\beta k}^* U_{\alpha j}^* U_{\beta j} \exp \left(-i \frac{\Delta m_{kj}^2 L}{2E} \right). \quad (2.20)$$

The survival probability for antineutrinos $\bar{\nu}_\alpha \rightarrow \bar{\nu}_\alpha$ is

$$P_{\bar{\nu}_\alpha \rightarrow \bar{\nu}_\alpha} (L, E) = P_{\nu_\alpha \rightarrow \nu_\alpha} (L, E) = 1 - 4 \sum_{k>j} |U_{\alpha k}|^2 |U_{\alpha j}|^2 \sin^2 \left(-i \frac{\Delta m_{kj}^2 L}{4E} \right). \quad (2.21)$$

which is expected the same as the case of neutrino due to the CPT invariance.

2.2.2 Two-neutrino mixing

Two-neutrino mixing is an approximation in which two massive neutrinos out of three are considered. In fact, many neutrino oscillation experiments can be well described within the framework of two-neutrino mixing. In the case of two-neutrino mixing, we consider two flavor neutrinos ν_α and ν_β , which can be pure flavor neutrinos ($\alpha, \beta = e, u$ or $\alpha, \beta = e, \tau$ or $\alpha, \beta = \mu, \tau$) or linear combinations of pure neutrinos. The two flavor eigenstates are connected to the two mass eigenstates ν_1 and ν_2 via a unitary 2×2 mixing matrix,

$$U = \begin{pmatrix} \cos \theta & \sin \theta \\ -\sin \theta & \cos \theta \end{pmatrix}, \quad (2.22)$$

where θ is the mixing angle. In two-neutrino mixing framework, there is only one squared-mass difference

$$\Delta m^2 \equiv \Delta m_{21}^2 \equiv m_2^2 - m_1^2. \quad (2.23)$$

By substituting the 2×2 mixing matrix U into 2.17, it is straightforward to

derive the transition probability $P_{\nu_\alpha \rightarrow \nu_\beta}$ with $\alpha \neq \beta$, as seen in Figure 2.2

$$\begin{aligned} P_{\nu_\alpha \rightarrow \nu_\beta}(L, E) &= \frac{1}{2} \sin^2 2\theta \left[1 - \cos \left(\frac{\Delta m^2 L}{2E} \right) \right] \\ &= \sin^2 2\theta \sin^2 \left(\frac{\Delta m^2 L}{4E} \right) \quad (\alpha \neq \beta). \end{aligned} \quad (2.24)$$

For the case $\alpha = \beta$, the survival probabilities $P_{\nu_\alpha \rightarrow \nu_\alpha}(L, E)$ is

$$P_{\nu_\alpha \rightarrow \nu_\alpha}(L, E) = 1 - P_{\nu_\alpha \rightarrow \nu_\beta}(L, E) = 1 - \sin^2 2\theta \sin^2 \left(\frac{\Delta m^2 L}{4E} \right). \quad (2.25)$$

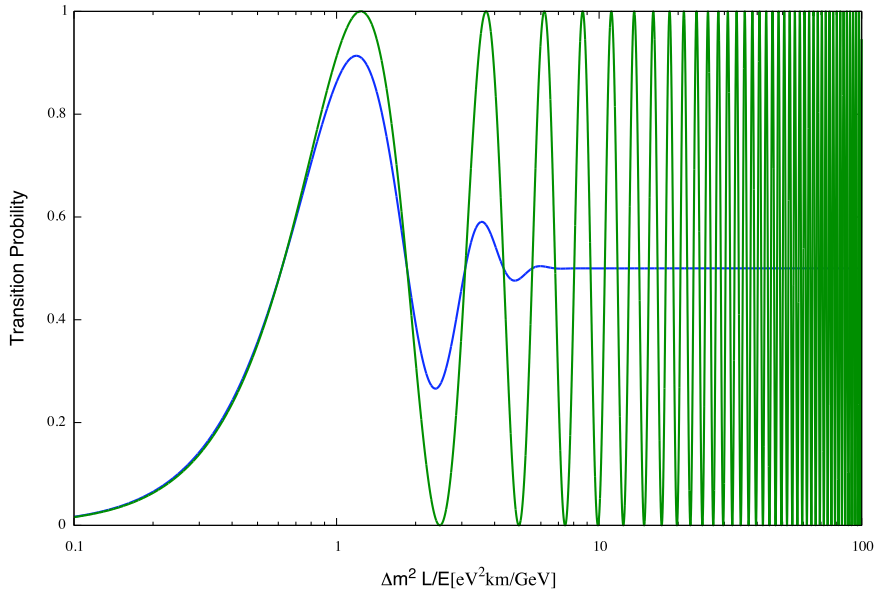


Figure 2.2: The transition probability of $\nu_\alpha \rightarrow \nu_\beta$ with $\sin^2 2\theta = 1$ as a function of $\langle L/E \rangle$. The green curve indicates a unaveraged transition probability; while the blue one indicates the smeared transition probability with $\sigma_{L/E} = 0.2 \langle L/E \rangle$.

2.2.3 Three-neutrino oscillation

For three neutrino flavors, the PMNS mixing matrix is defined to transform the mass eigenstates (ν_1, ν_2, ν_3) to the flavor eigenstates $(\nu_e, \nu_\mu, \nu_\tau)$,

$$\begin{pmatrix} \nu_e \\ \nu_\mu \\ \nu_\tau \end{pmatrix} = U_{PMNS} \begin{pmatrix} \nu_1 \\ \nu_2 \\ \nu_3 \end{pmatrix} = U_{23} U_{13}^* U_{12} U_M \begin{pmatrix} \nu_1 \\ \nu_2 \\ \nu_3 \end{pmatrix} \quad (2.26)$$

where

$$U_{23} = \begin{pmatrix} 1 & 0 & 0 \\ 0 & \cos \theta_{23} & \sin \theta_{23} \\ 0 & -\sin \theta_{23} & \cos \theta_{23} \end{pmatrix}, \quad U_{13}^* = \begin{pmatrix} \cos \theta_{13} & 0 & \sin \theta_{13} e^{-i\delta_{CP}} \\ 0 & 1 & 0 \\ -\sin \theta_{13} e^{i\delta_{CP}} & 0 & \cos \theta_{13} \end{pmatrix},$$

$$U_{12} = \begin{pmatrix} \cos \theta_{12} & \sin \theta_{12} & 0 \\ -\sin \theta_{12} & \cos \theta_{12} & 0 \\ 0 & 0 & 1 \end{pmatrix}, \quad U_M = \begin{pmatrix} e^{i\phi_1} & 0 & 0 \\ 0 & e^{i\phi_2} & 0 \\ 0 & 0 & 1 \end{pmatrix}. \quad (2.27)$$

(2.28)

Neutrino oscillations of three flavors are completely described by six parameters: three mixing angles θ_{12} , θ_{13} , θ_{23} , two independent mass-squared differences, $\Delta m_{21}^2 \equiv m_2^2 - m_1^2$, $\Delta m_{32}^2 \equiv m_3^2 - m_2^2$, and one CP-violating phase δ_{CP} . The neutrino oscillation phenomenology is independent of the Majorana phases ϕ_1 and ϕ_2 .

In a reactor-based antineutrino experiment the measured quantity is the survival probability (P_{ee}) for $\bar{\nu}_e \rightarrow \bar{\nu}_e$. With a given baseline L , the probability is expressed,

$$P_{ee} = 1 - \cos^4 \theta_{13} \sin^2 2\theta_{12} \sin^2 \Delta_{21} + \cos^2 \theta_{12} \sin^2 2\theta_{13} \sin^2 \Delta_{31} - \sin^2 \theta_{12} \sin^2 2\theta_{13} \Delta_{32}, \quad (2.29)$$

where

$$\Delta_{jk} \equiv 1.267 \delta m_{jk}^2 (\text{eV}^2) \times \frac{L(\text{km})}{E(\text{MeV})}.$$

2.3 Reactor Neutrinos

Nuclear reactors are the strongest terrestrial antineutrino source, coming from the β -decay of unstable neutron-rich product of ^{235}U , ^{238}U , ^{239}Pu and ^{241}Pu fission. The average yield is about $6\bar{\nu}_e$ per fission. The flux density is given by

$$\Phi_\nu = 1.5 \times 10^{12} \frac{P/\text{MW}}{L^2/\text{m}^2} \text{cm}^{-2}\text{s}^{-1} \quad (2.30)$$

where P is the thermal power (in MW) of the reactor and L is the distance (in m) from the reactor core. The total isotropic flux of emitted $\bar{\nu}_e$ is given ($F = 4\pi L^2$)

$$F\Phi_\nu = 1.9 \times 10^{17} \frac{P}{\text{MW}} \text{s}^{-1}. \quad (2.31)$$

The measurement of reactor antineutrino oscillation is a disappearance experiment looking for $\bar{\nu}_e \rightarrow \bar{\nu}_e$. One cannot detect $\bar{\nu}_\mu$ and $\bar{\nu}_\tau$ since the energies of reactor neutrinos are not large enough to produce μ^+ or τ^+ .

The detection reaction used mostly is



with an energy threshold of 1.806 MeV. The $\bar{\nu}_e$ energy can be obtained by measuring the positron energy, since

$$E_{\bar{n}\bar{\nu}_e} = E_{e^+} + m_n - m_p = E_{e^+} + 1.293 \text{ MeV} = T_{e^+} + 1.806 \text{ MeV} \quad (2.33)$$

with T_{e^+} the kinetic energy of the positron. The cross section of the above reaction

is given by

$$\sigma(\bar{\nu}_e + p \rightarrow e^+ + n) = \frac{G_F^2 E_\nu^2}{\pi} |\cos \theta_c|^2 \left(1 + \left(\frac{g_A}{g_\nu} \right)^2 \right) \quad (2.34)$$

$$= 9.23 \times 10^{-42} \left(\frac{E_\nu}{10 \text{ MeV}} \right)^2 \text{ cm}^2. \quad (2.35)$$

Coincidence techniques are used for identifying the above reaction with the annihilation of positron and electron as the prompt signal and a delayed capture of the neutron, which occurs 10-100 microseconds after the prompt photons.

The spectrum of $\bar{\nu}_e$ can be inferred from the measurement of positron spectrum. By comparing the spectrum of $\bar{\nu}_e$ with the theoretical calculation or measuring it at several distances from the reactor, one can measure the neutrino mixing angle.

Chapter 3

Daya Bay Reactor Neutrino Experiment

The goal of the Daya Bay experiment is to probe the mixing angle θ_{13} with a sensitivity of 0.01 or better in $\sin^2 2\theta_{13}$ at 90% confidence level. by measuring the rates and energy spectra of reactor antineutrinos at different baselines.

In Section 3.1, the site description of the Daya Bay experiment will be presented. The detectors, including the antineutrino detectors (ADs), water Cherenkov detectors (WP), and the resistance plate chamber detectors (RPCs) will be introduced in Section 3.2 and 3.3, respectively. At the last section, the recent Daya Bay results on θ_{13} will be discussed.

3.1 The Site Description

The Daya Bay Experiment [33] is located near the Daya Bay nuclear power complex situated at the southern coast of China which is 55 km to the northeast of Hong Kong and 45 km to the east of Shenzhen. The locations of the detectors and reactor cores are shown in Figure 3.1. The Daya Bay nuclear power complex consists of three nuclear power plants (NPPs): Daya Bay NPP, Ling Ao NPP and Ling Ao II NPP. Each NPP consists of two reactor cores separated by 90 m. All six cores are

functionally identical pressurized water reactors (framaton M310 nd its derivative CPR 1000) of 2.9 GW thermal power [33]. With maximum thermal power output of 17.4 GW in six reactor cores, it gives a prolific source of reactor antineutrinos ($\sim 6 \times 10^{20} \bar{\nu}_e/\text{s}/\text{core}$). The mountainous terrain near the reactor cores provides an ideal site for constructing underground laboratories that are well shielded from cosmic rays.

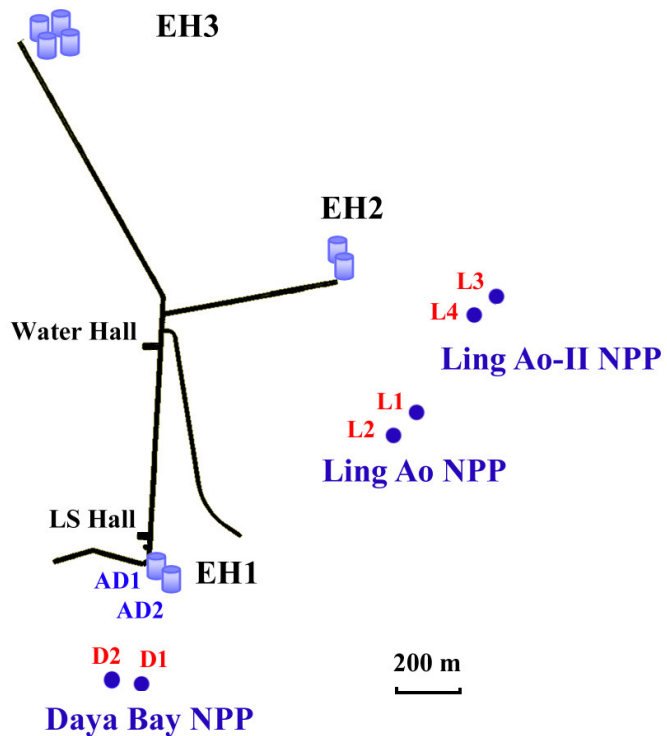


Figure 3.1: Layout of the Daya Bay experiment.

There are three experimental halls (EHs) in the Daya Bay experiment: two near halls, Daya Bay near hall (EH1) and Ling Ao near hall (EH2), and one far hall (EH3). The two near halls which are 300-500 m from the Daya Bay and Ling Ao NPPs respectively, are responsible for measuring the initial fluxes of $\bar{\nu}_e$ from the reactor cores. The disappearance probability of $\bar{\nu}_e$ as a function of the baseline

is given by

$$P_{\text{dis}} \approx \sin^2 2\theta_{13} \sin^2 \left(\frac{\Delta m_{21}^2 L}{4E} \right) + \cos^4 \theta_{13} \sin^2 2\theta_{12} \sin^2 \left(\frac{\Delta m_{31}^2 L}{4E} \right) \quad [33]. \quad (3.1)$$

As seen in Figure 3.2, the location of EH3 is chosen around the first oscillation maximum of P_{dis} , which is sensitive to $\sin^2 2\theta_{13}$. Table 3.1 shows the overburden, muon rate, average muon energy, and average distances to the reactor pairs for each EH, respectively.

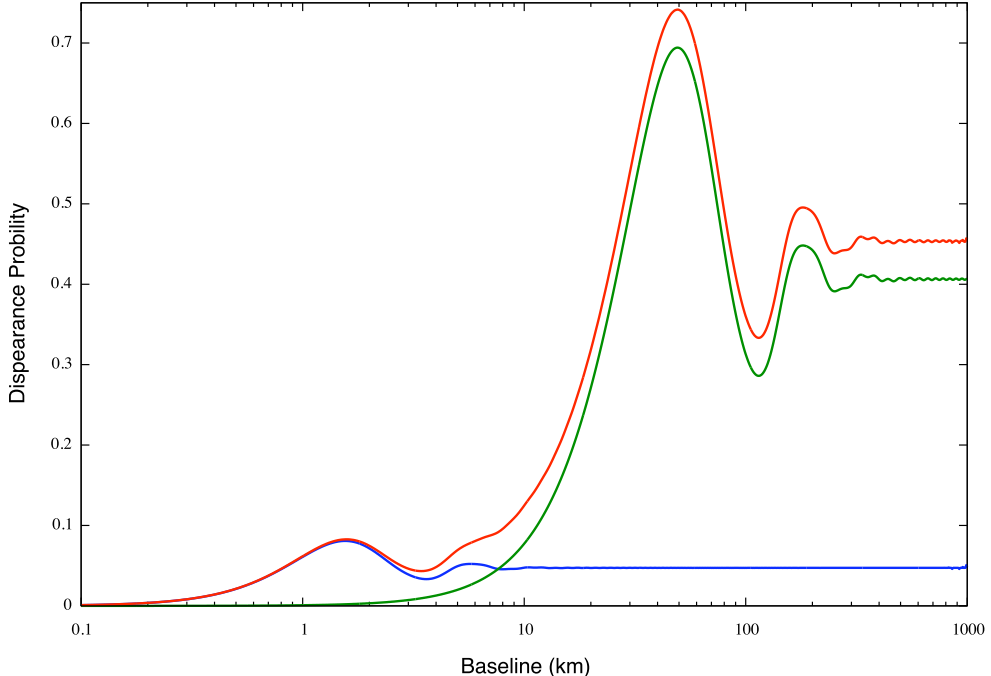


Figure 3.2: The disappearance probability of $\bar{\nu}_e$ as a function of the distance between the reactor core and the detector. The blue and the green curves represent the contribution from θ_{13} and θ_{12} respectively, while the red curve shows the sum of these two.

Each near hall consists of two antineutrino detectors (ADs), while four ADs are deployed in the far hall in order to increase the statistics. Each AD is submerged in a water pool. The water pool shields background from the surrounding rocks

	EH1	EH2	EH3
Overburden (m.w.e)	250	265	860
Muon rate (Hz)	1.27	0.95	0.56
Average muon energy (GeV)	57	58	137
Distance from D1/D2	364	1348	1912
Distance from L1/L2	8557	480	1540
Distance from L3/L4	1307	528	1548

Table 3.1: Site information including baselines and overburdens. D1/D2, L1/L2, and L3/L4 mean the reactor cores and Figure 3.1 shows the layout.

and serves as a water Cherenkov detector to tag cosmic-ray muons. On top of the water pool, a layer of resistance plate chambers (RPCs) gives an additional muon-tagging. Fig. 3.3 shows the schematics of the Daya Bay near hall. EH3 has a similar layout with a larger water pool and RPC module array.

3.2 Antineutrino Detector

The antineutrino detector is a three-zone cylindrical structure. Two acrylic vessels with diameters about 3.1 m and 4 m are nested inside a 5-m diameter stainless steel vessel (SSV), as illustrated in Figure 3.4.

The innermost acrylic vessel (IAV) is filled with about 20 tons of Gadolinium-doped liquid scintillator (GdLS) as the target region. The medium zone between IAV and the outer acrylic vessel (OAV) is filled with about 20 tons of pure liquid scintillator (LS) to capture gamma rays escaping from the target region. The density of GdLS and LS is about 0.86 g/cm³. The 37 tons of Mineral oil (MO), filled in the outermost zone, is served as a buffer preventing the external radiation from entering the fiducial volume. The density of MO is about 0.85 g/cm³, which matches closely with that of GdLS and LS to reduce the buoyancy force and the stress on the acrylic vessels.

A total of 192 8-inch Hamamatsu R5912 photomultiplier tubes (PMTs) are

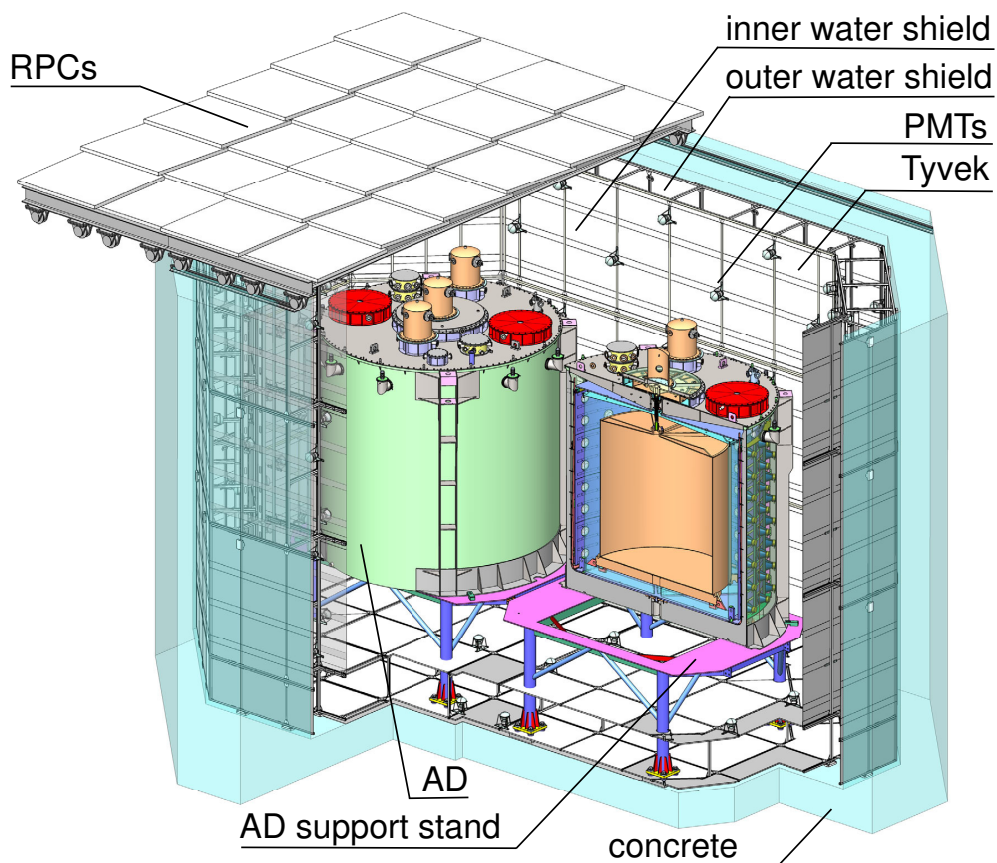


Figure 3.3: Schematic of the Daya Bay near hall (EH1) including the ADs, water shields, and RPCs.

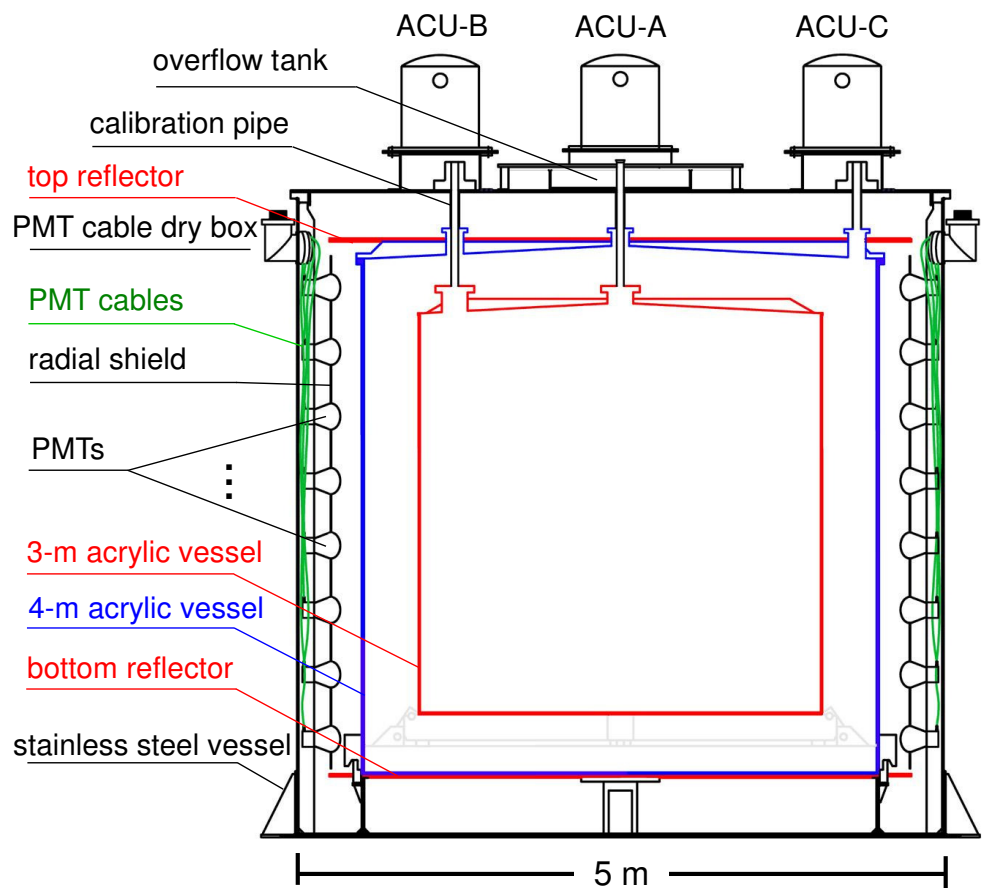


Figure 3.4: Schematic drawing of the antineutrino detector.

mounted on the removable ladders that are secured on the inner wall of SSV with rails, resulting in an effective photo-coverage of 12%. The PMTs are installed in 8 rows (rings) and 24 columns, and each PMT is separated by 0.5 m vertically and 15 degrees in azimuthal angle. A radial light shield, made of 3-mm thick black tyvek, is installed on the PMT ladders to simplify the light propagation: either directly from the interaction vertex or from the reflectors inside the AD.

Inside the SSV, two reflective panels with a diameter of 4.5 m and a thickness of 2 mm are installed on the top and the bottom of the MO buffer region to increase the photo-statistics and improve the uniformity of the energy response. The reflector are laminated with a film of ESR (VikuitiTM Enhanced Specular Reflector Film) sealed between two 1-cm thick acrylic panels. The ESR film has a reflectivity greater than 98% across most of the relevant spectrum.

Three Automated Calibration Units (ACUs) are installed on the top of the AD as shown in Figure 3.4. ACU-A sits on the central axis of the AD. ACU-B is located at a radius of 135.00 cm to calibrate and study the edge effects of the IAV. ACU-C is located at a radius of 177.25 cm for calibrating the gamma catcher, on the opposite side to ACU-B. Each ACU is equipped with a LED, a ⁶⁸Ge source, and a combined source of ²⁴¹Am-¹³C and ⁶⁰Co. The ²⁴¹Am-¹³C source generates neutrons at a rate of 0.5 Hz. The rates of the ⁶⁰Co and ⁶⁸Ge are about 100 Hz and 15 Hz, respectively. The sources can be located to better than 0.5 cm along a vertical line down to the bottom of the acrylic vessels. To supplement the automated system, the manual calibration system (MCS) has also been constructed. Figure 3.5 illustrates the 3D model of MCS installed on the AD. The MCS used a combined source including of ⁶⁰Co and ²³⁸Pu-¹³C. The robotic arm of MCS could reach into the AD through ACU-A penetration, and is able to position the sources at any location inside the target volume. Table 3.2 summarizes properties of the calibration sources in ACU and MCS.

Six 2-inch PMTs (Hamamatsu R7724) are installed at the top and bottom of the AD, for monitoring the attenuation length of the GdLS and LS via the

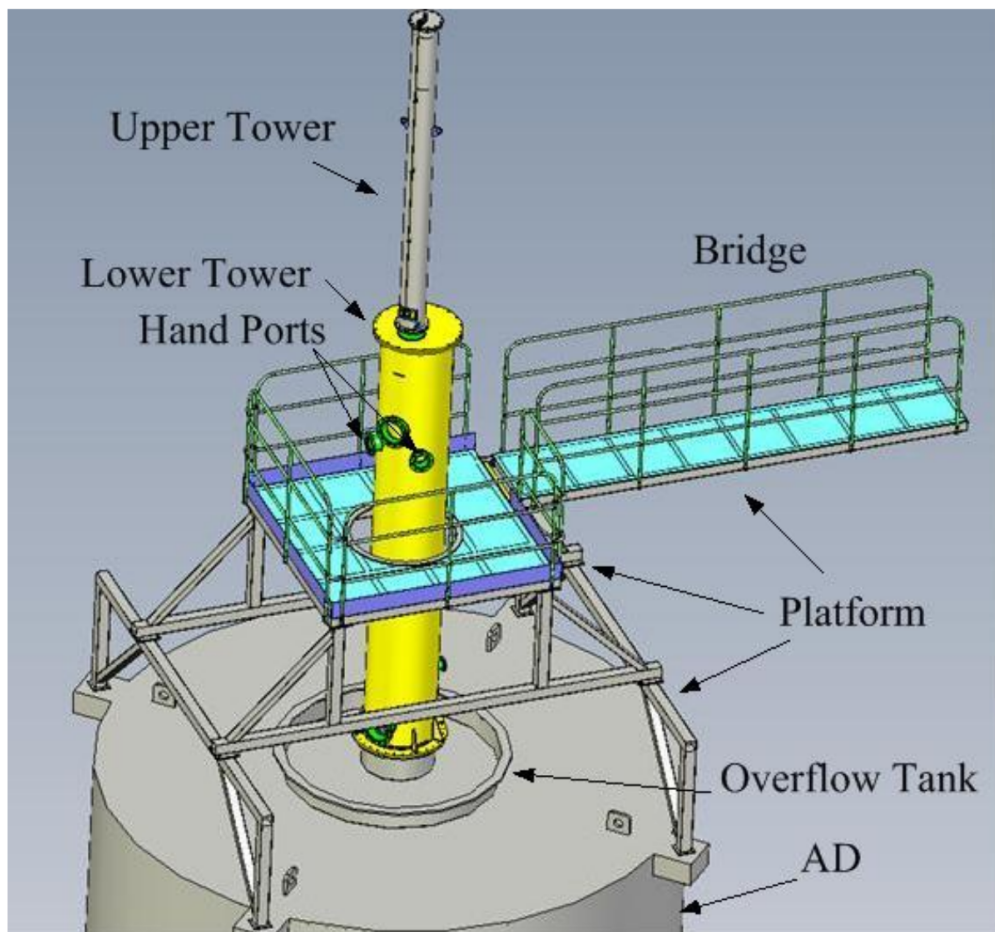


Figure 3.5: The 3D model of the MCS installed on the AD.

optical windows on the reflective panels. The mineral oil clarity device is installed for monitoring the attenuation length of the mineral oil by detecting LED light reflected back from the bottom of the AD. Sensors and CMOS cameras are installed inside the AD for monitoring the temperatures and levels of liquids.

Source	Type	Energy	Half-life	Rate (Hz)	Auto/Manual System
LED	visible γ	430 nm	-	500 (adjustable)	Auto
^{68}Ge	e^+	1.022 MeV	270.95 d	10	Auto
^{60}Co	γ	2.5 MeV	1925.28 d	100	Auto and Manual
$^{241}\text{Am}-^{13}\text{C}$	n	~ 8 MeV*	432.6 y	~ 0.5	Auto
$^{238}\text{Pu}-^{13}\text{C}$	n	~ 8 MeV*	24110 y	~ 1000	Manual

Table 3.2: Lists of calibration sources. (*) indicates the energy of capture gammas.

3.3 The Muon System

The major background in the Daya Bay experiment is the cosmic-ray muon induced backgrounds. Although the detectors are located in the mountainous terrain, the energetic muon can still penetrate and induce backgrounds in EH. To reduce the cosmic-ray induced backgrounds, it is important to be able to tag cosmic-ray muons entering the detectors efficiently and provide a shielding from those kinds of backgrounds. The muon detection system consists of a water Cherenkov detector and a Resistive Plate Chamber.

As seen in Figure 3.3 the ADs are submerged in a water pool. The water pool provides an at least 2.5 m of water in every direction to shield backgrounds from the surrounding rocks and serves as a water Cherenkov detector to tag cosmic-ray muons. The water pool is separated into two regions: the inner water shield (IWS) and the outer water shield (OWS) by Tyvek film 1070D reflectors. Each region operates as an independent water Cherenkov detector. There are totally 288 8-inch PMTs installed in each near hall, and 384 in the far hall. Assuming any AD trigger with an energy > 20 MeV resulting from cosmic-ray muon, the

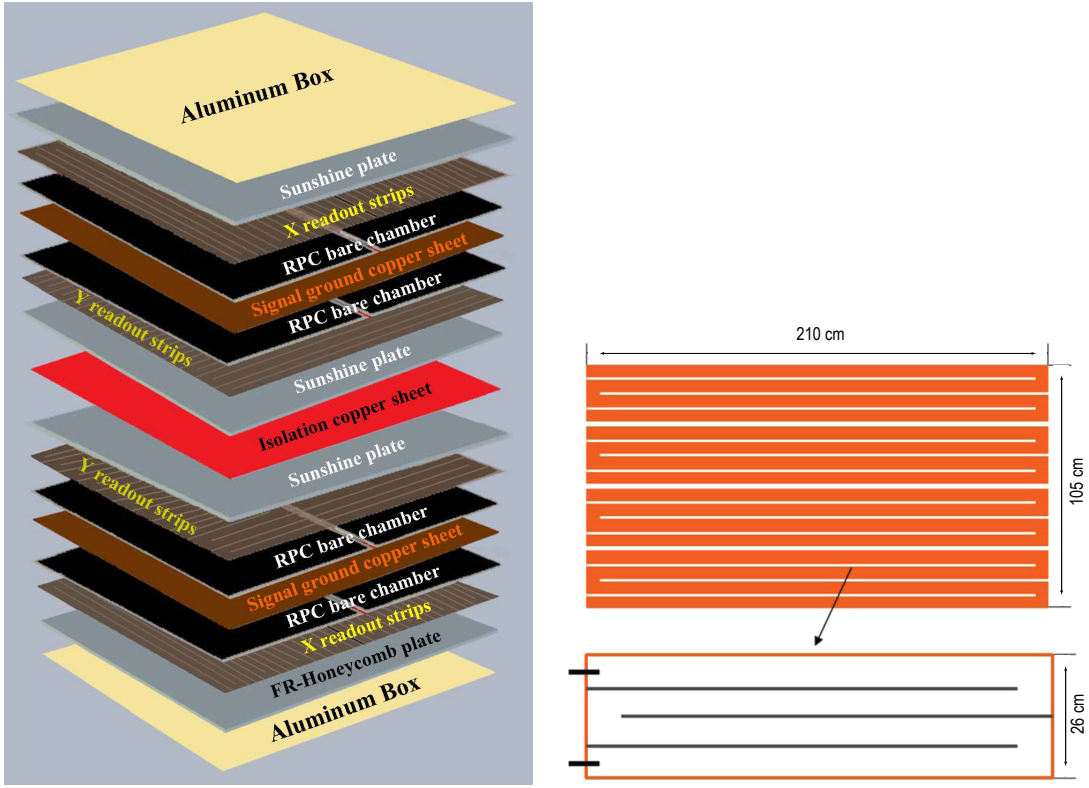


Figure 3.6: Schematic drawing of an RPC module structure.

muon detection efficiency is 99.7% and 97% for the IWS and OWS, respectively [53]. The larger inefficiency of the OWS is due to muon decay in the IWS or an AD.

Each water pool is covered with an array of RPC module. 54 modules are installed in both of the near halls, and 81 in the far hall. The $2.17\text{ m} \times 2.20\text{ m} \times 8\text{ cm}$ modules are deployed in an overlapping pattern on a steel frame mounted on rails, so that the assembly can be retracted to provide access to the water pool. There are four layers of bare chambers in one module, and each layer contains 8 readout strips, providing a spacial resolution of $\sim 8\text{ cm}$. Figure 3.6 shows the schematic of an RPC module structure.

3.4 The Measurement of the Mixing Angle θ_{13}

In March 8, 2012, the Daya Bay experiment reported the first observation of non-zero θ_{13} with a significance of 5.2 standard deviations. In June, with 2.5 times larger statistics , an improved measurement of $\sin^2 2\theta_{13}$ was determined to be $0.089 \pm 0.010(\text{stat}) \pm 0.005(\text{syst})$ [45].

3.4.1 Event selection and the efficiencies

The detection of an antineutrino from the reactor is via the inverse beta decay (IBD),

$$\bar{\nu}_e + p \rightarrow n + e^+, \quad (3.2)$$

in which the antineutrino from the reactor interacts with a target proton creating a neutron and a positron. The positron annihilates with an electron quickly, depositing 1 MeV of rest mass energy plus the excess kinetic energy from the $\bar{\nu}_e$. The neutron is slowed down by the thermalization process in few microseconds and finally is captured on the Hydrogen or Gadolinium in the target volume, releasing γ rays with energy 2.2 or 8 MeV, respectively. In this analysis, the neutron captured on Gd is treated as a delayed signal, while the positron annihilation is the prompt one.

The events are defined as muons if the following criteria are fulfilled,

- AD muon (μ_{AD}): $E > 20$ MeV;
- AD showering muon(μ_{sh}): $E > 2.5$ GeV;
- WP muon (μ_{WS}): number of fired PMTs (NHIT) > 12 in IWS or OWS;

By applying the following selection cuts, the IBD can be selected,

- Removal of the instrumental backgrounds;
- Prompt energy cut: $0.7 \text{ MeV} < E_p < 12 \text{ MeV}$;

- Delayed energy cut : $6 \text{ MeV} < E_d < 12 \text{ MeV}$;
- time correlation cut: $1 \mu\text{s} < \Delta t < 200 \mu\text{s}$ ($\Delta t \equiv t_d - t_p$, where t_p and t_d are the times of prompt and delayed signals);
- Muon veto:
 - any AD triggers are vetoed within $(-2 \mu\text{s}, 200 \mu\text{s})$ for μ_{WS} ;
 - IBD candidate is vetoed if $t_d - t_{\mu_{\text{WS}}} < 600 \mu\text{s}$, $t_d - t_{\text{AD}} < 1000 \mu\text{s}$ or $t_d - t_{\text{sh}} < 1 \text{ s}$.
- Multiplicity cut: no additional event with $E > 0.7 \text{ MeV}$ in the interval $200 \mu\text{s}$ before t_p , $200 \mu\text{s}$ after t_d , or between t_p and t_d .

For our relative measurement, the absolute efficiencies and the correlated uncertainties cancel among themselves. Only the relative efficiencies and uncorrelated uncertainties contribute to the error in the measurement of θ_{13} . Table 3.3 shows the the summary of absolute efficiencies, and the corresponding correlated and uncorrelated systematic uncertainties.

	Efficiency	Correlated	Uncorrelated
Target protons		0.47%	0.03%
Flasher cut	99.98%	0.01%	0.01%
Delayed energy cut	90.9%	0.6%	0.12%
Prompt energy cut	99.88%	0.10%	0.01%
Multiplicity cut		0.02%	<0.01%
Capture time cut	98.6%	0.12%	0.01%
Gd capture fraction	83.8%	0.8%	<0.1%
Spill-in	105.0%	1.5%	0.02%
Livetime	100.0%	0.002%	<0.01%
Combined	78.8%	1.9%	0.2%

Table 3.3: Summary of absolute efficiencies, and correlated and uncorrelated systematic uncertainties.

The absolute efficiency of the prompt energy cut is determined to be 99.88%. The energy spectrum is shown in Figure 3.7. The inefficiency is mainly from the event occurred at the edge of the IAV, resulting in a rejected prompt signal ($E < 0.7$ MeV). By comparing the asymmetries of energy scale at the edge of IAV among ADs, the uncorrelated uncertainty can be determined to be 0.01%. From the comparison between MC and data using the calibration source ^{68}Ge , the correlated uncertainty is estimated to be 0.1%.

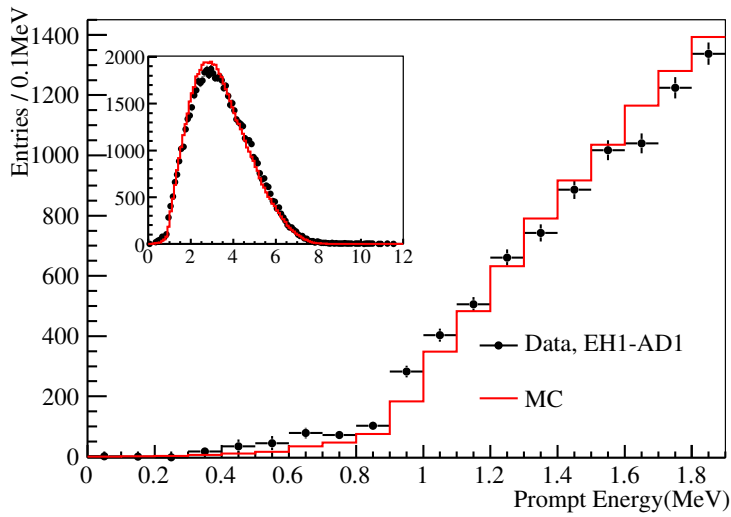


Figure 3.7: Prompt energy spectrum from EH1-AD1.

The absolute efficiency of the delayed energy cut is determined to be 90.9%. The energy spectrum is seen in Figure 3.8. By comparing the fraction of events in 6-7 MeV region to that in 6-12 MeV between MC and data, the correlated uncertainty is calculated to be 0.6%. From previous study, there exists 0.5% asymmetry of the energy scale at 6 MeV in ADs, it leads a 0.12% uncorrelated uncertainty.

From MC, there are about 5% IBD occurred outside the GdLS region, and the neutrons from IBD are finally captured on Gd in the GdLS region. By modeling the relative difference in the acrylic vessel thickness, acrylic density and liquid density,

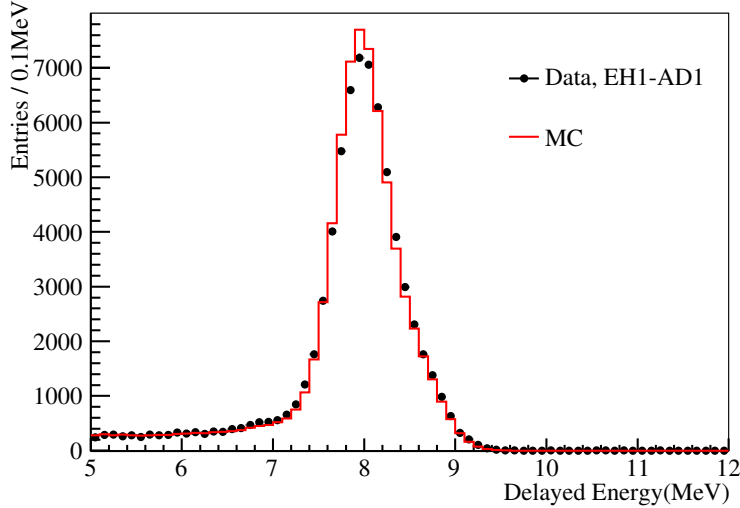


Figure 3.8: Delayed energy spectrum from EH1-AD1.

the spill-in efficiency is determined to be $105\% \pm 1.5\%(\text{corr}) \pm 0.02\%(\text{uncorr})$.

The Gd capture fraction is evaluated to be 83.8% from MC. By measuring the difference in the neutron capture time of each AD, the uncorrelated uncertainty is $< 0.1\%$. From the comparison of MC and data in Am-C source, the correlated uncertainty is estimated to be 0.8%.

The efficiency of the capture time cut is evaluated to be 98.6% with 0.2% of events with $\Delta t < 1 \mu\text{s}$ and 1.2% events with $\Delta t > 200 \mu\text{s}$. From the comparison of MC and data in Am-C source, the correlated uncertainty is estimated to be 0.12%. The possible trigger time-walk effect and Gd-concentration variation cause an 0.02% uncorrelated uncertainty.

The muon veto efficiencies is determined from data. By adding up the muon veto time, the overlapping veto windows are merged to avoid double counting. The muon veto efficiency ϵ_μ is defined as the fraction of the livetime after muon in the total DAQ livetime.

The efficiency due to the multiplicity cut can be divided into three parts,

- no signal with $E > 0.7 \text{ MeV}$ (singles) in the time interval $200 \mu\text{s}$ before the prompt signal: $\epsilon_1 = \exp(-R_s \cdot 200\mu\text{s})$, where R_s is the singles rate.

- no singles between the prompt and delayed signals: $\epsilon_2 = 1 - R_s \bar{t}_{\text{cap}}$, where \bar{t}_{cap} is the mean neutron capture time.
- no singles in the time interval 200 μs after the delayed signal:

$$\epsilon_3 = \begin{cases} \frac{1}{R_s T_s} (1 - e^{(-R_s T_s)}) & \text{for } T_s < 200 \mu\text{s} \\ \left(1 - \frac{200\mu\text{s}}{T_s}\right) e^{-R_s \cdot 200\mu\text{s}} + \frac{1}{R_s T_s} (1 - e^{(-R_s \cdot 200\mu\text{s})}) & \text{for } T_s > 200 \mu\text{s} \end{cases},$$

where T_s is the single livetime window.

Because the ϵ_3 depends on the length of the single livetime window, the multiplicity cut efficiency must be calculated for every single livetime window. T_s is determined after the muon veto. Therefore, ϵ_m couples with ϵ_μ , and the combined efficiency is

$$\epsilon_\mu \bar{\epsilon}_m = \left(\sum_i \epsilon_m^i T_s^i \right) / T_{\text{DAQ}}, \quad (3.3)$$

where ϵ_m^i is the multiplicity cut efficiency in the i -th singles livetime T_s^i , and T_{DAQ} is the DAQ livetime.

3.4.2 Backgrounds

Table 3.4 shows the summary of signals and backgrounds in ADs in the 3 EHs. Below are the major backgrounds of the IBD selections,

3.4.2.1 Accidental background

The accidental background is defined as any pair of uncorrelated signals that satisfy the IBD selection criteria coincidentally. The probability of forming a prompt-delayed pair within the time interval 1-200 μs is calculated to be $1 - \exp(-R_p \cdot 199\mu\text{s})$, where R_p is the rate of prompt-like singles. The probability of no prompt-like singles 200 μs before the prompt-like signal and 200 μs after the delayed-like signal is estimated to be $\exp(-R_p \cdot 400\mu\text{s})$. By multiplying the probabilities and

the rate of delayed-like singles(R_d) together, the rate of accidental background can be calculated,

$$R_{\text{acc}} = R_d \cdot e^{-R_p \cdot 400\mu\text{s}} \cdot (1 - e^{-R_p \cdot 199\mu\text{s}}). \quad (3.4)$$

3.4.2.2 Fast neutron background

The energetic neutrons induced by cosmic-ray muons entering the AD could mimic the prompt signal by recoiling off a proton, and give a delayed signal after being captured on Gd. The energy deposited by a recoiled proton has a wide range which could reach to a hundred MeV. We increase the AD muon energy threshold and the number of fast-neutron is estimated in the IBD samples by extrapolating the prompt energy distribution between 12 and 100 MeV down to 0.7 MeV. As a cross-check, we select the fast neutrons associated with tagged OWS or RPC-only muons. The prompt energy spectrum is similar to the fast-neutron background in the IBD samples, as shown in Figure 3.9.

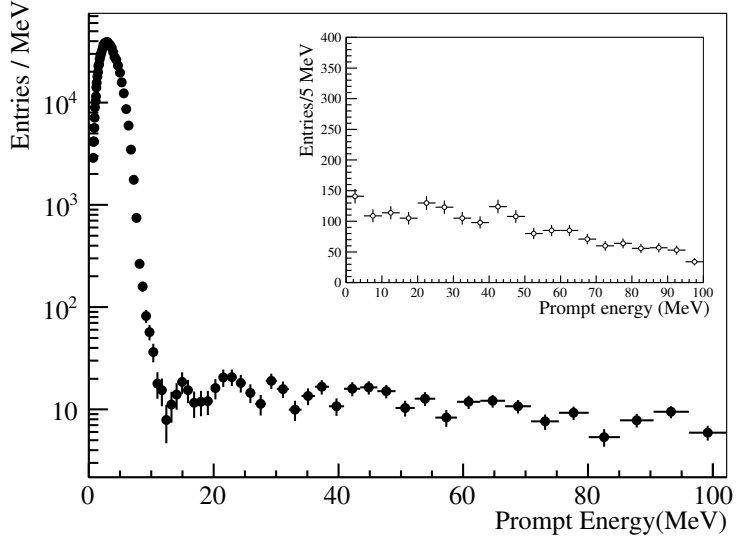


Figure 3.9: Prompt energy spectrum of IBD candidates with the upper limit relaxed. The energy spectrum of the fast neutron backgrounds tagged by the OWS muons or RPC-only muons is shown in the inset.

3.4.2.3 ${}^9\text{Li}/{}^8\text{He}$ background

The rate of correlated background from the β -n cascade of the cosmogenic ${}^9\text{Li}/{}^8\text{He}$ can be estimated by evaluating the time distribution since the last muon. One describes the time distribution by

$$f(t) = \frac{B_a}{\lambda_b} \cdot e^{-t/\lambda_b} + \frac{B_b}{\lambda_b} \cdot e^{-t/\lambda_b} + \frac{N_{IBD}}{T} e^{-t/T}, \quad (3.5)$$

where B_a and B_b being the number of β -n events for ${}^9\text{Li}$ and ${}^8\text{He}$, respectively. $T \equiv 1/R_\mu$ is the mean time between muons, while $1/\lambda_a = 1/T + 1/\tau_a$ and $1/\lambda_b = 1/T + 1/\tau_b$ with $\tau_a = 0.257$ s and $\tau_b = 0.172$ s the decay constants for ${}^9\text{Li}$ and ${}^8\text{He}$, respectively.

By modifying the criteria of IBD selection into

- $3.5 < E_p < 12.0$ MeV,
- $1 < \Delta t < 100$ μs and
- μ_{sh} veto: $t_d - t_{\text{sh}} < 1000$ μs ,

for reducing other backgrounds, the time distribution of the β -n backgrounds since the last muon is given by Figure 3.10. The numbers of the ${}^9\text{Li}/{}^8\text{He}$ background is estimated from the fitting result. To reduce the number of minimum ionizing muons in these data samples, we assumed that most of the ${}^9\text{Li}$ and ${}^8\text{He}$ production was accompanied with neutron generation, and thus rejected AD tagged muon events with no follow-on neutron (defined as > 1.8 MeV signal within a $10 - 200$ μs window). The muon samples with and without reduction were both prepared for the ${}^9\text{Li}$ and ${}^8\text{He}$ background estimation.

Figure 3.11 shows the fitted ${}^9\text{Li}$ yield as a function of the visible energy of parent muons for 3 EHs. We found that ${}^9\text{Li}$ was predominant over ${}^8\text{He}$ by doing the global maximum likelihood. Thus we can estimate the ${}^9\text{Li}/{}^8\text{He}$ background by

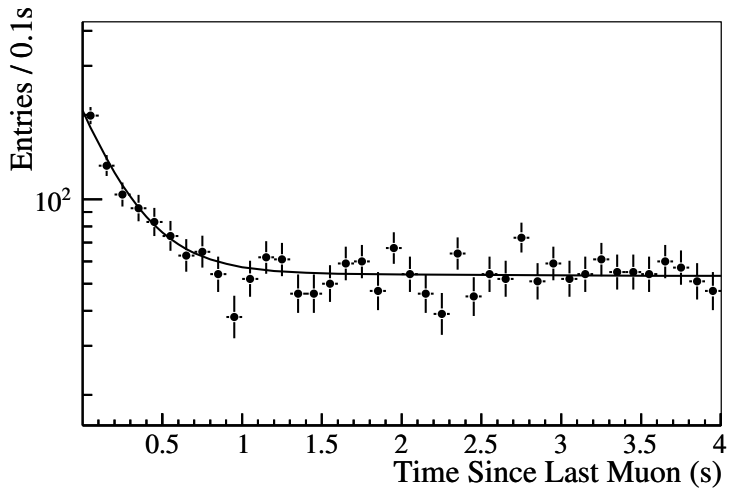


Figure 3.10: An example of the time distribution of the ${}^9\text{Li}/{}^8\text{He}$ background since the last muon.

summing over the numbers of the ${}^9\text{Li}$ background caused by muons with $E_\mu < 2.5$ GeV.

3.4.2.4 ${}^{13}\text{C}(\alpha, n){}^{16}\text{O}$ background

The ${}^{13}\text{C}(\alpha, n){}^{16}\text{O}$ background is determined by measuring α -decay rate in situ and then calculate the neutron yield by MC. Four sources of the α decays are identified: the ${}^{238}\text{U}$, ${}^{232}\text{Th}$, ${}^{227}\text{Ac}$ decay chains and ${}^{210}\text{Po}$. GEANT4 is used for modeling the energy deposition process. Based on the (α, n) cross sections in JENDL, the neutron yield as a function of α energy is calculated and summed. A 100% uncertainty is assigned since the estimation relies on MC.

3.4.2.5 Calibration source Am-C induced background

During the data taking, neutrons from the Am-C calibration source stored inside the ACU may mimic IBD events by scattering inelastically with nuclei in the shielding material, and captured on Fe, Cr, Mn or Ni in the stainless steel tank. Since the Am-C is stored on the top of AD, it has more chance to have such background in the top half of the AD. The estimation of delayed-like signals caused

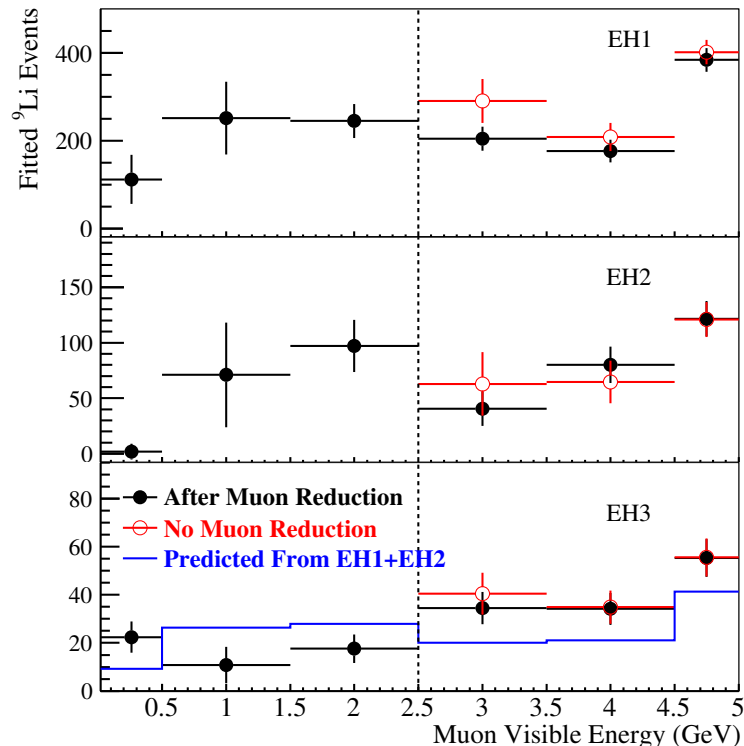


Figure 3.11: The fitted ${}^9\text{Li}$ yield as a function of the muon deposited energy in the 3 EHs. The open circles represent the fit with all muons included. Due to high muon rate, the fit is done only for $E_\mu > 2.5$ GeV. The filled circles are the results obtained by requiring a neutron following the muon as described in the text. In the bottom panel the prediction from the near site measurements is shown as a solid line.

by Am-C source is obtained by subtracting delayed-like events in the bottom half region of AD from those in the top half. The rate of Am-C delayed-like signal from data is $\sim 230/\text{day}/\text{AD}$. GEANT4 is used to estimate the probability of forming a Am-C correlated background, and gives an estimation $\sim 0.09\%$. By multiplying these two quantities together, the rate of the Am-C correlated background is estimated to be $0.2 \pm 0.2/\text{day}/\text{AD}$. A 100% uncertainty is assigned since it relies on MC.

	AD1	AD2	AD3	AD4	AD5	AD6
IBD candidates	69121	69714	66473	9788	9669	9452
Expected IBDs	68613	69595	66402	9922.9	9940.2	9837.7
DAQ livetime (days)	127.5470	127.3763			126.2646	
ϵ_μ	0.8231	0.8198	0.8576	0.9813	0.9813	0.9810
$\bar{\epsilon}_m$	0.9738	0.9742	0.9753	0.9737	0.9734	0.9732
Accidentals (per day)	9.73±0.10	9.61±0.10	7.55±0.08	3.05±0.04	3.04±0.04	2.93±0.03
Fast-neutron (per day)	0.77±0.24	0.77±0.24	0.58±0.33	0.05±0.02	0.05±0.02	0.05±0.02
$^{9}\text{Li}/^{8}\text{He}$ (per AD per day)	2.9±1.5	2.0±1.1	0.22±0.12			
Am-C correlated (per AD per day)		0.2±0.2				
(α, n) background (per day)	0.08±0.04	0.07±0.04	0.05±0.03	0.04±0.02	0.04±0.02	0.04±0.02
IBD rate (per day)	662.47±3.00	670.87±3.01	613.53±2.69	77.57±0.85	76.62±0.85	74.97±0.84

Table 3.4: Summary of signal and background in ADs in the 3 EHs.

3.4.3 θ_{13} Analysis

In the assumption of no oscillation, the $\bar{\nu}_e$ in the far hall can be predicted with a weighted combination of the two near hall measurements. The ratio of measurement to the expected rate is then $R = M_f/\bar{N}_f$, where \bar{N}_f and M_f are the predicted and measured rates in the far hall (sum of ADs). A deficit at the far hall is observed in the ratio,

$$R = 0.094 \pm 0.011(\text{stats}) \pm 0.004(\text{syst}). \quad (3.6)$$

Figure 3.12 shows the energy spectra of the measured prompt signal comparing with the prediction with non-oscillation from the measurement of two near halls.

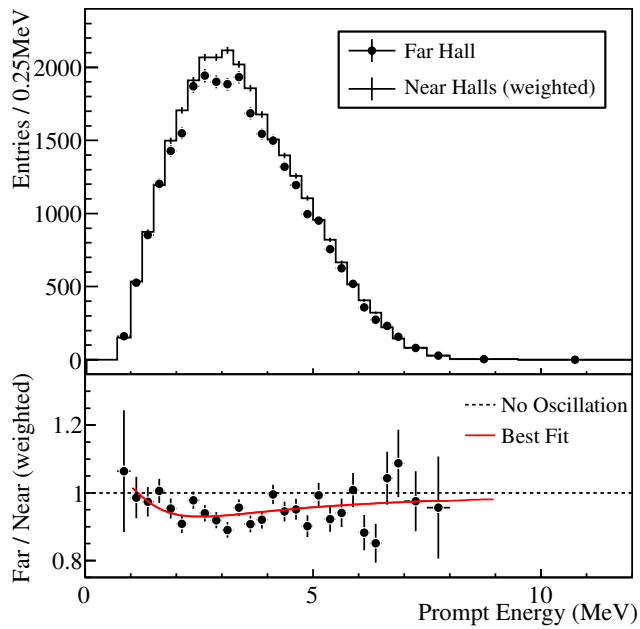


Figure 3.12: Top: Measured prompt energy spectrum of the far hall (sum of ADs) compared with the no-oscillation prediction based on the measurements of the near halls. Bottom: the ratio of measured and predicted spectrum. Red curve indicates the best fit with $\sin^2 2\theta_{13} = 0.089$; while the dashed curve is the non-oscillation prediction.

The value of $\sin^2 2\theta_{13}$ is determined with a χ^2 constructed to handle correlated systematic uncertainties,

$$\chi^2 = \sum_{d=1}^6 \frac{[M_d - T_d (1 + \varepsilon + \sum_r \omega_r^d \alpha_r + \varepsilon_d) + \eta_d]^2}{M_d + B_d} + \sum_r \frac{\alpha_r^2}{\sigma_r^2} + \sum_{d=1}^6 \left(\frac{\varepsilon_d^2}{\sigma_d^2} + \frac{\eta_d^2}{\sigma_B^2} \right), \quad (3.7)$$

where M_d is the measured IBD event number of the d -th AD with its backgrounds subtracted, B_d is the corresponding background, T_d is the prediction from antineutrino flux, including MC corrections and neutrino oscillations, ω_r^d is the fraction of IBD contribution of the r -th reactor to the d -th AD determined by the baselines and antineutrino fluxes. The uncorrelated reactor uncertainty is σ_r (0.8%). The parameter σ_d (0.2%) is the uncorrelated detection uncertainty, as shown in Table 3.3. The parameter σ_B is the quadratic sum of the background uncertainties listed in Table 3.4. The corresponding pull parameters are $(\alpha_r, \varepsilon_d, \eta_d)$. The detector- and reactor-related correlated uncertainties were not included in the analysis. The absolute normalization ε was determined from the fit to the data.

The $\bar{\nu}_e$ survival probability used in the χ^2 is

$$P_{sur} = 1 - \sin^2 2\theta_{13} \sin^2(1.267 \Delta m_{31}^2 \frac{L}{E}) - \cos^4 \theta_{13} \sin^2 2\theta_{12} \sin^2(1.267 \Delta m_{21}^2 \frac{L}{E}), \quad (3.8)$$

where $\Delta m_{31}^2 = 2.32 \times 10^{-3} \text{ eV}^2$, $\sin^2 2\theta_{12} = 0.861^{+0.026}_{-0.022}$, and $\Delta m_{21}^2 = 7.59^{+0.20}_{-0.21} \times 10^{-5} \text{ eV}^2$ [30]. The uncertainty in Δm_{31}^2 [31] is not included in the fit.

The best-fit value is

$$\sin^2 2\theta_{13} = 0.089 \pm 0.010(\text{stat.}) \pm 0.005(\text{syst.})$$

with a χ^2/NDF of 3.4/4 [45]. All best estimates of pull parameters are within its one standard deviation based on the corresponding systematic uncertainties. The no-oscillation hypothesis is excluded at 7.7 standard deviations.

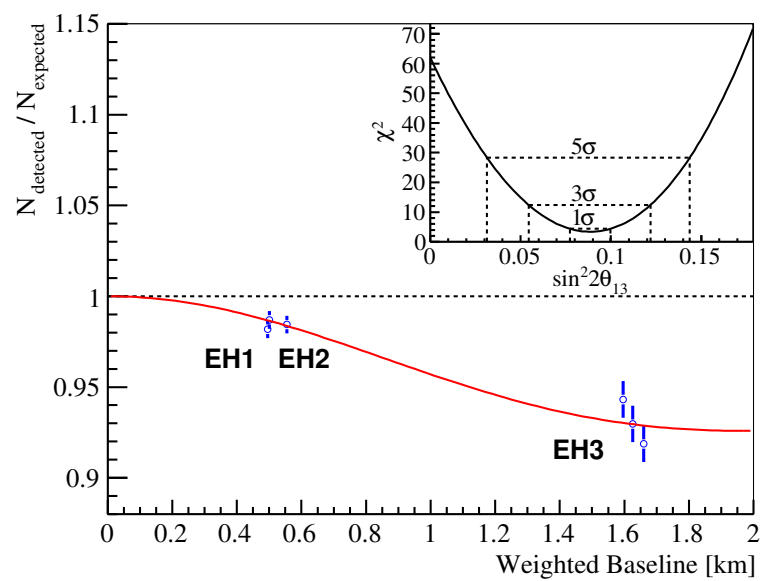


Figure 3.13: Ratio of measured versus expected signals in each detector, assuming no oscillation.

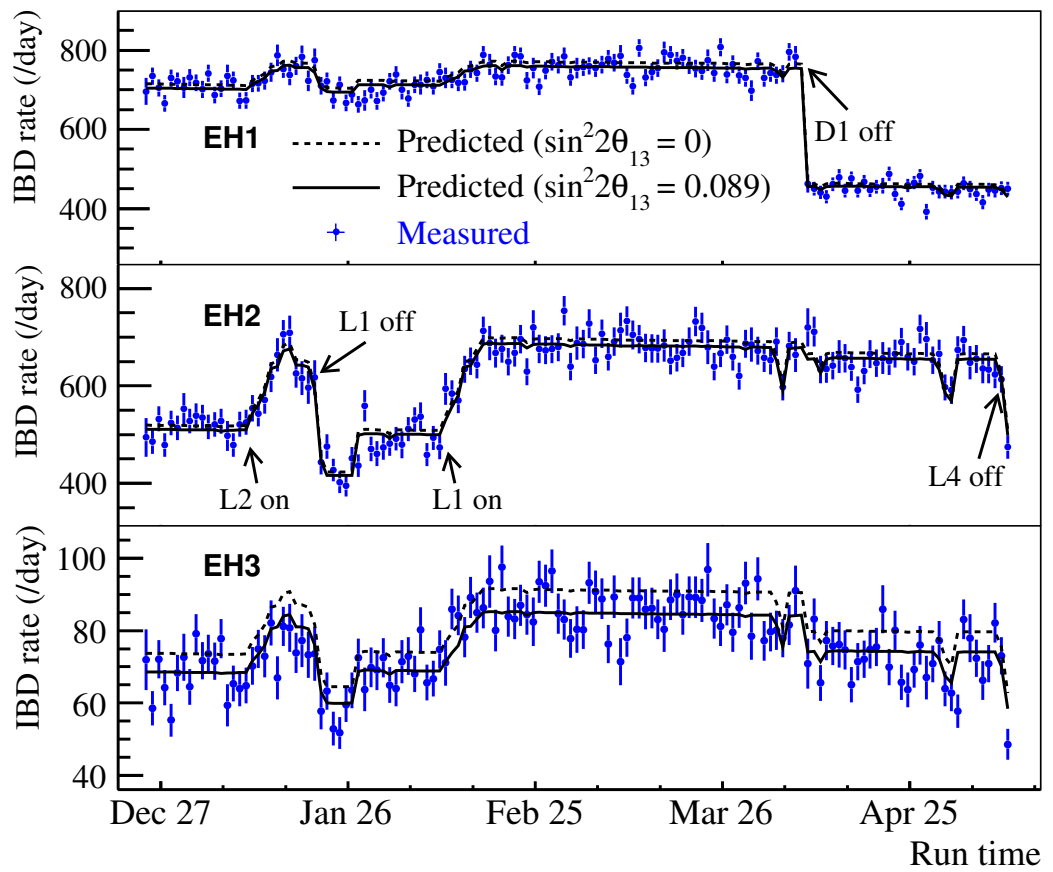


Figure 3.14: The measured daily IBD rate per AD in the three experimental halls.

Chapter 4

Data Acquisition System

The main task of the data acquisition (DAQ) system in the Daya Bay experiment is to record the antineutrino candidate events and the relevant backgrounds, such as muon-induced neutrons. The Daya Bay DAQ gives an interactive interface with the front-end electronics, the trigger system, the detector and the calibration system. The readout system (ROS) in DAQ reads data from the front-end electronics modules installed in VME crates, concatenates the data fragments into a subsystem crate by crate in parallel, and then transmits to the back-end system to do the data stream merging, monitoring and recording. The online software in DAQ configures, controls the applications in DAQ and records the non-data information into the online database. During the calibration data taking, the automatic controller takes data according to the parameters given by the calibration system.

My main contribution to the experiment during the construction stage of the Daya Bay experiment is the research and development in online system software and the automatic controller.

4.1 Hardware Architecture

The DAQ architecture design is a multi-level system using advanced commercial computer and network technology as shown in Fig 4.1. According to the site loca-

tions, DAQ system can be separated into two parts: the VME front-end system, and the back-end system.

The front-end system, which is a real-time system based on VME bus, is responsible for reading out the raw data. Each VME crate holds a VME system controller, multiple front-end readout modules and one trigger module. The VME controller, an embedded single-board computer, is used to collect, preprocess, and transfer data. It is based on a PowerPC CPU and the Universe II chip for VME bus interface. The commercial embedded operating system TimeSys Linuxlink (TimeSys/PowerPC) [38] with kernel version 2.6.9 is running on the system controller.

The Daya Bay experiment also adopted the blade server based computing farm to construct the back-end system. The DAQ has two x3650 servers acting as file servers for farm and data storage. Nine blade servers serve as computing nodes for data gathering and data quality monitoring. Scientific Linux CERN 4 X86 (SLC4/X86) is chosen as the operating system in the back-end servers.

The DAQ system has been designed entirely with a gigabit Ethernet network. Due to the distances involved, the three experimental halls connect to the surface through single mode fibers. Double peer to peer single mode fiber cables connect the front-end and back-end networks.

4.2 Software Architecture

The DAQ software in the Daya Bay experiment is designed based on the BES III DAQ and ATLAS Trigger/DAQ [37]. Functionally, the DAQ can be divided into two layers, the data flow software, and the online software as shown in Figure 4.2. The data flow software is responsible for the processing of data stream, receiving and transporting the data to storage. The online software is responsible for the operations and controls of the sub-packages in DAQ.

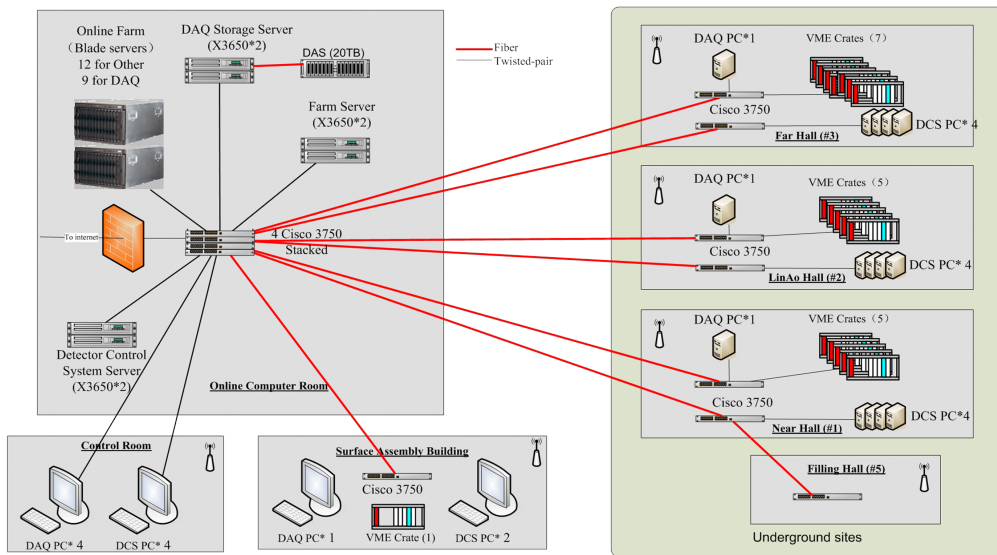


Figure 4.1: The hardware architechture of the DAQ.



Figure 4.2: The structure of the DAQ software.

4.2.1 Data flow software

The Fig 4.3 shows the data flow component diagram in DAQ, it is migrated from the back-end data flow software of ATLAS Trigger/DAQ and the front-end readout software of BES III DAQ. The readout system running on TimeSys/PowerPC, reads data, packs the fragments to a signle event and send the packed event to the back-end. The back-end components are running on the SLC4/X86. Event Flow Distributer (EFD) receives data from the multiplie ROSs through input task. The data from the linked ROSs will be merged together then sent to sub farm output (SFO). SFO can also receive data from multiple EFDs, merge and sort events by the corresponding trigger time, then record events to data files. The monitor task of EFD will parse the sent data and fill the data monitoring histograms, then publish to the information sharing (IS) server. The online histogram presenter (OHP) retrieves histograms from IS and provides a real-time data monitoring. The event flow input output (EFIO) service package is used to deal with data transportation among the data flow component.

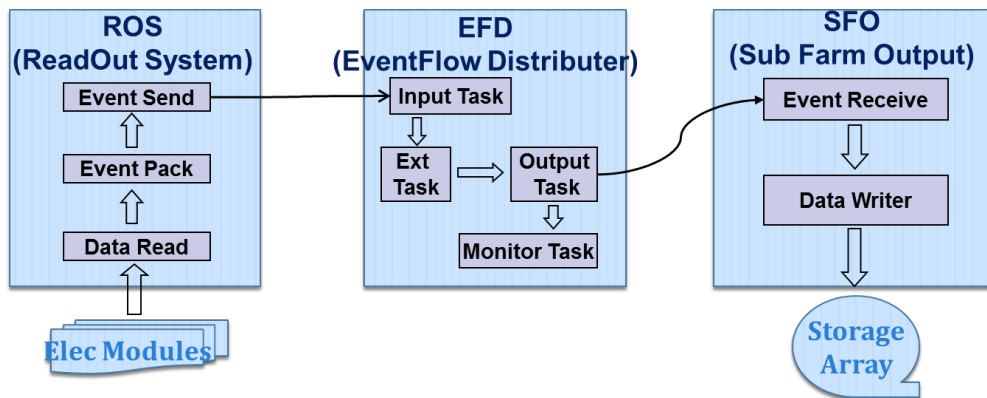


Figure 4.3: the data flow component diagram in DAQ software.

Detector	Max trigger rate (Hz)	Max bandwidth (MB/s)	Real trigger rate (Hz)	Bandwidth (MB/s)
AD1	2k	4	280	0.5
AD2	2k	4	275	0.5
WPI	2k	2.5	235	0.5
WPO	2k	3.4	346	0.5
RPC	3k	~1	193	0.03
total	11k	~15	1.33k	~1.5

Table 4.1: The performance of the readout systems in EH1.

4.2.2 Readout system

The readout system (ROS) is the front-end component in the data flow software, which has the interface with the front-end electronics, trigger system, and the back-end components of the data flow software. ROS reads data fragments from electronics modules and packs them into events, then sends events to the back-end components to do monitoring and storing, as shown in Figure 4.3

The expected maximum physics data throughput rate is less than 0.5 MB/s for one crate and less than 1.5 MB/s for one EH assuming a baseline trigger rate. The total normal physics data throughput rate for all 3 EHs is expected to be about 3 MB/s [33]. The estimations would increase with the implementation of full waveform digitization, the noisy PMTs, or the implementation of additional triggers, e.g. the LED calibration triggers. The design of ROS should have a sufficient flexibility for allowing background studies. Consequently, the designed event rate could achieve 1 kHz with a 2 kilobyte event size resulting in a throughput less than 2 MB/s per crate. Table 4.1 shows the performance of the ROSSs in EH1, and the capability of ROSSs fulfill the requirement of the Daya Bay experiment.

The ROS is capable of taking different data type according to the configuration of the electronics in different run mode. While detectors are running in a given run mode, only the affected ROSSs are configured accordingly while the others are remaining the default configuration or not working. Table 4.2 shows the summary

Run Type	AD	Water Pool	RPC
Physics	Y	Y	Y
FEE Diagnosis	Y	Y	N
Pedestal	Y	Y	N
AD Calibration	Y	Physics	Physics
Mineral Oil Monitoring	Y	Physics	Physics

Table 4.2: The summary of running types of ROSSs in different run modes. “Y” indicates that this detector works according to the run mode.

of running types of ROSSs in different run modes.

4.2.3 Online software

The online software is customized from the ATLAS online framework and migrated to TimeSys/PowerPC environment. It provides essentially the ‘glue’ that holds the various sub-systems together. It does not contain any elements that are detector specific as it is used by all the various configurations of the DAQ and detector instrumentation. The online software architecture consists of three high level components:

- Control: contains sub-packages for the control of the DAQ system detectors. Control sub-packages exist to support DAQ system’s initialization and shutdown, to provide control command distribution, synchronization, error handling, and system verification.
- Databases: contains sub-packages for configuration of the DAQ system and detectors. Configuration sub-packages exist to support system configuration description and access to it, record operational information during a run and access to this information.
- Information Sharing (IS): contains classes to support information sharing in the DAQ system. IS classes exist to report error messages, to publish states

and statistics, to distribute histograms built by the sub-systems of the DAQ system and detectors, and to distribute events sampled from different parts of the data flow chain.

The interaction between the online software packages is shown in Fig 4.4. The Control makes use of the Information Sharing and of the Databases packages. The Databases package is used to describe the system to be controlled. The IS package provides the infrastructure to obtain and publish information on the status of the controlled system, to report and receive error messages, and to publish results for interaction with the operator. The DIM¹ [34] service is responsible for communicating with the non-DAQ systems, since the IS package is limited to the internal communications among the DAQ sub-packages. DIM provides the information exchanging between DAQ and non-DAQ systems.

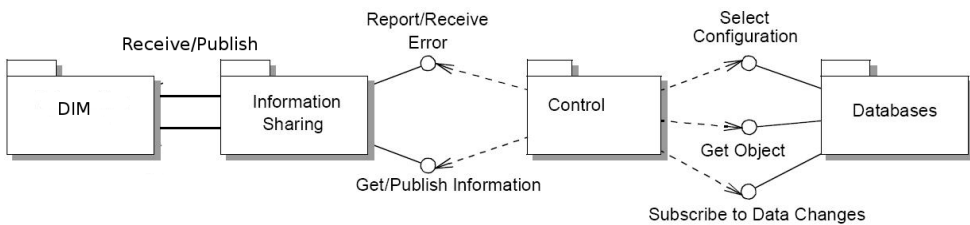


Figure 4.4: The interaction between the online software packages.

A java-based GUI (Graphic User Interface) is provided for the end user on-site, as shown in Figure 4.5, and the web-based GUI is also developed for shifter remotely, as shown in Figure 4.6.

4.2.4 Online database

The online databases are responsible for logging the data-related information, such as the calibration parameters, the configuration of front-end electronics and trigger

¹DIM (Distributed Information Management) is a communication system for distributed / mixed environments, it provides a network transparent inter-process communication layer.

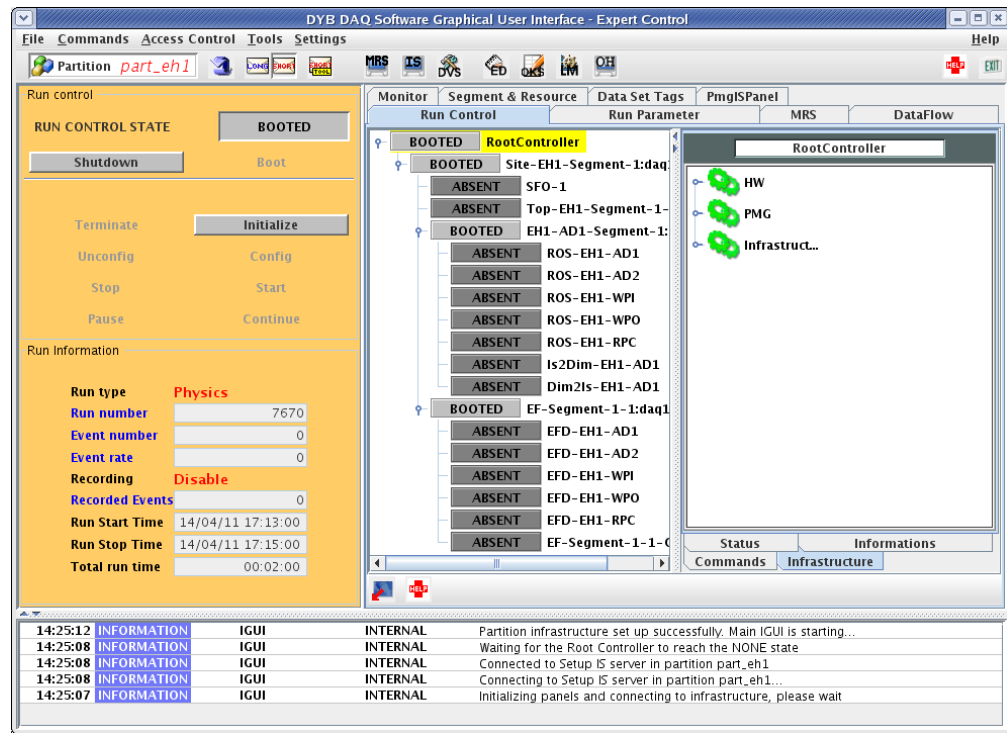


Figure 4.5: The java-based GUI of DAQ for the onsite shifter.

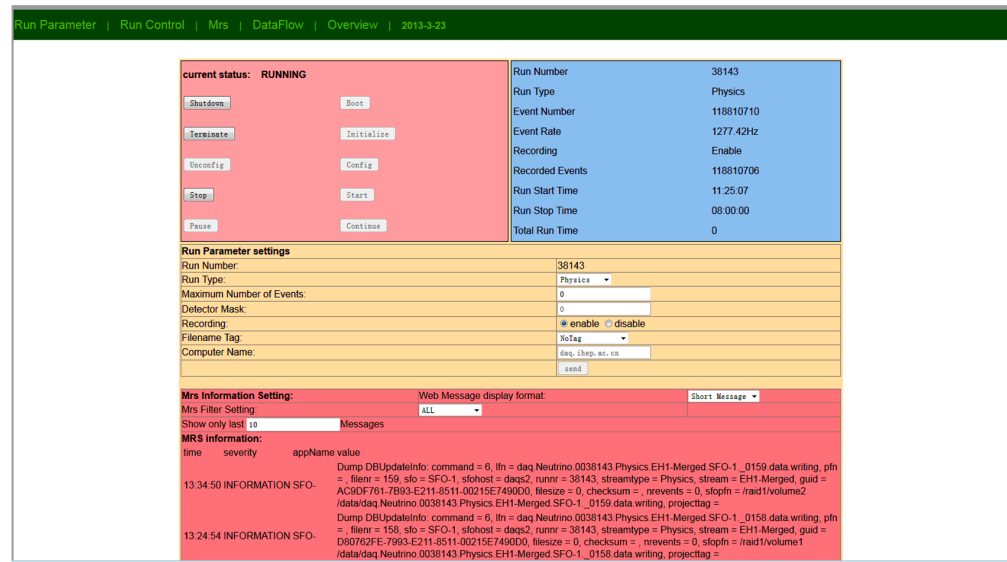


Figure 4.6: The web-based GUI of DAQ for the remote shifter.

system, the logs of DAQ, and the run information. MySQL [35] database server is used for storing such data, and CORAL [36] and COOL [36] are adopted to be the APIs (Application Programming Interface). CORAL is an abstraction layer with an SQL-free API to access data stored using relational database technologies. It is used directly by experiment-specific applications and internally by COOL. COOL provides specific software components and tools for the handling of the time variation and versioning of the experiment conditions data. Figure 4.7 shows an example of the run number table in the database. The web interface is also developed for the end user, as shown in Figure 4.8.

	Field	Type	Collation	Attributes	Null	Default
<input type="checkbox"/>	NAME	varchar(16)	latin1_swedish_ci		No	
<input type="checkbox"/>	RUNNUMBER	mediumint(9)			No	
<input type="checkbox"/>	STARTAT	varchar(24)	latin1_swedish_ci		No	
<input type="checkbox"/>	DURATION	mediumint(9)			Yes	<i>NULL</i>
<input type="checkbox"/>	CREATEDBY	varchar(16)	latin1_swedish_ci		No	
<input type="checkbox"/>	HOST	varchar(256)	latin1_swedish_ci		No	
<input type="checkbox"/>	PARTITIONNAME	varchar(256)	latin1_swedish_ci		No	
<input type="checkbox"/>	CONFIGSCHEMA	mediumint(9)			Yes	<i>NULL</i>
<input type="checkbox"/>	CONFIGDATA	mediumint(9)			Yes	<i>NULL</i>
<input type="checkbox"/>	COMMENTS	varchar(2000)	latin1_swedish_ci		Yes	<i>NULL</i>

Figure 4.7: Example shows the table which store run number information.

4.3 The Automatic Controller

The non-physics data, such as the AD calibration data, are taken routinely every period of time. Each data run at a given source stop takes few minutes, and the whole period of the AD calibration typically takes about 5 hours by deploying 3-5 run stops for one source, 3 sources in each ACU and 3 ACU in an AD. The Automatic Controller (AutoCtrl in short) in DAQ is designed for taking the routine data automatically to reduce the human-caused error. Since IS only gives the

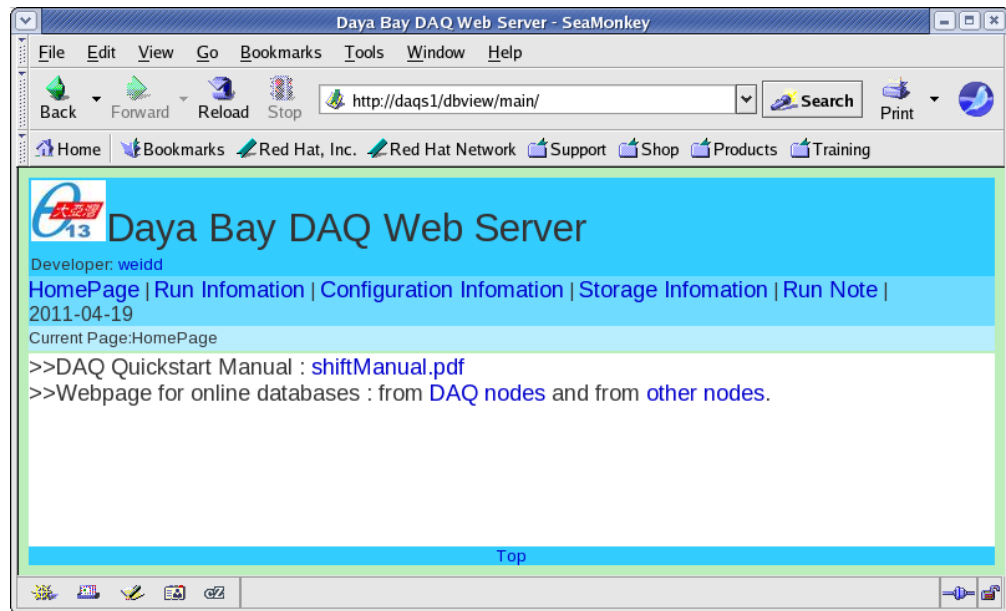


Figure 4.8: The web interface of the online database.

internal communication among the components in DAQ system, the exchange of parameters between DAQ and non-DAQ systems, e.g. the ACU, is via the DIM server. Figure 4.9 illustrates the the relationship of AutoCtrl, DIM and other sub-packages.

The functionalities of IsDIMCommu as shown in Figure 4.9 are the following,

- it publishes the information on the DAQ side in DIM server;
- it retrieves the information of non-DAQ system via DIM server, and store it in IS.

The AutoCtrl is used in different run modes: the electronic diagnosis, the pedestal run, AD calibration and the mineral oil monitoring. The working of AutoCtrl in the run mode "AD calibration" will be presented.

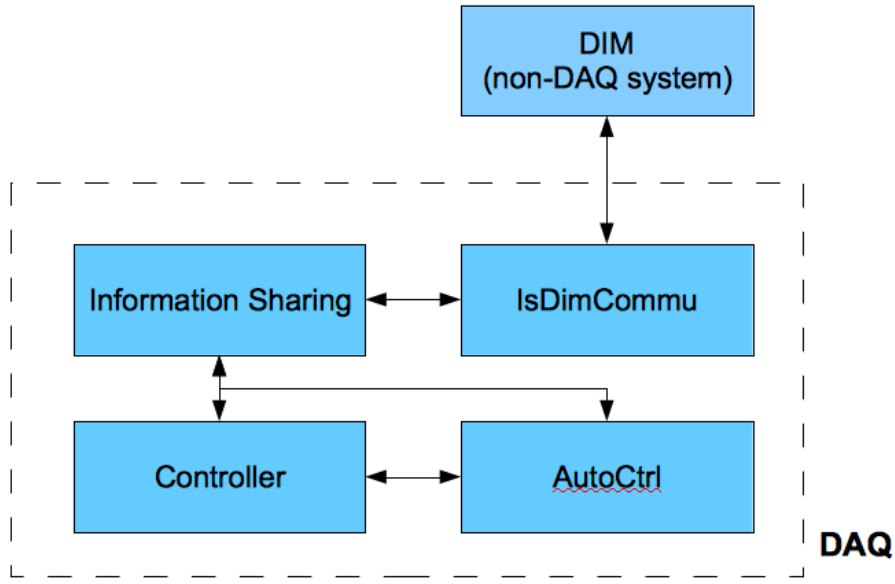


Figure 4.9: The relationship of the AutoCtrl, DIM, and sub-packages in DAQ

4.3.1 Automatic Controller in AD calibration

Figure 4.10 shows the communication protocol between the AutoCtrl and the ACU. Both sides publish their status, and listen to each other with a handshaking protocol via DIM. When the shifter is ready to do the routine AD calibration and sets the run mode to “AD calibration”, the AutoCtrl is activated. After the AutoCtrl activated, it publishes the status “Ready To Run” via DIM server to notify the control software of ACU (ACU in short). After the ACU listens to the “Ready To Run” signal, it starts to deploy the source to the designed position. AutoCtrl retrieves the parameters from ACU side and starts to take data according to the parameters when ACU publishes status “Source In Position”. The parameters corresponding to this calibration run, as shown in Table 4.3, are then stored in the online database for further analysis. During the data taking, AutoCtrl publishes its status as “Run In Progress”. After AutoCtrl informs the end of data taking, ACU then deploys the source to the next position (if there is any), and repeat the above steps until the period of calibrations end. At the end

of the calibration, the ACU moves the source home and publishes its status as "Going Home". AutoCtrl then changes the status back to "Physics" and returns the default run mode for taking physics data. With this method, after the shifter begins the weekly calibration program, the entire program in all three halls and eight ADs are executed simultaneously with fully automated data taking at one data run per source stop in each hall.



Figure 4.10: The communication protocol between AutoCtrl and ACU.

Calibration DIM Server	
Service	Explanation
CalibrationStatus	0=InitialValue, 1=SourceAtHome, 2=MovingToPosition, 3=SourceInPosition, 4=GoingHome
ADNumber	1 through 8
CalibrationAxis	0=center, 1=off-center, 2=gamma catcher, 3=oil
SourceID	0=UNKNOWN, 1= LED, 2=neutron, 3=68Ge
Z position	Z position in mm (relative to target center)
Duration	Duration of the DAQ run in second
LEDVoltage	LED Voltage in mV
LEDFreq	LED trigger frequency in Hz. Negative=n/a
LTBMode	0=multiplicity, 1=forced
Error	0=no, 1=yes
Heartbeat	1 Hz counter indicating the liveliness
DAQ DIM Server	
Service	Explanation
DAQStatus	0=Initial, 1=Physics, 2=RadyToRun, 3=RunInProgress, 4=RunEnded
Error	0=no, 1=yes
Heartbeat	1 Hz counter indicating the liveliness

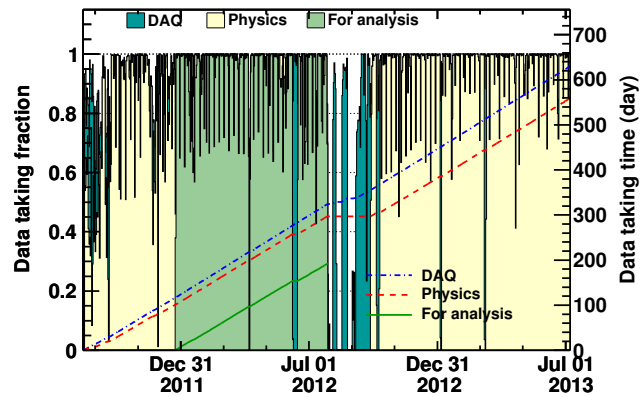
Table 4.3: The parameters and status that are exchanged between the DAQ and ACU sides.

4.4 Status

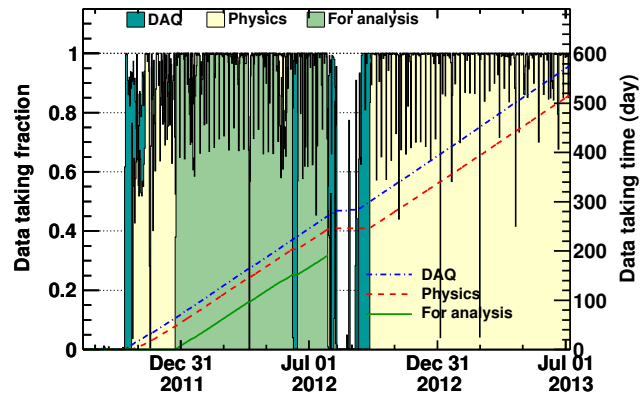
The 15 of 17 detectors start taking data since August 2011, and the full data taking begins with the whole detectors in October 2012. During the period of the data taking, the performance of the DAQ keeps stable. The total event rates in the 3 EHs are summarized in Table 4.4 and Figure 4.11 shows the live times in the 3 EHs.

Site	Detectors	Event rates
EH1	2AD+2WP+1RPC	1.33 kHz
EH2	2AD+2WP+1RPC	1.06 kHz
EH3	4AD+2WP+1RPC	807 Hz

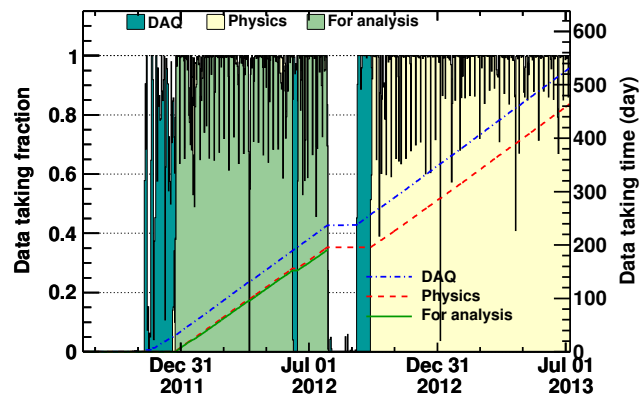
Table 4.4: Summary of the event rates in the 3 EHs.



(a) Live time in EH1



(b) Live time in EH2



(c) Live time in EH3

Figure 4.11: The live times in 3 EHs. The light green region was the data used for this analysis.

Chapter 5

Event Reconstruction of Antineutrino Detectors

The raw output of the AD is simply a collection of hits, where a hit is just a pair of ADC and TDC counts. Directly looking at the raw ADC and TDC values gives less physical meaning with regard to antineutrino or muon-induced neutron detections. The purpose of reconstruction is to convert the values recorded by FEE back to the physical quantities: such as energy, time and vertex of this event. The reconstruction involves:

- the conversion of raw ADC and TDC counts back to number of photoelectrons created at the PMT and time of the event,
- the conversion of photoelectrons to energy of the event.

Figure 5.1 shows the flowchart which describes the steps of the reconstruction that convert raw signals to physical quantities.

There are small number of AD PMTs which spontaneously emit light due to discharge within the base. These instrumental backgrounds are referred to as flasher events. The instrumental backgrounds can be removed by observing the charge distribution among the PMTs in the AD.

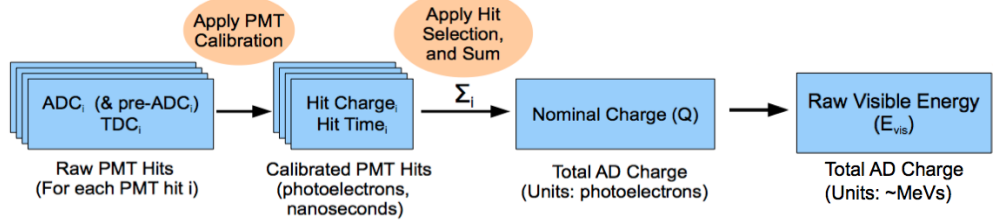


Figure 5.1: A flowchart showing the steps of event reconstruction in the AD.

In this chapter, the gain calibration of PMT, the energy and vertex reconstructions, and flasher removal will be presented.

5.1 PMT Calibration

The goal of PMT gain calibration is to obtain the constant that converts the ADC count to a single photoelectron (SPE) created at the PMTs. The coarse gain ADC is responsible for the signals with high energy ($\gtrsim 200$ p.e.), and can be calibrated by using the self-test pulses from the FEE. There are two ways to calibrate the fine gain constants: one way is to take calibration data by deploying the low-intensity LED from the ACU-A at the center of the ADs [39], and the other way is to analyze the dark noise [40] from the physics data stream.

5.1.1 Calibration using the low-intensity LED

The LED from the ACU-A is deployed at the center of the detector once per week. To suppress the double and multiple photoelectron events, the intensity of the LED is tuned in a way that the average PMTs would record only less than 13% of the total number of triggers (occupancy < 0.13) to ensure significant SPE spectra. To avoid the dark noise, the occupancies are required to be more than 0.01. Figure 5.2 shows a two-dimensional histogram of the PMT occupancy of AD1 in an LED calibration run. The PMTs on the cylindrical wall are unfolded to a two-dimensional sheet with x-axis being the column number and y-axis being the ring number of the PMTs. To get sufficient statistics (statistical error less

than 0.5%), the data-taking of LED calibration run would be at least 10 minutes.

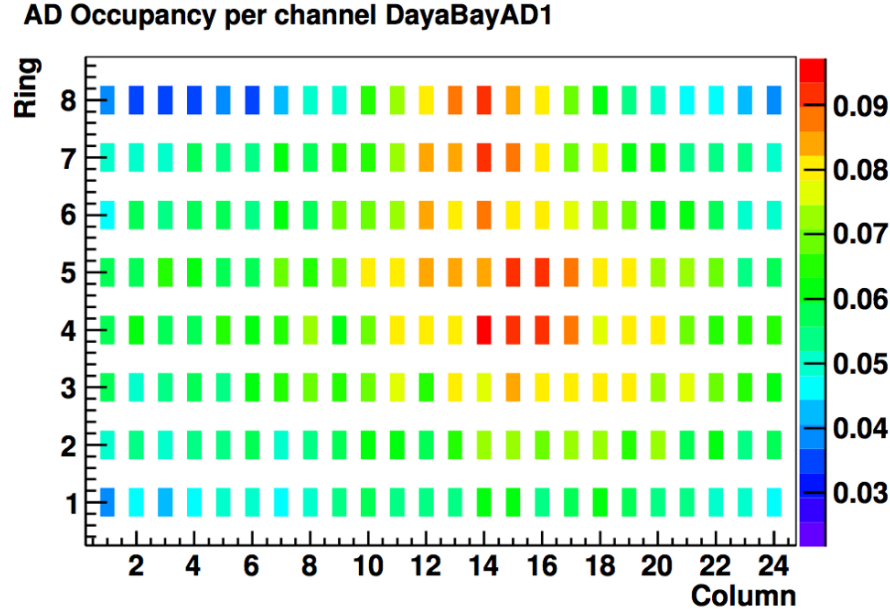


Figure 5.2: The occupancies of 192 PMTs at AD1 in an LED calbraiton run.

To select pure LED photons, the following cuts are made in processing PMT hits,

1. The TDC count of the first hit in PMT is within [950, 1050] to avoid the dark noise and after-pulses, as shown in Figure 5.3.
2. The peak cycle from the ADC peak finding algorithm locates between the third and the eighth cycle.
3. Remove the 40 MHz electronics noises.

5.1.2 Calibration using the dark noise

Comparing with the calibration using LED source once per week, the dark noise hits in the data stream provide us a method to do a real time gain measurement.

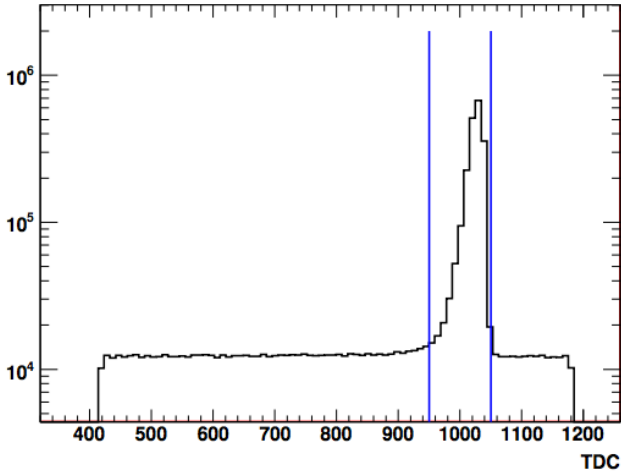


Figure 5.3: TDC distribution of a PMT in a LED calibration run. The blue lines indicate the selection region.

We select the hits before the main peak in TDC. It is believed that those hits are dark noise. Below are the cuts used for selecting dark noise,

1. Time to previous trigger is above $20 \mu\text{s}$ to suppress the effect from the previous trigger.
2. Number of fired PMTs in the noise windows must be less than three to prevent low energy physics events.
3. Only one hit is allowed per PMT channel.
4. The TDC count of the hit in PMT is larger than 1070 to make sure it is before the main peak. See Figure 5.4.
5. The peak cycle locates between the fourth and the sixth cycle.
6. Remove the 40 MHz electronics noises.

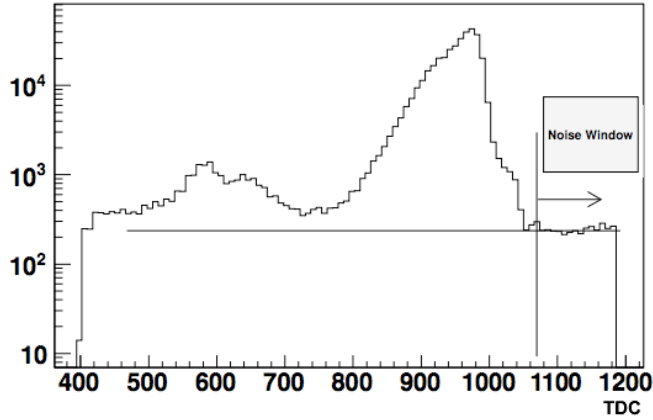


Figure 5.4: A typical TDC distribution of a PMT. The vertical line indicates the noise region in which the the dark noise is selected.

5.1.3 The fine gain calibration

Figure 5.5 shows an example of preADC-substracted ADC spectrum of a PMT from a LED calibration run. A quantity called preADC, which is the average of 4 ADC readout values at 100 ns, 75 ns, 50 ns, and 25 ns before the ADC peak, is used to be an approximation for the pedestal and have been subtracted from the ADC peak. The preADC-subtracted ADC spectrum is therefore modeled by a realistic PMT response function [41]. The PMT can be treated as an instrument consisting of two independent parts,

- the photocathode that converts flux of photons into photoelectrons;
- the amplifier (dynode system) which amplifies the initial charge emitted by the photocathode.

The conversion process between photons and photoelectrons can be described by the Poisson distribution:

$$P(n; \mu) = \frac{\mu^n e^{-\mu}}{n!} \quad (5.1)$$

as

$$\mu = mq \quad (5.2)$$

where μ is the mean number of photoelectrons collected by the first dynode, $P(n; \mu)$ the probability that n photoelectrons will be observed when their mean is μ , m the mean number of photons hitting the photocathode, and q the quantum efficiency of the photocathode such that $\mu = mq$. The number of photoelectrons would be amplified many times ($\sim 10^7$) when they go through the PMT dynode system. If the process is initiated by n photoelectrons at the first dynode, the charge distribution at the PMT output can be approximated as a Gaussian distribution,

$$G_n(x) = \frac{1}{\sigma_1 \sqrt{2\pi n}} \exp\left(-\frac{(x - nQ_1)^2}{2n\sigma_1^2}\right) \quad (5.3)$$

where x is the ADC value, Q_1 is the average ADC value at the PMT output and σ_1 is the corresponding standard deviation of the ADC distribution when SPE is emitted by the first dynode. Therefore, the overall PMT response can be described as the convolution of these two functions,

$$R(x) = P(n; \mu) \otimes G_n(x) = \sum_{n=0}^{\infty} \frac{\mu^n e^{-\mu}}{n!} \frac{1}{\sigma_1 \sqrt{2\pi n}} \exp\left(-\frac{(x - nQ_1)^2}{2n\sigma_1^2}\right) \quad (5.4)$$

This function is used to fit the ADC spectrum as shown in Figure 5.5 with Q_1 , σ_1 and μ the fitting parameters. Figure 5.6 shows the distributions of SPE peaks for 192 PMTs in AD1 and AD2 using calibration data taken in Dec. 2011. The ratios of standard deviations and the mean values are roughly 8%. A systematic difference in the average ADC count per SPE between AD1 and AD2 is found, and it could be due to the gain of the PMTs drifting from the early measurement. A slight drift in the calibration as function of time is also observed as shown in Figure 5.7. All channels appear to drift together and the difference between AD1 and AD2 is stable.

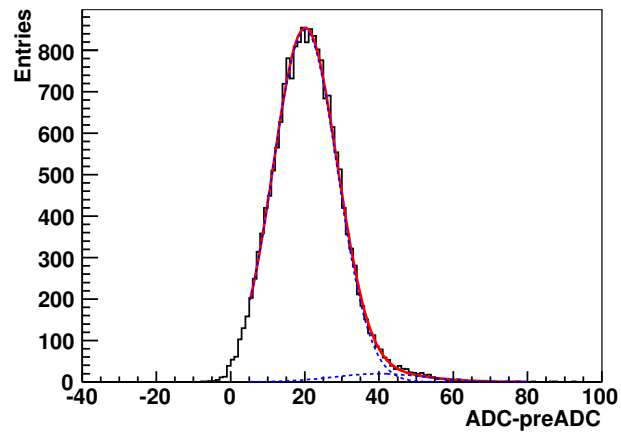


Figure 5.5: Fit to a single PMT SPE distribution using the realistic PMT response function after subtracting the preADC. Dashed curves show the SPE and double PE components. The units are in raw ADC counts.

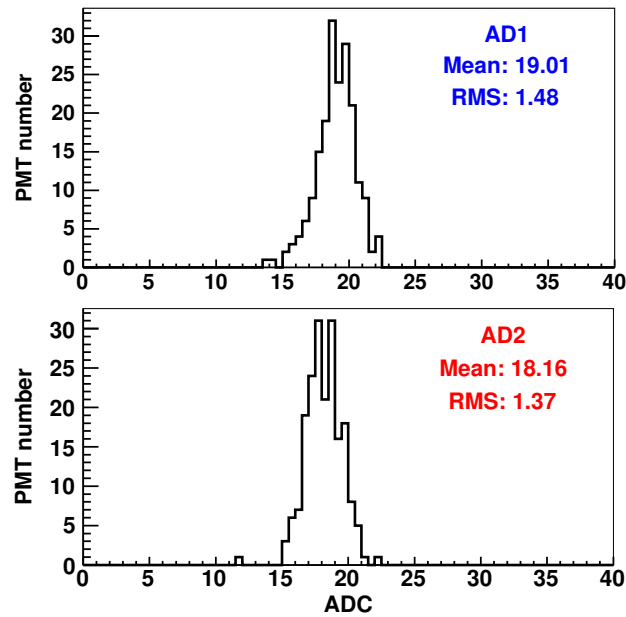


Figure 5.6: Distribution of SPE peaks (Q_1) for AD1 and AD2.

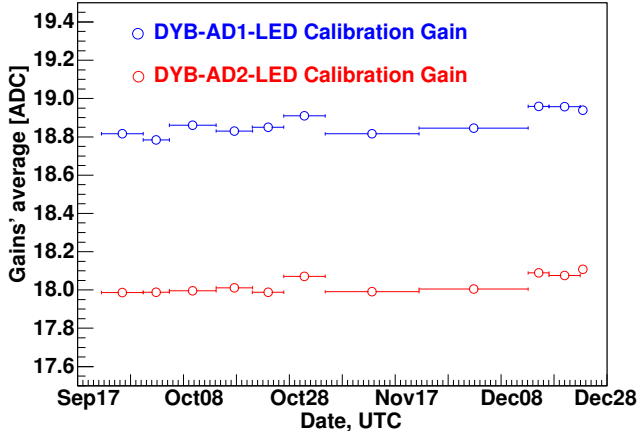


Figure 5.7: The stability of the peak in the SPE distributions averaged in AD1 and AD2 using the calibration data taken in a period of three months.

5.2 Flasher Events

A small number of the AD PMTs spontaneously emit light, due to discharge within the base. These instrumental backgrounds are referred to as flasher events. These flasher events have reconstructed energy ranges from sub-MeV to 100 MeV and are about 5% of all triggers. Flasher events exhibit characteristic charge patterns so that they can easily be removed with the identification of charge pattern.

Two features were observed when a PMT flashes: the flashing PMT typically receives the highest fraction of observed charges, and PMTs on the opposite side of the AD sees a large fraction of light from the flashed PMT. Figure 5.8 shows the charge pattern of a typical flasher event. To reject flasher events, two variables, named *MaxQ* and *Quad*, were created based on the distinctive charge pattern. *MaxQ* is the largest fraction of the total detected charge seen by a single PMT (the "hottest" PMT). There are twenty-four columns of PMTs in an AD that can be divided into four quadrants. The quadrant that contains the hottest PMT is named quadrant 1, and the rest of the quadrants are named 2, 3, 4 clockwise. *Quad* was defined as $Q_3/(Q_2 + Q_4)$, where Q_i is the charge sum of the PMTs in

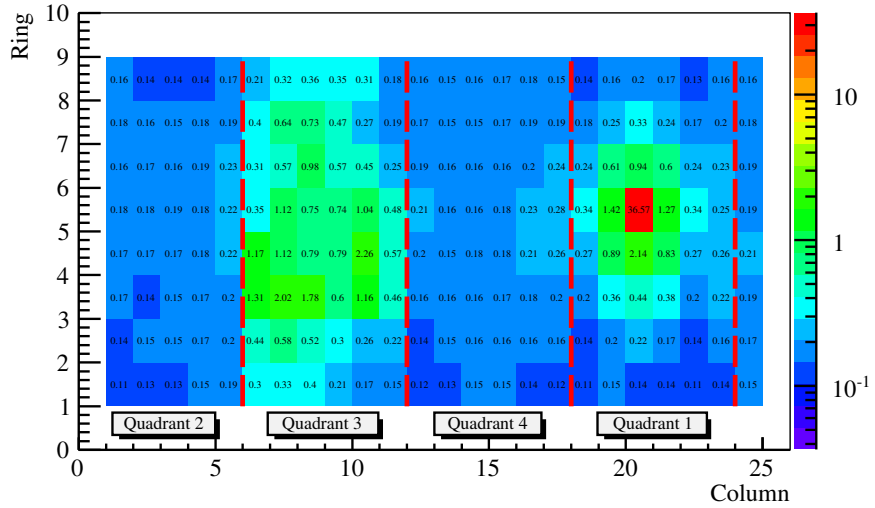


Figure 5.8: An example showing the flasher charge pattern.

the i th quadrant. A flasher event identification variable (FID) was constructed based on $MaxQ$ and $Quad$:

$$FID = \log_{10} [(MaxQ/0.45)^2 + (Quad)^2] \quad (5.5)$$

Event with $FID > 0$ is considered to be a flasher event. Figure 5.9 shows the discrimination of flasher events for the delayed signal of the IBD candidates. For the 2" PMTs, we simply look at the charge: if one 2" PMT receives more than 100 photoelectrons in a trigger, this event would be considered as a flasher event.

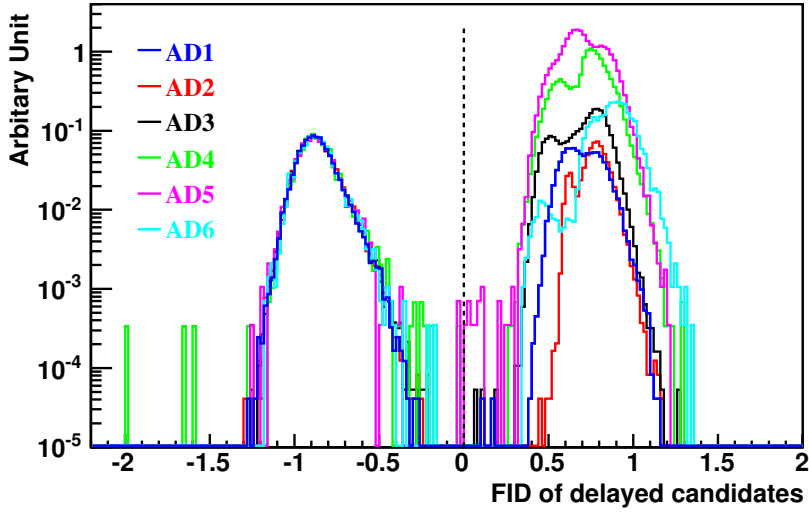


Figure 5.9: Discrimination of flasher events ($FID > 0$) and IBD delayed signals ($FID < 0$). The delayed signals of IBDs have the same distribution for all six ADs while the flashers are different. The $FID < 0$ distributions have been scaled to equal area.

5.3 Vertex Reconstruction

The vertex reconstruction comprises two main steps:

1. the calculation of the “charge-weighted mean” using the information from all fired PMTs, with an empirical correction derived from the MC simulation as the first guessing,
2. and the charge templates algorithm reconstructing the vertex with the first guessing as the initial condition.

5.3.1 Charge-weighted mean with an empirical correction

The first step of the reconstruction is to calculate the charged-weighted mean (center of charge; COC) of the PMT positions, which is defined as

$$\overrightarrow{R_{COC}} = \frac{\sum_i^{PMTs} Q_i \vec{R}_i}{\sum_i^{PMTs} Q_i} \quad (5.6)$$

where i being the index for 8" AD PMTs (192 in total), Q_i being the charge received at each PMT, and \vec{R}_i being the location of the i th PMT in the AD local coordinates.

However, the COC reconstruction gives a large bias on the reconstructed vertex which are toward the center of the AD. A reconstruction biases as functions of R and z are defined as:

$$\Delta R = \frac{\overrightarrow{R_{true}} \cdot \overrightarrow{R_{COC}}}{|\overrightarrow{R_{COC}}|} - R_{COC} \quad (5.7a)$$

$$\Delta Z = Z_{true} - Z_{COC} \quad (5.7b)$$

where $R = \sqrt{X^2 + Y^2}$. From MC simulation, the maps of ΔR and ΔZ with x-axis being R_{COC} and y-axis being Z_{COC} can be obtained as shown in Figure 5.10. Once we have the charged weight mean ($\overrightarrow{R_{COC}}$ and Z_{COC}) and the correction

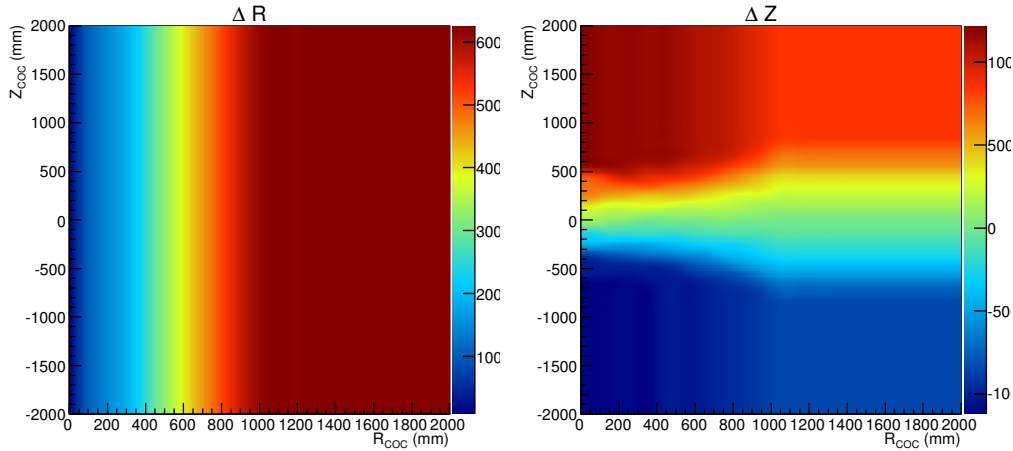


Figure 5.10: Distributions of ΔR (left) and ΔZ (right).

values ($\Delta R(R_{COC}, Z_{COC})$ and $\Delta Z(R_{COC}, Z_{COC})$). The corrected vertex position

from COC with MC correction is given as:

$$X_{COR} = [R_{COC} + \Delta R(R_{COC}, Z_{COC})] \cdot \frac{X_{COC}}{R_{COC}} \quad (5.8a)$$

$$Y_{COR} = [R_{COC} + \Delta R(R_{COC}, Z_{COC})] \cdot \frac{Y_{COC}}{R_{COC}} \quad (5.8b)$$

$$Z_{COR} = Z_{COC} + \Delta Z(R_{COC}, Z_{COC}). \quad (5.8c)$$

5.3.2 Charge templates

The charge templates are constructed by simulating the IBD positrons inside the OAV at AD1 in EH1. The MC sample is divided into $20 \times 20 \times 24$ bins in cylindrical coordinate (R^2, Z, ϕ) , where $R^2 = X^2 + Y^2$ and $\phi = \arctan(y/x)$. To increase MC statistics, we added all 24 ϕ bins by shifting appropriate number of PMT columns and construct the templates. Figure 5.11 shows the example of the PMT charge distribution for two different vertex location. These charge distributions exhibit strong correlation to the true vertex position. One can estimate the vertex position

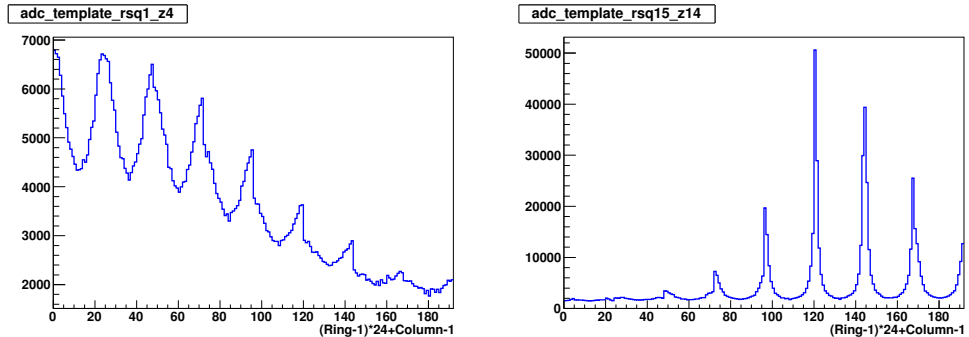


Figure 5.11: Examples for charge distribution for each PMT. The left figure shows the distribution for $0.2 < r^2 < 0.4(m^2)$ and $-1.2 < z < -1.0(m)$ and the right one shows that for $3.0 < r^2 < 3.2(m^2)$ and $0.8 < z < 1.0(m)$

by performing a χ^2 minimization defined as:

$$\chi^2 = 2 \sum_i^{PMTs} \left[N_i^{exp} - N_i^{obs} + N_i^{obs} \ln \left(\frac{N_i^{obs}}{N_i^{exp}} \right) \right]. \quad (5.9)$$

where N_i^{obs} and N_i^{exp} are the observed and the expected charge (in p.e.) of the i -th PMT. After the bin with minimum χ^2 is found, the vertex position can be further refined by interpolating the χ^2 values at neighboring grid points.

5.4 Energy Reconstruction

The energy reconstruction comprise three main steps:

1. The determination of the total charge deposited in the detector as seen by the PMTs,
2. the conversion between the total charge to a visible energy, and
3. the non-uniformity correction to the visible energy.

These three steps are described in the following subsections.

5.4.1 Calculation of the total charge

The charge collected in a trigger could come from hits that are not directly related to the physical event that caused the trigger. Since the electronics have rather consistent processing time, the time from forming a trigger to reading out is roughly constant for each trigger. Hits that are coming from the an actual triggering event would tend to cluster in time. These hits can be selected by summing the charges of only those hits in the window between -1650 and -1250 ns. The charge sum is called "nominal charge", and will be used in the energy reconstruction.

5.4.2 Visible energy

Once we get the total charge of this event, we could convert it to the visible energy (E_{vis}) by dividing by the energy scale constant as shown in Equation 5.10.

$$E_{vis} = \frac{Q_{total}}{C}, \quad (5.10)$$

where Q_{total} is the total charge that observed by the PMTs in the AD and C is the energy scale constant. The energy scale constant can be determined by analyzing the Gd-capture spallation neutrons.

Before selecting the Gd-capture spallation neutron, one must define the muon event. A trigger is tagged as a muon if the nominal charge is more than 3000 photoelectrons. After removing the flasher events, the Gd-capture spallation neutrons can be selected from events in signal region ($20\mu s < \Delta t < 1000\mu s$) subtracted by those in the background region ($1020\mu s < \Delta t < 2000\mu s$). The photoelectron spectrum of the Gd-capture spallation neutron is then fitted with a double Crystal Ball function. The Crystal Ball function is defined as,

$$f(x; \alpha, n, \bar{x}, \sigma) = \begin{cases} N \exp \frac{(x-\bar{x})^2}{2\sigma^2}, & \frac{x-\bar{x}}{\sigma} > -\alpha \\ NA \left(B - \frac{x-\bar{x}}{\sigma} \right)^{-n}, & \frac{x-\bar{x}}{\sigma} < -\alpha \end{cases} \quad (5.11a)$$

$$A = \left(\frac{n}{|\alpha|} \right)^n e^{-\frac{|\alpha|^2}{2}}, \quad (5.11b)$$

$$B = \frac{n}{|\alpha|} - |\alpha|. \quad (5.11c)$$

The two Crystal Ball functions fit the peak contributed from neutron captured by two individual isotopes: ^{155}Gd and ^{157}Gd . The properties and the light yields are described in Table 5.1. An example of Gd-capture neutron peak fitted with a double Crystal Ball function is shown in Figure 5.12.

Isotope	^{155}Gd	^{157}Gd
Isotopic Abundance (%)	14.80	15.65
Neutron Capture Cross-section (barn)	60900	254000
Neutron Capture Peak (MeV)	7.937	8.536

Table 5.1: caption

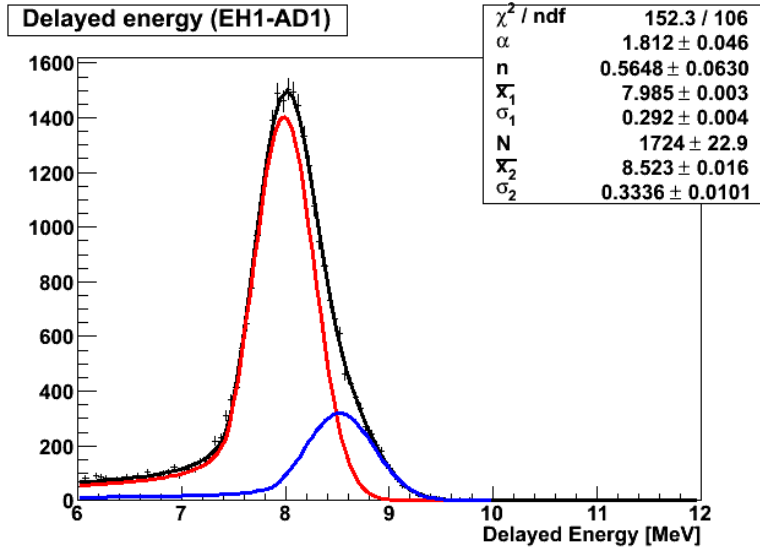


Figure 5.12: Gd-capture neutron peak fitted with a double Crystal Ball function. The red curve is the fitting result of ^{155}Gd , while the blue one is that of ^{157}Gd . The black one is the sum of those two.

5.4.3 The non-uniformity correction

The E_{vis} seems to have a dependence on position. The variation of E_{vis} with position for ^{60}Co sources from all three ACUs is shown in Figure 5.13. The detector energy spectrum can be made more uniform by applying position corrections to the visible energy of an event. The position-based correction is described as:

$$E_{rec} = 8.05/R(r) \times 8.05/R(z) \times E_{vis}, \quad (5.12)$$

where $R(r)$ and $R(z)$ are the energy response functions in terms of r and z (both in units of meters):

$$R(r) = 7.74687 - 0.129958r + 0.3355034r^2 - 0.0337577r^3, \quad (5.13a)$$

$$R(z) = 8.09949 - 0.11702z - 0.124515z^2 + 0.0245703z^3. \quad (5.13b)$$

The variation of E_{rec} after the non-uniformity correction is less than 2%, as

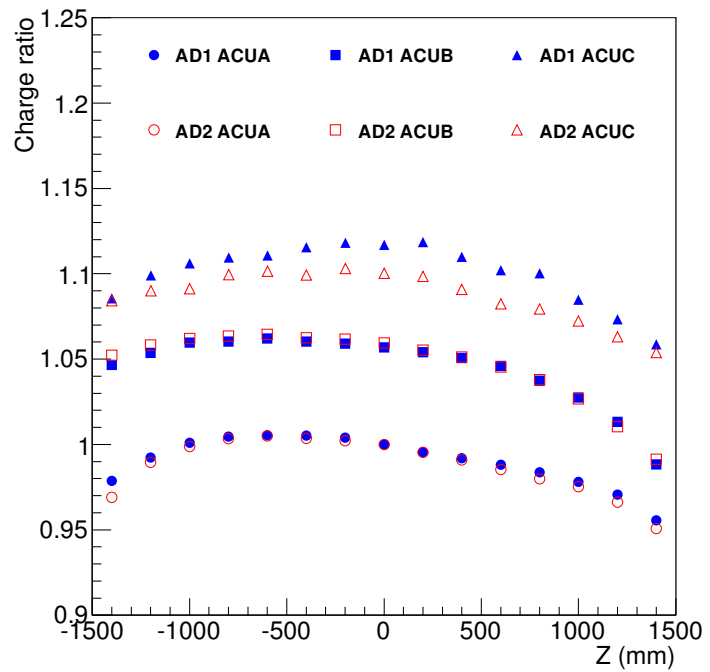


Figure 5.13: The variation of E_{vis} for the ^{60}Co sources as a function of position in ADs. The charge ratio denotes $E_{vis}(Z)/E_{vis}(Z = 0)$. The R -positions of each ACU are 0 m (ACU A), 1.35 m (ACU B), and 1.77 m (ACU C).

shown in Figure 5.14.

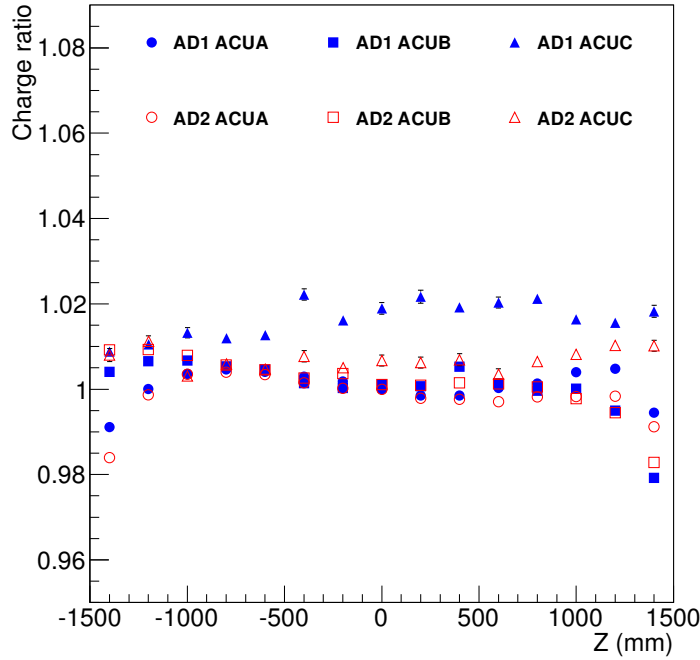


Figure 5.14: The variation of E_{rec} for the ^{60}Co sources as a function of position in ADs. The charge ratio denotes $E_{rec}(Z)/E_{rec}(Z = 0)$. The R -positions of each ACU are 0 m (ACU A), 1.35 m (ACU B), and 1.77 m (ACU C).

5.4.4 Energy resolution

The resolution of the reconstructed energy is obtained by measured the energy peak widths of ^{60}Co , ^{68}Ge and AmC sources, neutron captured by H and Gd in AD1 and AD2. The resoultion curve is fitted to be $(7.5/\sqrt{E(\text{MeV})} + 0.9)\%$, as shown in Figure 5.15.

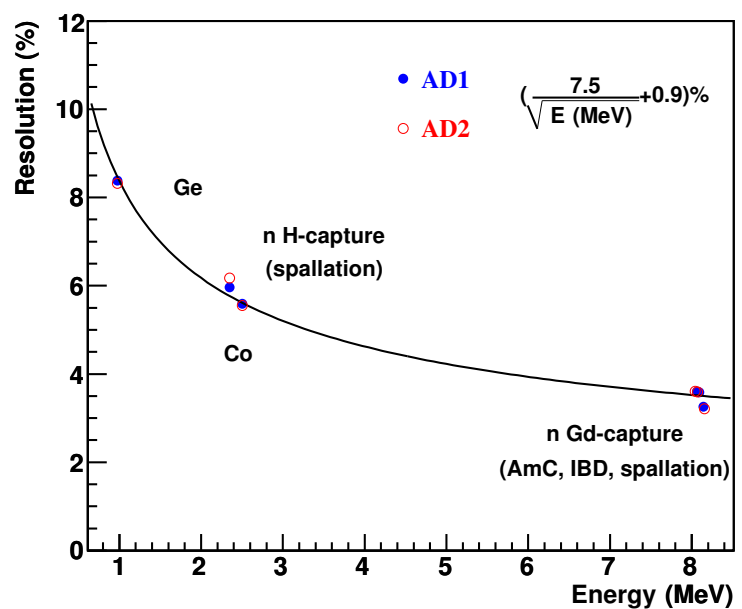


Figure 5.15: Resolution of reconstructed energy.

Chapter 6

Muon-induced Neutron

The main purpose of this thesis is the measurements of the muon-induced neturon yields in the 3 experimental halls of the Daya Bay experiment. The production mechanisms of the muon-induced neturon will be discussed in Section 6.1. To calculate the efficiencies and the relevent correction factors, the detector simulaiton is needed and will be presented in Section 6.2. In Section 6.3, the measuements of muon-induced neutron yields and the comparison with other experimental results will be discussed.

6.1 Neutron Production

Cosmic ray muons produce neutrons through several different mechanisms. The processes contributing to this neutron production include the following;

1. Photo-nuclear interactions: As a muon passes through matter, real photons and electrons from bremsstrahlung and pair production released and produce particle shower. In general, the cross sections associated with electromagnetic shower are well known.
2. Muon Spallations: Neutrons produced in muon spallation involve the exchanged of a virtual photon as the muon passes through matter. Figure 6.1

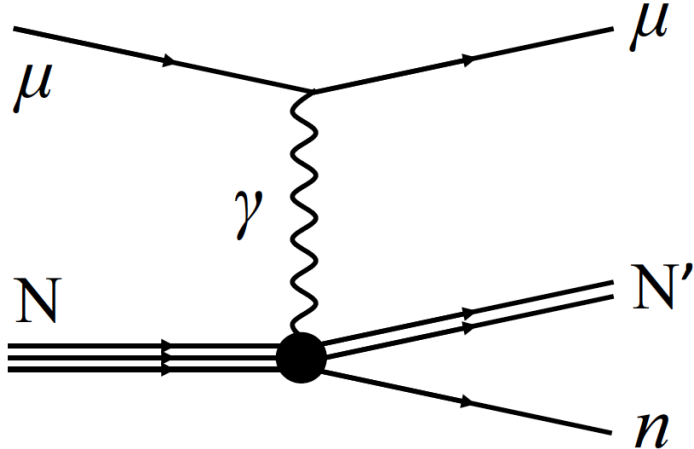


Figure 6.1: The Feynman diagram of a muon spallation process.

shows the lowest-order Feynman diagram for this interaction.

3. Elastic scattering: The bound neutrons escape nuclei due to muon scattering with such neutrons.
4. Secondary neutrons: the neutron production from the cascade neutrons produced by other processes.
5. μ^- capture on nuclei: Low energy μ^- undergoes nuclear capture via the weak charged-current process and produces neutrons,

$$\mu^- + A(Z, N) \rightarrow \nu_\mu + A(Z - 1, N + 1). \quad (6.1)$$

Processes 1 to 4 describe neutrons generated by through-going muons. For those kind of neutrons, the production rate can be modeled by the following empirical formula [11],

$$Y_n = 4.14 \times E_\mu^{0.74} \times 10^{-6} \text{ } n/\mu/(\text{g/cm}^2), \quad (6.2)$$

with Y_n being neutron production rate in a unit of $n/\mu/(\text{g/cm}^2)$, E_μ the average energy of the cosmic-ray moun in the underground laboratory in a unit of GeV.

The energy spectrum of muon-induced neutron is parameterized as [11],

$$\frac{dN}{dE_n} = A \left(\frac{e^{-7E_n}}{E_n} + (0.52 - 0.58e^{-0.0099E_\mu}) e^{-2E_n} \right), \quad (6.3)$$

with E_n being the neutron energy. The angular distribution,

$$\frac{dN}{d\cos\theta} = \frac{1}{(1 - \cos\theta)^{0.6} + 0.699E_\mu^{-0.136}}. \quad (6.4)$$

The neutrons produced by μ^- captures are only dominant for shallow depths ($\simeq 100$ m w.e.) and can be easily identified and eliminated by the muon veto detectors in deep underground. They will not be discussed in the later analysis.

6.2 Simulation Setup

The muon-induced neutron simulation comprises two parts: one is the simulation of muon flux, which studies the transportation and energy loss of muon from the atmosphere to the underground laboratory, the other is the simulation of muon-induced neutron in the underground laboratory.

6.2.1 Muon simulation

The muon flux, energy spectrum and angular distribution in the 3 experimental halls of the Daya Bay experiment was calculated using MUSIC [54]. The energy spectrum of muon at the sea level are generated according to the modified Gaisser formula as [33]

$$\frac{dI}{dE_\mu d\cos\theta} = 0.14 \left(\frac{E_\mu}{\text{GeV}} \left(1 + \frac{3.64 \text{ GeV}}{E_\mu (\cos\theta^*)^{1.29}} \right) \right)^{-2.7} \left[\frac{1}{1 + \frac{1.1E_\mu \cos\theta^*}{115 \text{ GeV}}} + \frac{0.054}{1 + \frac{1.1E_\mu \cos\theta^*}{850 \text{ GeV}}} \right] \quad (6.5)$$

where the polar angle θ^* is defined as a function of the zenith angle θ ,

$$\cos \theta^* = \sqrt{\frac{(\cos \theta)^2 + P_1^2 + P_2(\cos \theta)^{P_3} + P_4(\cos \theta)^{P_5}}{1 + P_1^2 + P_2 + P_4}} \quad (6.6)$$

The parameters are determined to be $P_1 = 0.102573$, $P_2 = -0.068287$, $P_3 = 0.958633$, $P_4 = 0.0407253$, and $P_5 = 0.817285$, by using CORSIKA [55] to simulate the muon production in the atmosphere.

The muon flux at the sea level is then input in MUSIC together with the amount of rocks at different angle in which the muons have to penetrate. The amount of rocks at different angle is calculated from the topographic map in the Daya Bay area as shown in Figure 6.2. Table 6.1 shows the simulated muon flux

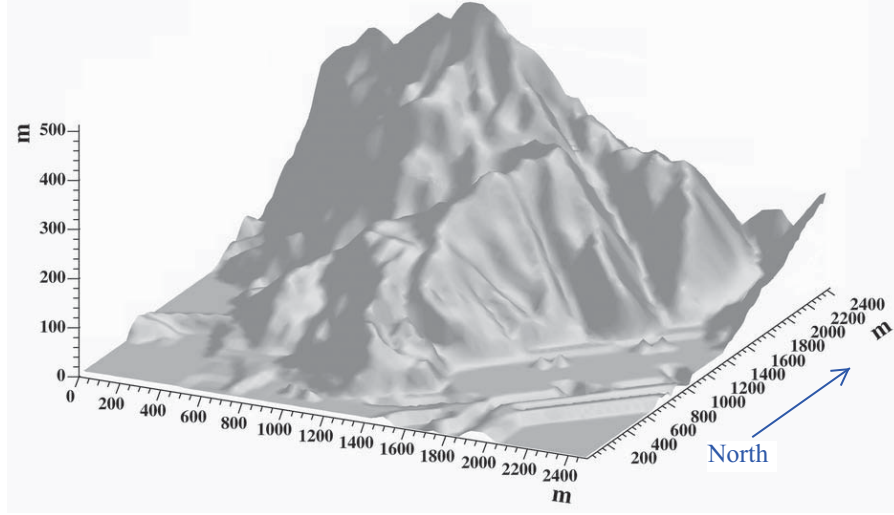


Figure 6.2: The 3D topographic map of the Daya Bay area. The tunnel entrance is at the base of the mountain at the left side of the figure.

and the average energy at each EH [45], and Figures 6.3 and 6.4 show the muon angular and energy distributions at each EH.

The simulation error from MUSIC is about 1%. Considering the uncertainties

	Overburden	R_μ	E_μ
EH1	250	1.27	57
EH2	265	0.95	58
EH3	860	0.056	137

Table 6.1: The overburden (m w.e.), the muon flux R_μ (Hz/m²) and the average energy E_μ (GeV) of the 3 EHs from MUSIC simulation.

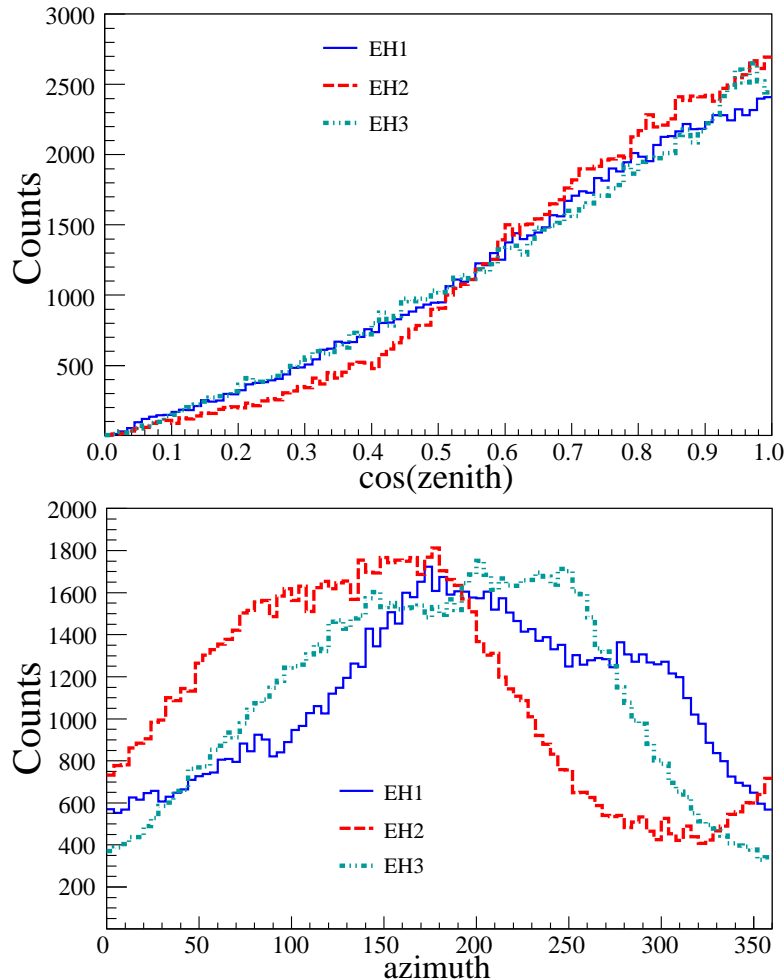


Figure 6.3: Simulated muon trajectories. The upper figure shows the cosine distribution of zenith angle; while the bottom figure shows the azimuthal angular distribution.

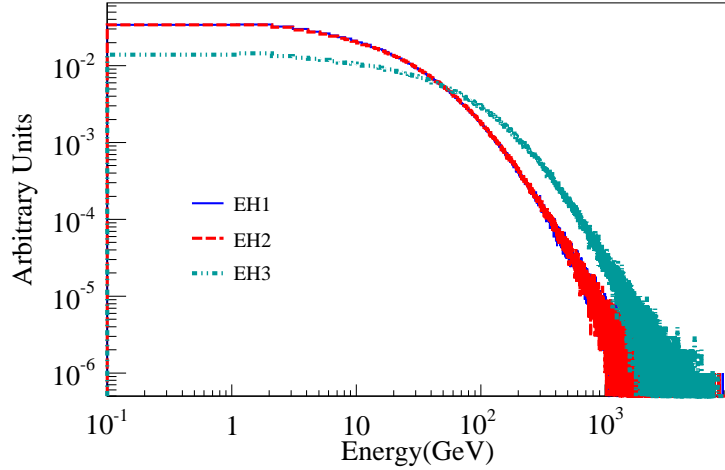


Figure 6.4: Simulated muon energy distributions.

in mountain profile mapping, rock composition, and density profiling, the total error in the simulated muon flux is about 10% [56], and the total error in the simulated average muon energy is assigned 5% conservatively [57].

Since the modified Gaisser formula only models the muon energy, the charge of cosmic-ray muon is given by the $\pi - k$ model of muon charge ratio [44],

$$\frac{N_{\mu^+}}{N_{\mu^-}} = \left[\frac{f_{\pi^+}}{1 + \frac{1.1E_{\mu^+} \cos \theta}{115 \text{ GeV}}} + \frac{0.054 f_{K^+}}{1 + \frac{1.1E_{\mu^+} \cos \theta}{850 \text{ GeV}}} \right] / \left[\frac{(1 - f_{\pi^+})}{1 + \frac{1.1E_{\mu^-} \cos \theta}{115 \text{ GeV}}} + \frac{0.054(1 - f_{K^+})}{1 + \frac{1.1E_{\mu^-} \cos \theta}{850 \text{ GeV}}} \right]. \quad (6.7)$$

where $f_\pi = 0.55$, $f_k = 0.67$ as shown in Figure 6.5.

In the later analysis, the zenith angle in Equation 6.7 is set to be vertical ($\cos \theta = 1$) for simplicity.

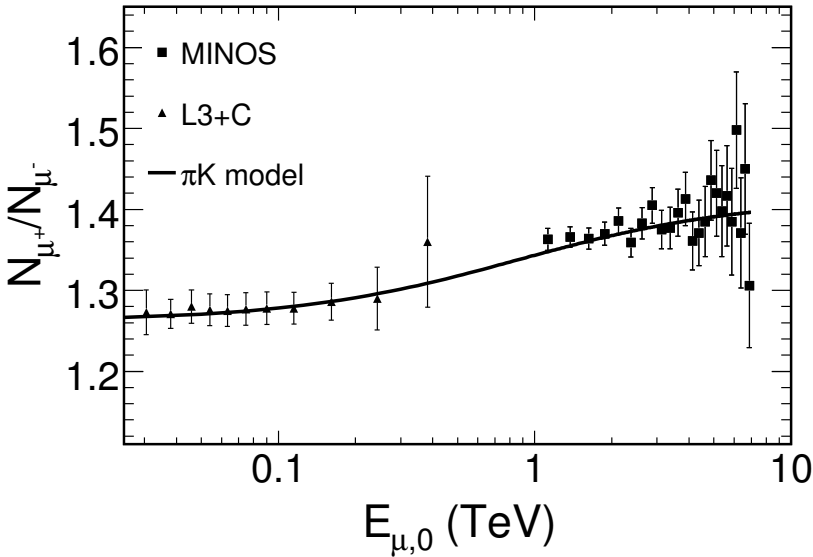


Figure 6.5: The fitting of the $\pi - k$ model to the data of MINOS and L3+C [44].

6.2.2 Simulation of neutron production and transportation

Once we have realistic muon spectra, we are ready to perform the muon-induced neutron simulation. The official detector simulation tool is based on GEANT4. The muon cascade simulation in GEANT4 could produce hundreds and thousands of photons which cost much CPU time. A fast simulation is employed in this study to avoid the time-consuming muon-cascade simulation. The procedure of the fast simulation can be separated into two stages:

1. At first, we generate the neutron samples which are induced by realistic muon flux injecting into a simple geometrical region. This stage is done by FLUKA [10].
2. We then put the neutron samples along the muon track into a realistic detector region. This stage is done by GEANT4 [12].

6.2.2.1 FLUKA simulation setup: generating neutron samples

FLUKA is a fully integrated particle physics Monte Carlo simulation package based predominantly on original and well-tested microscopic models. The models are benchmarked and optimized by comparing to experimental data at the single interaction level. The physics models in FLUKA are fully integrated into the code and modifications or adjustments are not available at user level. A list of benchmark results relevant to the simulation of deep underground cosmogenic backgrounds is described in [58].

Details of the physics models implemented in FLUKA with focus on hadronic interactions and the FLUKA specific nuclear interaction model PEANUT can be found in [59, 60, 61, 62], while a description of the approach for muon interactions in FLUKA is given in [11]. A validation of the FLUKA Monte Carlo code for predicting induced radioactivity is given, for instance, in [63].

The version of FLUKA used for this study is FLUKA 2011.2. The simulation was performed using the FLUKA default setting PRECISIO(n). In addition, photo-nuclear interactions were enabled through the FLUKA option PHOTONUC and a more detailed treatment of nuclear de-excitation was requested with the EVAPORAT(ion) and COALESCE(nce) options. These enable the evaporation of heavy fragments ($A > 1$) and the emission of energetic light fragments, respectively. The treatment of nucleus-nucleus interaction was turned on for all energies via the option IONTRANS and radioactive decays were activated through the option RADDECAY.

In these simulations, muons with a realistic energy spectrum and charge ratio are tracked in a cylindrical detector with a length and diameter of 50 m as shown in Figure 6.6. The detector is filled with the Gd-doped liquid scintillator used in the Daya Bay experiment, and the composition is described in Table 6.2. The simple geometry was chosen to eliminate geometry effects. As shown in Figure 6.7, the particle shower from the muon requires several meters to develop. The particle shower then decreases as the distance that muons penetrate deeper

into the medium. As the penetration distance increases, the mean muon energy also decreases. The neutron should be chosen at a limited distance range so that the muon energy-loss is small and the initial energy spectrum can be treated as unaltered by the propagation. For these reasons, the neutrons produced between 10 and 20 m are chosen for analysis.

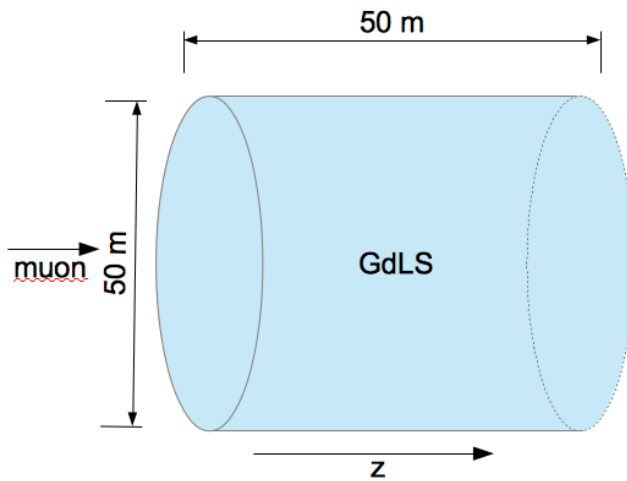


Figure 6.6: The scheme of the FLUKA simulation. Muons are injected into a cylinder filled with Gd-doped liquid scintillator.

Gd-doped LS	
Density	0.8602 g/cm ³
Element	Fraction of Mass
Carbon	0.87705
Hydrogen	0.12051
Oxygen	0.00109
Gadolinium	0.00103
Nitrogen	0.00027
Sulfur	0.00005

Table 6.2: The composition of Gd-doped LS.

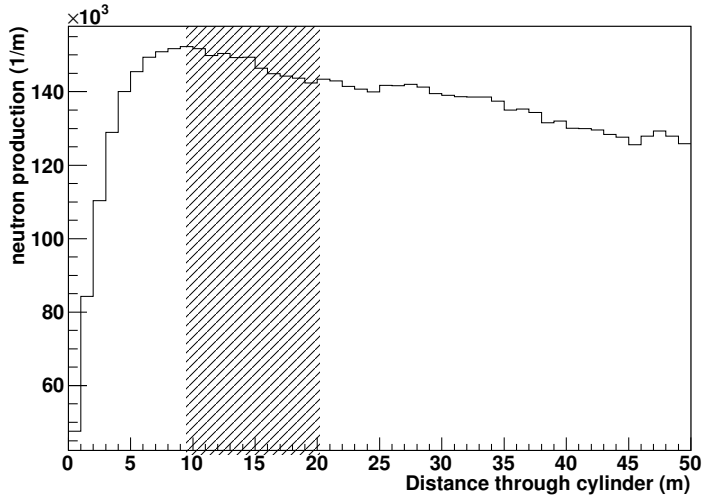


Figure 6.7: The neutron production rate as a function of muon track length. We injected 25 million muons with realistic spectrum for this simulation. Neutron samples are selected in the shadow region.

For extracting the neutrons from the simulation, care must be taken in order not to double-count neutrons that are involved in reactions like $X(n, nn')X'$. Therefore, if such an interaction occurs, the final state neutron with the highest energy is considered as the original neutron and not to be added to the tally.

Figures 6.8 and 6.9 show an example of the neutron energy spectrum and angular distribution relative to the muon direction in EH1. Comparing the energy spectrum with Equation 6.3, they agree with each other for energy larger than 10-50 MeV [11][46][50].

6.2.2.2 GEANT4 simulation setup: a semi-realistic simulation

GEANT4 is a toolkit for the simulation of the passage of particles through matter. Its areas of application include high energy, nuclear and accelerator physics, as well as studies in medical and space science. Comparing with FLUKA, GEANT4 offers alternative models to deal with physics processes which can be selected according to the requirement of each simulation (e.g. the trade-off between computational

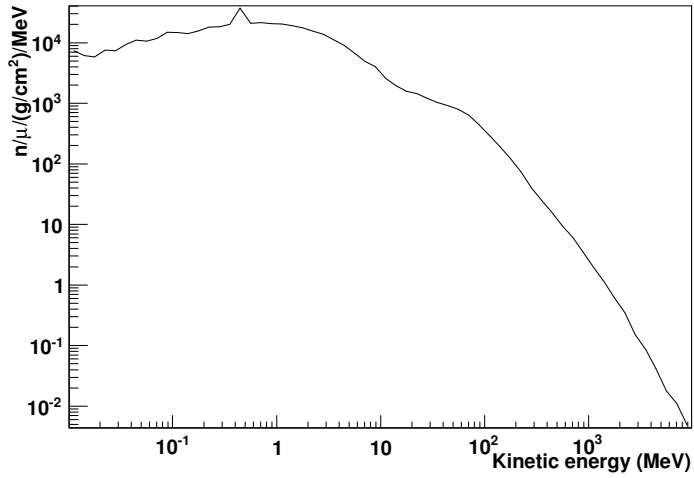


Figure 6.8: The kinetic energy spectrum of muon-induced neutron in EH1.

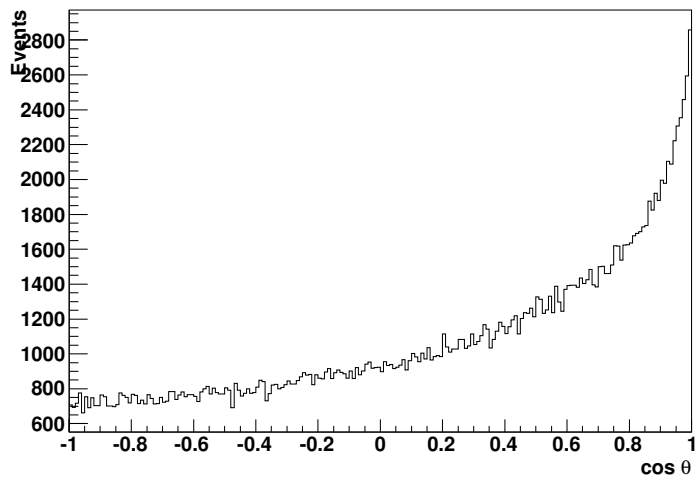


Figure 6.9: The angular distribution of muon-induced neutron in EH1. The angle is relative to the muon direction.

efficiency and the accuracy of the simulation).

The version of GEANT4 in use is 4.9.2.p01. The physics processes describing interactions of muons and their associated showers are the following:

- muon-induced spallation: available for muon with energy from 1 GeV to 1 PeV.
- photo-production (γ inelastic scattering): A chiral-invariant phase-space (CHIPS) model is used below 3.5 GeV, while a theoretical quark-gluon string (QGS) model is used for energies between 3 GeV and 100 TeV.
- hadron interaction: the QGS model is used at high energy ($12 \text{ GeV} < E < 100 \text{ TeV}$). The binary cascade model is used at low energy ($65 \text{ MeV} < E < 9.9 \text{ GeV}$) for protons and neutrons; while the pions are described by the Bertini model at low energy ($0 < E < 9.9 \text{ GeV}$). For the intermediate energy range, the LEP model is used;
- de-excitation of the residual nucleus: it is included for describing γ and fragment evaporation, fission, Fermi break-up and multi-fragmentation;
- neutron interactions: a data-driven model are used for neutron below 20 MeV, and the thermal neutron scattering ($E < 4 \text{ eV}$) is included by considering the molecular binding energy of the scattering nuclei.

For the neutron and muon capture processes, the validations and the corresponding corrections are implemented based on the measured gamma spectra. The optical properties of the detector components were determined from measurements of attenuation lengths, refraction indices of all liquids and the acrylic components, time constants and photon emission spectra of GdLS, LS and mineral oil, and the reflectivity of the reflectors and other detector materials.

In this stage of simulations, we simply give the tracks of muons without simulating their interactions and propagations in a realistic setup of detector geometry (for detailed description of detectors, see Chapter 3). The resulting neutrons from

FLUKA simulation are then put along the muon track if these muons are triggered. Since the interactions of muon are not simulated in GEANT4, a muon is treated as a triggered one if the calculated “deposited energy” in the AD is larger than 20 MeV. The calculated “deposited energy” of muon in MC is defined as the multiplication of the track length in the liquid scintillator and the energy loss per unit track length. An approximate numerical formula for ionization energy loss [51] of muon in the liquid scintillator is

$$\frac{dE}{dX} \approx - \left(1.9 + 0.08 \ln \left(\frac{E_\mu}{m_\mu} \right) \right) \quad (\text{MeV}/(\text{g/cm}^2)) \quad (6.8)$$

where E_μ is the muon energy and m_μ is the muon mass.

The lateral profile of the neutron production is also simulated by FLUKA. The average lateral distances to the muon track are 36.57, 36.41, and 39.35 cm in the 3 EHs , respectively. Figure 6.10 shows the lateral distribution of muon-induced neutron in the EH1.

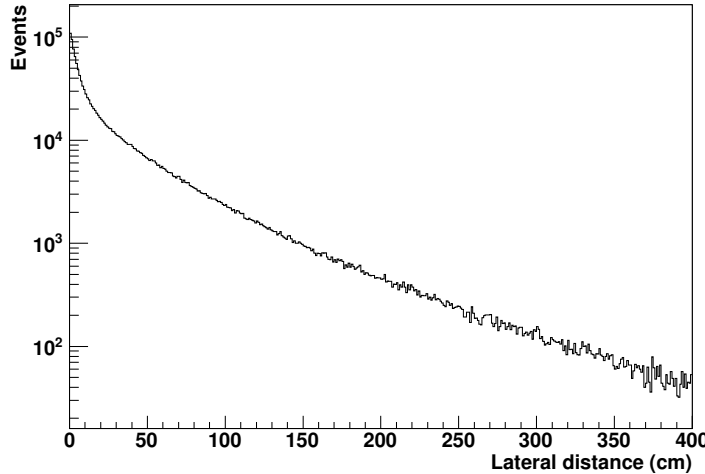


Figure 6.10: The lateral profile for neutron produced by cosmic muons in a liquid scintillator in EH1.

Reactions involving neutron-induced neutron also occur in GEANT4 simula-

tion. However, those neutrons are already taken into account in FLUKA simulation. To make discussion easier, we define those neutrons which are generated in FLUKA simulation and subsequently put in GEANT4 simulation as injections, and those neutrons which are generated by the injections in GEANT4 simulation as productions. To avoid overcounting the neutron-induced neutrons, two methods for estimating the number of neutrons are used in the analysis:

1. We put all kind of injections in GEANT4 simulation, but only take into account the injections in GEANT4. We ignore the productions since the neutron-induced neutrons is already included in injections. In this method, the production of neutron-induced neutron is already simulated in FLUKA.
2. We only put the not-neutron-induced injections, and take into account the injection neutrons and their production ones. In this method, the production of neutron-induced neutron is simulated in GEANT4.

In the following analysis, Method 1 and 2 will be used to calculate the spill in/out correction factor and the corresponding systematic uncertainty, and Method 2 will be used to calculate the rest efficiencies.

6.2.2.3 Brief introduction to electronics simulation

The details of the electronics simulation can be found in Reference [49]. Using the timing and number of photoelectrons generated in PMTs, an analog signal pulse for each PMT was generated and tracked through the digitization process, taking into account the non-linearity, dark rate, pre-pulsing, after-pulsing and ringing of the wave form. The simulated analog pulse was then used as the input for the trigger system simulation for each sub-detector.

6.3 Measurement of muon-induced neutron production

To understand the production rate of the muon-induced neutron in the Daya Bay experiment, the GdLS regions in the ADs deployed in the 3 experimental halls are treated as the targets. When a cosmic-ray muon passes through the AD, the neutrons are produced by the interactions of muon with the surrounding matter. These neutrons are slowed down by the thermalization process in a few microseconds ($\sim 28 \mu\text{s}$) and are eventually captured on Gd in the GdLS region. The gamma rays are emitted with the characteristic energy $\sim 8 \text{ MeV}$, as illustrated in Figure 6.11.

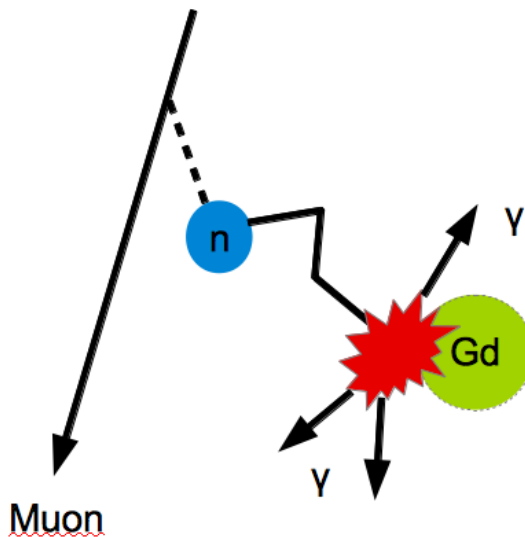


Figure 6.11: The illustration of muon-induced neutron captured on Gd

In this study, the neutron signature is a delayed coincidence in time between the prompt trigger from muon track and the delayed one from the captured gammas.

Events are identified as cosmic-ray muons passing through the AD by the following selection criteria,

- AD muon (μ_{AD}): the energy response (E) is greater than 20 MeV;
- WP muon (μ_{WP}): either the number of fired PMTs in IWS or those in OWS are greater than 12;
- μ_{AD} and μ_{WP} are within $0.3 \mu\text{s}$.

After applying the flasher removal which is described in Section 5.2, events fulfilled the following criteria are selected as candidates for muon-induced neutrons captured on Gd (nGd in short),

- the time since the last muon (dT) must be located in the signal time window which is defined as $10 \mu\text{s} < dT < 300 \mu\text{s}$, and
- $6 \text{ MeV} < E < 12 \text{ MeV}$.

The reason for setting a lower timing cut $10 \mu\text{s}$ is to suppress the effect of retrigger and ringing at the very beginning time period after the passing of muon, as depicted in Figure 6.12.

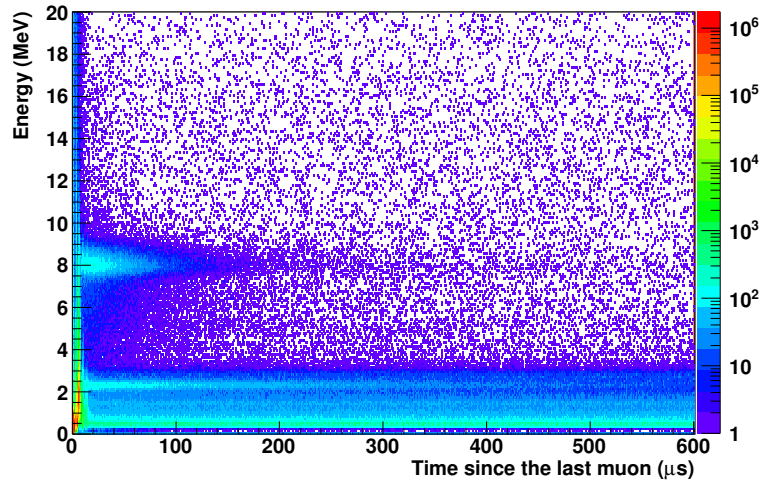


Figure 6.12: A 2D map showing the time since the last muon versus the energy of the spallation products.

There are two kinds of backgrounds for this analysis of muon-induced neutrons,

- accidental coincidences due to the radioactivity;
- neutrons associated with the local radioactivity.

To remove the background due to the accidental coincidences, the background time window is defined as $310 \mu\text{s} < dT < 600 \mu\text{s}$. By subtracting events in the background time window from those in the signal time window (side-band subtraction in short), the accidental background can be eliminated. Neutrons associated with the local radioactivity are produced mainly via (α, n) reactions, initiated by α -particles from U/Th which are contained in the surrounding materials in EH. Neutrons from spontaneous fission of ^{238}U also contribute at low energies. The background due to neutrons associated with the local radioactivity is estimated to be negligible after the prompt energy cut ($E > 20 \text{ MeV}$).

To prevent spallation products from other muons falling on the signal time window, an isolation cut is applied such that there are no additional muon events (μ_{AD} or μ_{WP}) before $300 \mu\text{s}$ and after $600 \mu\text{s}$ of this muon event.

6.3.1 The neutron yield

The neutron yield Y_n can be expressed as,

$$Y_n = \frac{N_n \cdot C_p}{N_\mu \cdot \langle X \rangle \cdot \epsilon_{Gd} \cdot \epsilon_{\text{flasher}} \cdot C_{in/out} \cdot \epsilon_E \cdot \epsilon_t}, \quad (6.9)$$

where Y_n is the muon-induced neutron production rate in a unit of $n/\mu\text{/}(g/\text{cm}^2)$. N_n is the detected number of nGd candidates, and N_μ is the number of muons that passes the selection and isolation cuts. C_p is the correction factor for taking into account the pile-up events. $\langle X \rangle$ is in a unit of g/cm^2 and denotes the average track length muon traveling through the Gd-doped liquid scintillator in AD. $\epsilon_{\text{flasher}}$ represents the cut efficiency of the flasher removal. ϵ_{Gd} is the Gd-capture ratio efficiency. Neutrons with high kinetic energy from outside could sneak into the GdLS region and are finally captured. Furthermore, neutrons produced in GdLS region with high kinetic energy could escape from the AD. $C_{in/out}$ denotes the

correction factor for the spill in/out effect. ϵ_E is the energy cut efficiency and ϵ_t is the timing cut efficiency.

N_n and N_μ are determined directly from data, while a correction is imposed on the estimation of N_μ . C_p is given by a theoretic calculation, and its uncertainty is obtained from the comparison between the measurement and calculation. Quantities $\langle X \rangle$, ϵ_E , ϵ_t and ϵ_{Gd} are determined by a data-constrained MC simulation. For $C_{in/out}$, it is obtained solely by MC simulation. The determination of each of the quantity on the right hand side of Equation 6.9 is described in the followings.

The data for this analysis is from December 24, 2011 to July 28, 2012. 6 ADs deployed in 3 EHs are in use.

6.3.1.1 Estimation of N_μ

After applying the muon selection and isolation cuts, the number of muons N_μ and the energy spectrum are as shown in Figure 6.13. Due to the limitation of

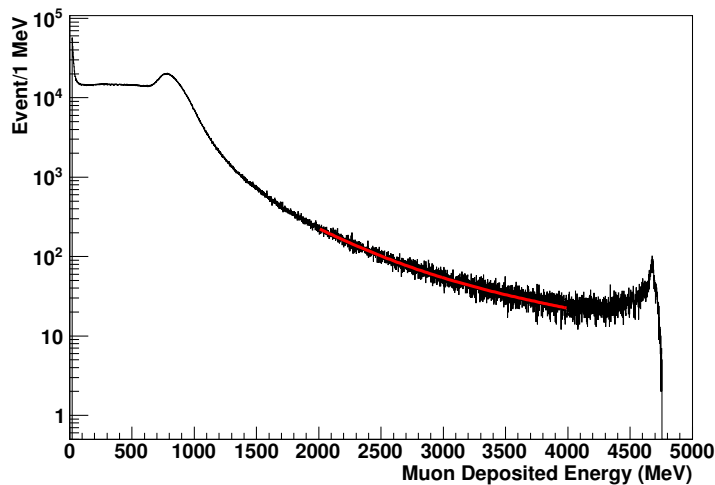


Figure 6.13: The deposited energy spectrum of muon candidates in EH3-AD3. The red curve indicates the fitted function.

FEE, any event with nominal charge $\gtrsim 7.8 \times 10^5$ p.e. is squeezed into the last ADC channel. As we can see in Figure 6.13, the energy spectrum rises up at the

high energy edge. To correct the distortion of high energy tail, we fit the energy spectrum from 2 GeV to 4 GeV with a double exponential function,

$$\Phi(E) = N_1 e^{-p_1 x} + N_2 e^{-p_2 x} \quad (6.10)$$

After applying the fit, we extrapolate the fitted function to a very high energy (100 GeV in this study). To estimate the number of muons, we simply count the number of event for $E < 2$ GeV and the integration of the fitted function is employed for estimating the number of muons for $E > 4$ GeV. Table 6.3 summarizes the number of muons in the ADs of 3 EHs.

Detector	N_μ	$\sigma_{stats.} (\%)$	$\sigma_{syst} (\%)$
EH1-AD1	284262437	0.0059	0.0038
EH1-AD2	284207796	0.0059	0.0022
EH2-AD1	221364195	0.0067	0.0026
EH3-AD1	16480324	0.0246	0.0139
EH3-AD2	16582316	0.0246	0.0900
EH3-AD3	16489881	0.0246	0.0230

Table 6.3: The number of the isolated muon candidates in the ADs of 3 EHs. σ_{stats} indicates the statistical uncertainty, while σ_{syst} indicates the systematic uncertainty due to the errors from the fitted function.

6.3.1.2 Estimation of N_n

Once we have the isolated muon candidates, the nGd can be obtained by applying the delayed energy cut and side-band subtraction. Figure 6.14 shows an example of the energy spectra before and after applying the cuts.

Figures 6.15 show an example of the spatial distributions of events after the delayed energy cut both in the signal and background time windows. It is obvious that almost all nGd candidates occur inside the Gd-doped liquid scintillator (as it should be), while the accidental coincidences happen around the edge of the AD.

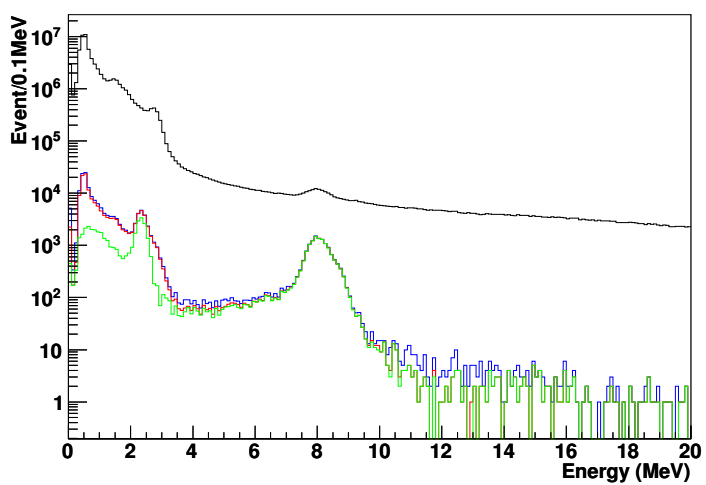
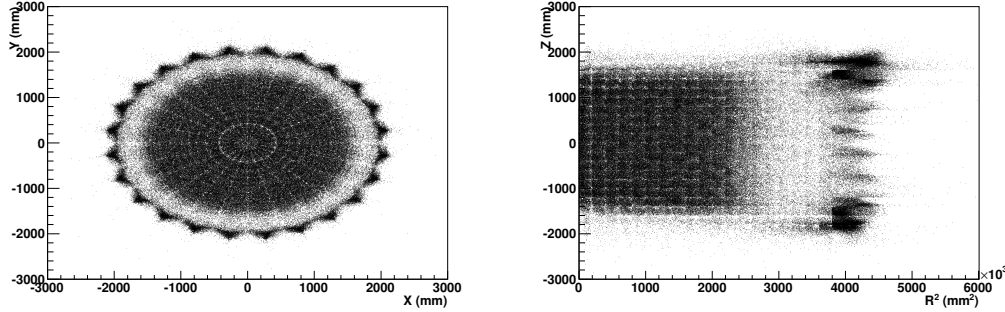
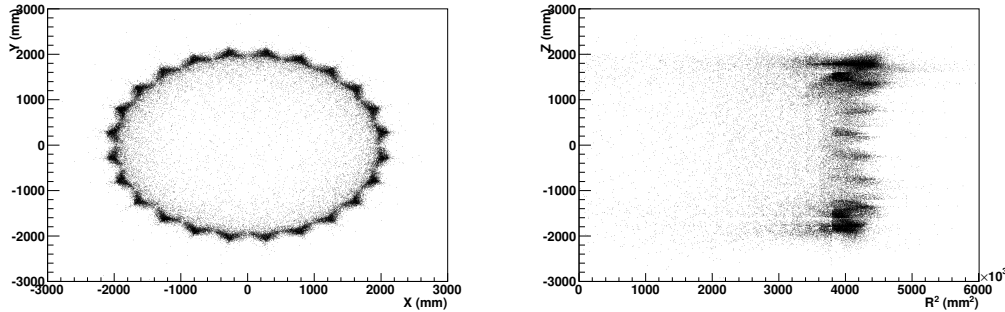


Figure 6.14: The energy spectra between 0 and 20 MeV before and after cuts in EH1-AD1. Black curve indicates the energy spectrum of all triggers; Blue curve indicates the energy spectrum for events located in the signal time window of an isolated muon; Red curve indicates the energy spectrum for events passing the the flasher removal cut; Green curve indicates the energy spectrum after the side-band subtraction.

By doing the side-band subtraction, the accidental coincidences can be removed.



(a) XY distribution in the singal time window.
(b) R^2Z distribution in the singal time window.



(c) XY distribution in the background time window.
(d) R^2Z distribution in the background time window.

Figure 6.15: The spatial distributions of the nGd candidates in the singal and background time windows.

After applying the timing and energy cuts of nGd, N_n can be obtained. The numbers of nGd candidates in ADs of the 3 EHs are shown in Table 6.4. Figure 6.16 shows an example of the energy spectrum of nGd in EH1-AD1.

6.3.1.3 The pile-up event

Figure 6.17 shows the energy spectrum in EH1-AD1 with a logarithmic scale on y axis. A small peak around 16 MeV indicates the pile-up events (double nGd): two

Detector	N_n	$\sigma_{stats.} (\%)$
EH1-AD1	1863991	0.0733
EH1-AD2	1875072	0.0730
EH2-AD1	1455265	0.0829
EH3-AD1	172877	0.2405
EH3-AD2	176308	0.2382
EH3-AD3	172272	0.2409

Table 6.4: The number of nGd candidates in the ADs of the 3 EHs. σ_{stats} indicates the statistical uncertainty.

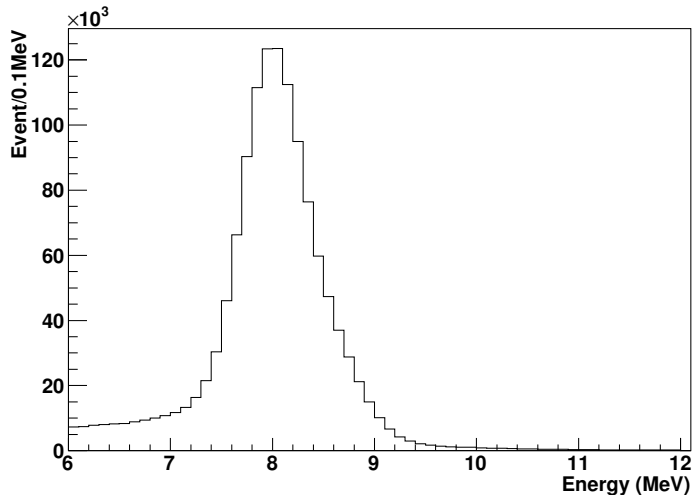


Figure 6.16: The energy spectrum of nGd after the selection cuts in EH1-AD1.

nGd accidentally occur within a readout time window ($< 1.2 \mu s$), and DAQ reads them out as a single event. By comparing the nGd and double nGd peaks, we can give the probability of double nGd $\approx 0.7\%$. We ignore the tiny difference on the measured probability of double nGd among the 6 ADs. The triple nGd peak is not observed around 24 MeV, so we ignore the triple nGd contribution.

By assuming that there are no correlation between two neutrons, we can calculate the probability of double nGd event P ,

$$P = \int_{10 \mu s}^{300 \mu s} \frac{1}{\tau} e^{-t_1/\tau} \left\{ \int_{t_1}^{t_1+1.2 \mu s} \frac{1}{\tau} e^{-t_2/\tau} dt_2 \right\} dt_1 \quad (6.11)$$

where τ is the neutron capture time constant. For EH1-AD1, we have $\tau = 30.78 \mu s$. This capture time constant leads to the probability $P \approx 1.0\%$. By varying the capture time constant from 30.78 to 30.98 μs (the range of capture time constants among 6 ADs, see Section 6.3.1.8 for details), we get a neglectable difference ($\sim 0.001\%$) on P .

Comparing the measurement and the calculation, the probability of the double nGd is obtained to be $C_p = 1.01 \pm 0.003$. This pile-up event correction factor is commonly used in 6 ADs.

6.3.1.4 The average track length

The average track length of muons crossing the GdLS volume is computed by employing both the MC and the measurement. In the MC, by analyzing those "triggered" muons as described in Section 6.2.2.2, the simulated track length X_{MC} can be calculated as shown in Figure 6.18.

The average muon track length can also be measured by using the muon deposited energy in the LS and GdLS divided by the average energy loss per unit track length [73]. The average energy loss per unit track length is estimated by a FLUKA simulation. In this standalone FLUKA simulation, muons with a realistic energy spectrum and charge ratio are tracked into a cylindrical detector filled with

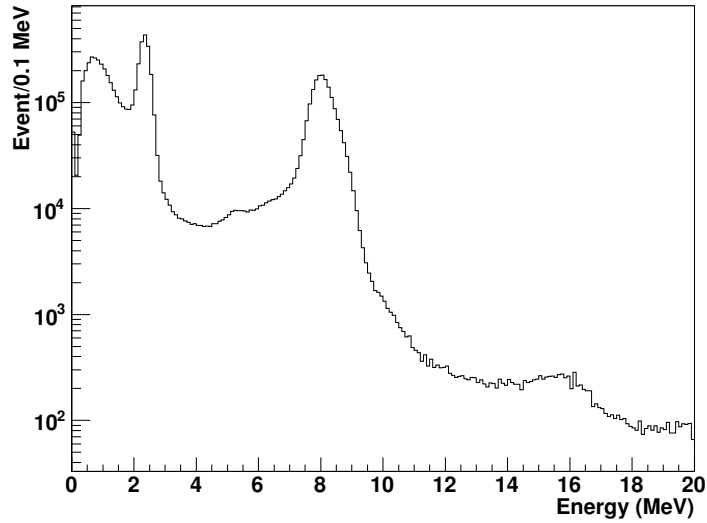


Figure 6.17: The energy spectrum in EH1-AD1 with a logarithmic scale on y axis.

GdLS. We calculate the energy loss of the i -th muon with its corresponding track length l_i . By summing over the energy loss for each muon, and dividing by the sum of track length, the average energy loss per unit track length can be calculated to be

$$\frac{dE}{dX} = \frac{\sum_i E_i}{\sum_i l_i}. \quad (6.12)$$

Table 6.6 lists the average energy loss per unit track length for cosmic-ray muons in the 3 EHs.

Site	$dE/dX(\text{MeV}/(\text{g/cm}^2))$
EH1	2.4271
EH2	2.4198
EH3	2.5071

Table 6.5: The average energy loss per unit track length for cosmic-ray muons in the 3 EHs

The measured track length X_{meas} in GdLS volume can be obtained by multi-

plying the measured total track length (LS+GdLS) by the fraction of such a length in GdLS, which is provided by the MC simulation.

Finally, we take the average of X_{MC} and X_{meas} as the muon track length across the GdLS volume, and the difference of the two lengths as the systematic uncertainty.

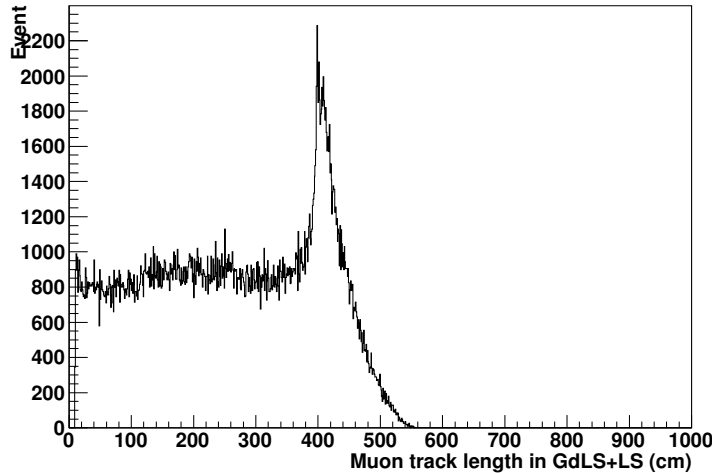


Figure 6.18: The MC simulation of muon track length in EH1-AD1.

Table 6.6 shows the average track lengths of muon in the 3 EHs.

Detector	X_{meas} (g/cm ²)	X_{MC} (g/cm ²)	X (g/cm ²)	σ_{syst} (g/cm ²)
EH1-AD1	108.38	108.67	108.52	0.14
EH1-AD2	109.57		109.12	0.45
EH2-AD1	115.37	108.67	112.02	3.35
EH3-AD1	109.16	108.69	108.93	0.23
EH3-AD2	111.27		109.98	1.29
EH3-AD3	112.39		110.54	1.84

Table 6.6: The average track lengths of muon in the 3 EHs.

6.3.1.5 Spill in/out correction factor

In this study, we are interested in counting the number of neutrons generated in GdLS. For high (kinetic) energy neutrons produced outside the target region, it is possible that these neutrons could enter into GdLS volume and get captured by Gd there. On the other hand, the energetic neutrons could also escape from the target volume. The quantities C_{in} and C_{out} are defined to describe the fractions of spill-in and spill-out respectively,

$$C_{in} = \frac{\text{Number of neutrons captured in GdLS } (N_C)}{\text{Number of neutron generated and captured in GdLS } (N_{G,C})} \quad (6.13)$$

and

$$C_{out} = \frac{\text{Number of neutrons gnerated and captured in GdLS } (N_{G,C})}{\text{Number of neutron generated in GdLS } (N_G)}. \quad (6.14)$$

By multiplying the fractions of of spill-in and spill-out, the correction factor of spill in/out is obtained,

$$C_{in/out} = C_{in} \times C_{out}. \quad (6.15)$$

As described in Section 6.2.2.2, to avoid overestimating the number of neutrons, two methods are adoped for counting the numbers N_G and N_C and calculating $C_{in/out}$. The averages of $C_{in/out}$ from two methods are used as the correction factors for spill in/out effects, $\overline{C_{in/out}}$, and the differences are treated as the systematic uncertainties. Table 6.7 shows the summary of the spill in/out correction factors in each EH.

6.3.1.6 Gd-capture ratio

The cosmic-ray muon-induced neutrons are not only captured on the Gadolinium doped in the LS, but can also be captued on other nuclei in LS, such as Hydrogen and Carbon. To calculate the muon-induced neutron production rate, it is necessary to convert the number of nGd event to the number of total neutron capture

Site	Method 1			Method 2			$\overline{C_{in/out}}$	σ_{syst}	σ_{stat}
	N_C	N_G	$C_{in/out}$	N_C	N_G	$C_{in/out}$			
EH1	55978	63245	0.8851	47058	52731	0.8924	0.8888	0.0037	0.0009
EH2	59076	67047	0.8811	50372	56254	0.89544	0.8883	0.0072	0.0009
EH3	91681	104720	0.8755	75367	85638	0.8801	0.8778	0.0023	0.0007

Table 6.7: The spill in/out correction factors in the 3 EHs. $\overline{C_{in/out}}$ denotes the spill in/out correction factor. σ_{stats} indicates the statistical uncertainty, σ_{syst} indicates the systematical uncertainty by comparing results obtained from two methods.

events in GdLS. The ratio of the former to the later is defined as ϵ_{Gd} ,

$$\epsilon_{Gd} = \frac{\text{Number of Gd-capture neurons in GdLS}}{\text{Number of captured neutrons in GdLS}}. \quad (6.16)$$

As described in Section 6.2.2.2, two methods are adopted to evaluate ϵ_{Gd} . Table 6.8 shows the results of Gd-capture efficiencies from two methods in 3 EHs. Since there are no significant differences of efficiencies among 3 EHs, we take the average of the efficiencies listed in Table 6.8 to be the central value of the Gd-capture efficiency $\epsilon_{Gd} = 85.38\% \pm 0.06\%(stat.)$. The statistical uncertainty is calculated by taking the quadratic average of the uncertainties listed in Table 6.8. By comparing the calibration source AmC simulation with spallation neutrons and AmC calibration source data, the absolute systematic uncertainty can be given as 0.81% and the relative uncertainty is 0.1% [48].

	$\epsilon_{Gd,1}$	$\sigma_{Gd,1}$	$\epsilon_{Gd,2}$	$\sigma_{Gd,2}$
EH1	0.8552	0.0015	0.8518	0.0016
EH2	0.8526	0.0015	0.8537	0.0016
EH3	0.8548	0.0012	0.8536	0.0013

Table 6.8: The Gd-capture ratio using two different methods, where ϵ_{Gd} and σ_{Gd} are Gd-capture efficiency and the associated statistical uncertainty.

6.3.1.7 Flasher cut efficiency

The efficiency of the flasher removal (See Section 5.2 for details.) is estimated by simulating nGd in the EH1-AD1. There are only 6 events identified as flasher events ($FID > 0$) out of 103036 nGd events, resulting in an efficiency 99.994% with a statistical uncertainty 0.0026%¹, as shown in Figure 6.19. The flasher inefficiency is extreme small, so we will neglect it in the later analysis.

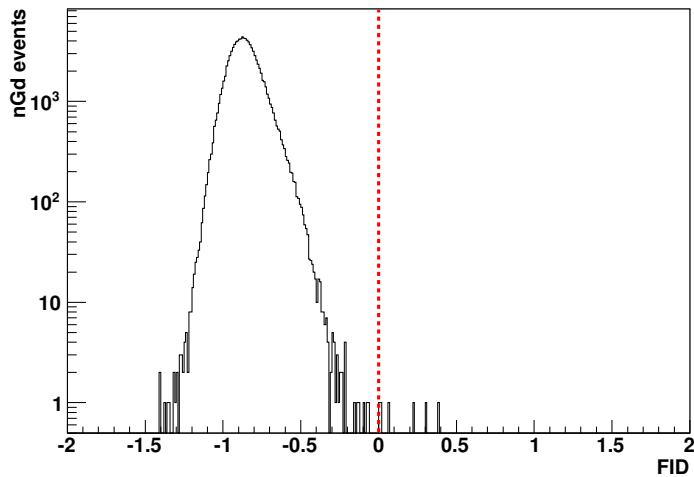


Figure 6.19: The FID distribution from the MC simulation. The red dashed vertical line indicates $FID = 0$.

6.3.1.8 Timing cut efficiency

Since the mean muon energies are different among 3 EHs, muons with higher energy could have larger probability to induce energetic neutrons. Neutrons with higher energies take more time to thermalize so that its capture time may increase. In the following subsections on timing and energy cut efficiencies, the comparison between MC and data in the same EH gives the absolute uncertainty, while the comparison of data among ADs in the same EH gives the relative uncertainty.

¹For extreme large or small efficiency, the calculation of its statistical uncertainty is described in [52]

The distributions of the time interval between prompt and delayed signal given by MC and data in EH1-AD1 are shown in Figure 6.20 and 6.21, respectively. By

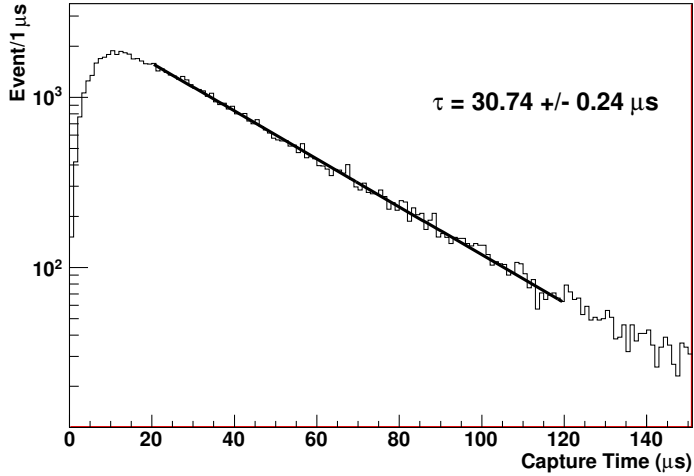


Figure 6.20: The capture time distribution in MC data.

applying the timing cut in the MC simulation, the efficiency of timing cut is then obtained,

$$\epsilon_t = 84.34\% \pm 0.17\% \text{ (stat)} \pm 0.05\% \text{ (syst)}, \quad (6.17)$$

with an assumption of 10 ns uncertainty of the trigger time. Since the uncertainty due to the 10 ns trigger time uncertainty is small enough, it will not be discussed in the later analysis. A single exponential function $f(t; \tau)$ is fitted to the capture time distribution from 20 to 120 μs ,

$$f(t; \tau) = \frac{1}{\tau} \exp(-t/\tau). \quad (6.18)$$

in which τ is the capture time constant. By comparing the capture time constant from MC and data, the difference between MC and data makes an absolute uncertainty 0.22%.

The procedure of calculating the absolute uncertainty of the timing cut effi-

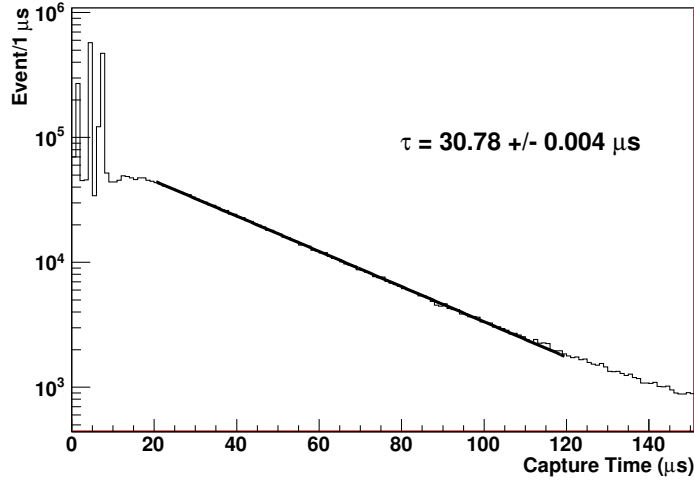


Figure 6.21: The capture time distribution in the data of EH1-AD1.

ciency is given below:

- Once we obtain the capture time constants τ_{MC} and $\tau_{EH1-AD1}$ and the corresponding errors σ_{MC} and $\sigma_{EH1-AD1}$ respectively, the difference between τ_{MC} and $\tau_{EH1-AD1}$ can be calculated as

$$\Delta = \sqrt{|\tau_{MC} - \tau_{EH1-AD1}|^2 + \sigma_{MC}^2 + \sigma_{EH1-AD1}^2}. \quad (6.19)$$

- By varying τ from $\tau_{MC} - \Delta$ to $\tau_{MC} + \Delta$ in the fit function, the integral between 10 to 300 μs would change with a relative difference $\delta = 0.26\%$.
- The absolute uncertainty can be calculated by multiplying ϵ_t by δ so that

$$\sigma_{abs_syst} = \epsilon_t \times \delta. \quad (6.20)$$

For calculating the relative uncertainty of the timing cut efficiency, a similar method is applied by comparing the capture time constants among ADs in the same EH. For EH1, the difference on capture time constant between the ADs gives a relative systematic uncertainty 0.05%.

Table 6.9 shows the summary of the time cut efficiencies and their uncertainties in the 3 EHs.

	ϵ_t	σ_{stat}	σ_{abs_syst}	σ_{rel_syst}
EH1	0.8434	0.0017	0.0022	0.0005
EH2	0.8456	0.0016	0.0023	N/A
EH3	0.8434	0.0012	0.0032	0.0016

Table 6.9: The timing cut efficiencies in the 3 EHs. σ_{stat} , σ_{abs_syst} , and σ_{rel_syst} denote the statistical, absolute systematic and relative systematic uncertainties, respectively.

Figure 6.22 shows the capture time constants in the 6 ADs.

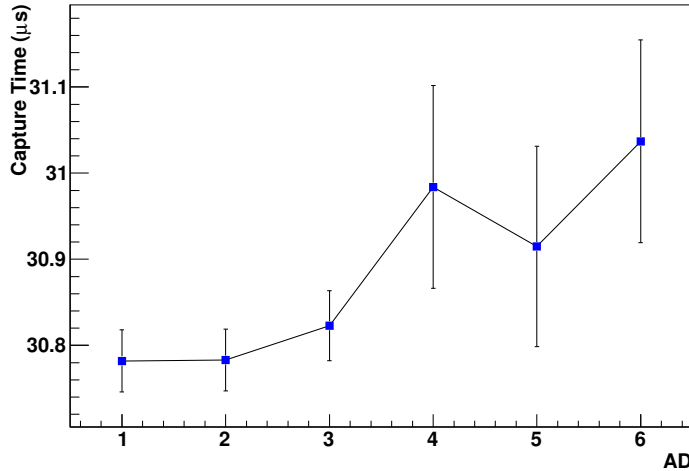


Figure 6.22: The capture time constants in the 6 ADs.

6.3.1.9 Energy cut efficiency

Details of calculating the energy cut efficiency in EH1 are presented in the following.

To get the energy cut efficiency in EH1, a simulation shows that 93763 events out of 103460 nGd pass the energy cut $6\text{MeV} < E < 12\text{MeV}$, resulting a cut

efficiency of 90.76% with a statistical uncertainty 0.09%. Before calculating the energy cut efficiency, we correct the energy spectrum of MC by shifting the peak position to align with the peak position of EH1-AD1 data. A 0.5% uncertainty on the energy scale at 6 MeV has been given in [53]. By varying the cut at 6 MeV and counting the number of nGd, we found that the 0.5% difference on the energy scale in ADs, shown in Figure 6.23, leads to a 0.14% relative uncertainty.

To determine the difference between MC and data, we calculate the ratio of events in a subset region 6-7 MeV to those in the energy region 6-12 MeV in MC and data. Assuming the same relative difference between MC and data in the 0-6 MeV region, the difference on the absolute efficiency between the MC and data are evaluated, and the largest one is taken to be the absolute systematic uncertainty, 1.99%.

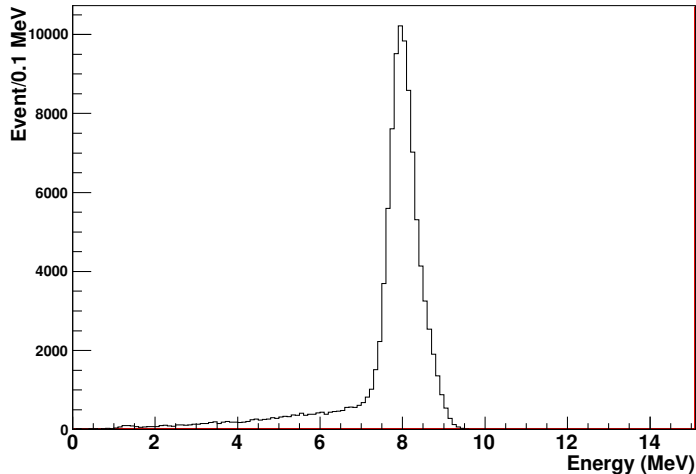


Figure 6.23: The energy spectrum of nGd in EH1 in MC.

By comparing the ratios of event in the energy range 6-7 MeV to that in 6-12 MeV among the ADs in EH1 as shown in Table 6.10, the relative uncertainty is determined to be 0.08%. The final relative uncertainty is obtained by summing up all relative uncertainties quadratically.

Detector	$N(6\text{-}7 \text{ MeV})/N(6\text{-}12 \text{ MeV})$
EH1-AD1	0.0676
EH1-AD2	0.0670

Table 6.10: The ratio of events in a subset region to that in 6-12 MeV.

Table 6.11 shows the summary of the energy cut efficiencies and uncertainties in the 3 EHs.

	ϵ_E	σ_{stat}	σ_{abs_syst}	σ_{rel_syst}
EH1	0.9076	0.0009	0.0199	0.0016
EH2	0.9092	0.0009	0.0194	N/A
EH3	0.9090	0.0011	0.0232	0.0022

Table 6.11: The energy cut efficiencies in the 3 EHs. σ_{stat} , σ_{abs_syst} , and σ_{rel_syst} denote the statistical, absolute systematic and relative systematic uncertainties, respectively.

6.3.1.10 Neutron production rate

Table 6.12 collects the measurements of N_n , N_μ , and $\langle X \rangle$, the efficiencies and the correction factors listed in Equation 6.9. The associated uncertainties are quadratic sum of the statistical and systematic uncertainties. We can calculate the neutron yield for the 6 ADs of the 3 EHs, as listed in Table 6.13.

Figure 6.24 shows the neutron yield as a function of the mean muon energy. The red curve is a parameterization resulting from FLUKA simulation [46] and the blue curve is from GEANT4 simulation [14]. By comparing with FLUKA simulation, the neutron yields are larger than simulation results by $\sim 15\%$ at near halls, while the neutron yields agree well with the simulation result at the far hall. For the comparison with GEANT4 simulation, the data are consistently larger than the simulation results by $\sim 12\%$.

	EH1		EH2		EH3			
	AD1	AD2	AD3	AD4	AD5	AD6		
DAQ live time (day)	190.9954		189.6464		189.7857			
N_μ	284262437	284207796	221364195	16480324	16582316	16489881		
$\sigma_{\mu,stat}$	16860	16858	14878	4059	4072	4060		
$\sigma_{\mu,syst}$	10867	6275	5754	2292	14939	3791		
N_n	1863991	1875072	1455265	172877	176308	172272		
$\sigma_{n,stat}$	1365	1369	1206	416	420	415		
X (cm)	108.52	109.12	112.02	108.93	109.98	110.54		
σ_X (cm)	0.14	0.45	3.35	0.23	1.29	1.84		
	EH1		EH2		EH3			
$C_{in/out}$	0.8986 ± 0.0061		0.8986 ± 0.0032		0.8884 ± 0.0084			
C_p				1.010 ± 0.003				
ϵ_{Gd}				0.8538 ± 0.0082				
ϵ_t	0.8434 ± 0.0029		0.8456 ± 0.0031		0.8434 ± 0.0038			
ϵ_E	0.908 ± 0.020		0.909 ± 0.019		0.909 ± 0.023			

Table 6.12: Summary of muon-induced neutrons in ADs in the 3 EHs.

Hall	Detector	$Y_n (\times 10^{-4} n/\mu/(g/cm^2))$	$\sigma_{stat} (\times 10^{-4})$	$\sigma_{syst} (\times 10^{-4})$
EH1	AD1	1.0506	0.0028	0.0260
	AD2	1.0513	0.0028	0.0263
EH2	AD3	1.0166	0.0026	0.0397
EH3	AD4	1.6929	0.0055	0.0475
	AD5	1.6993	0.0055	0.0516
	AD6	1.6613	0.0054	0.0541

Table 6.13: The neutron production rate in the 6 ADs of the 3 EHs. Y_n , σ_{stat} and σ_{syst} denote the neutron yield, statistical and systematic uncertainties. The uncertainties are also in unit of $n/\mu/(g/cm^2)$.

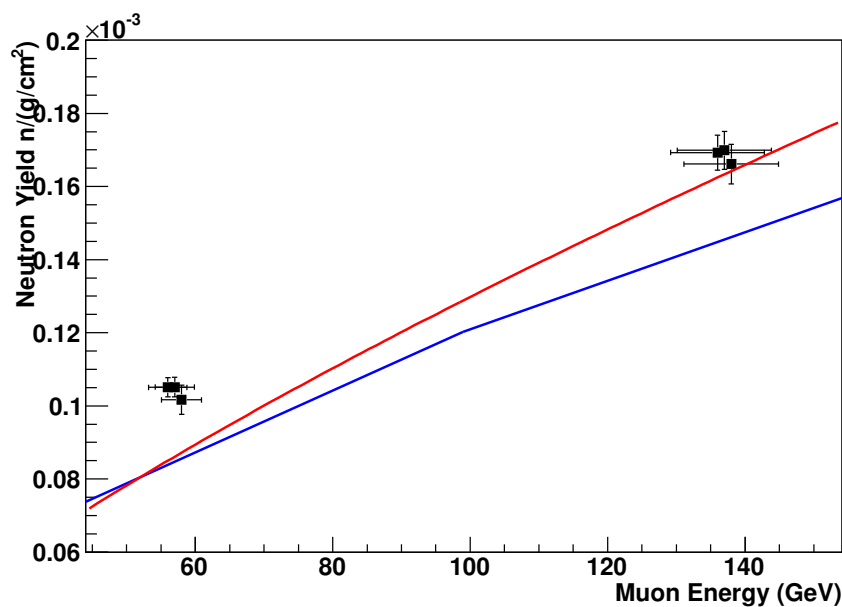


Figure 6.24: The neutron yields in 6 ADs of 3 EHs. For visual clarity, the ADs in EH1 and EH3 are separated by 1 GeV. The red curve indicates the parameterization formula obtained by FLUKA simulation [46], and the blue curve is from GEANT4 simulation [14].

6.3.2 Comparison with results from other experiments

Measurements of muon-induced neutron at different depths [65, 66, 67, 68, 69, 70, 71] including those obtained in this thesis (denoted as DYB Near and DYB Far, respectively), are depicted in Figure 6.25. The fitted function can be obtained as

$$Y_n = (7.46 \pm 1.03) \times 10^{-6} \times E_\mu^{0.64 \pm 0.03} \text{ } n/\mu/(\text{g/cm}^2), \quad (6.21)$$

with $\chi^2/NDF = 1.22$.

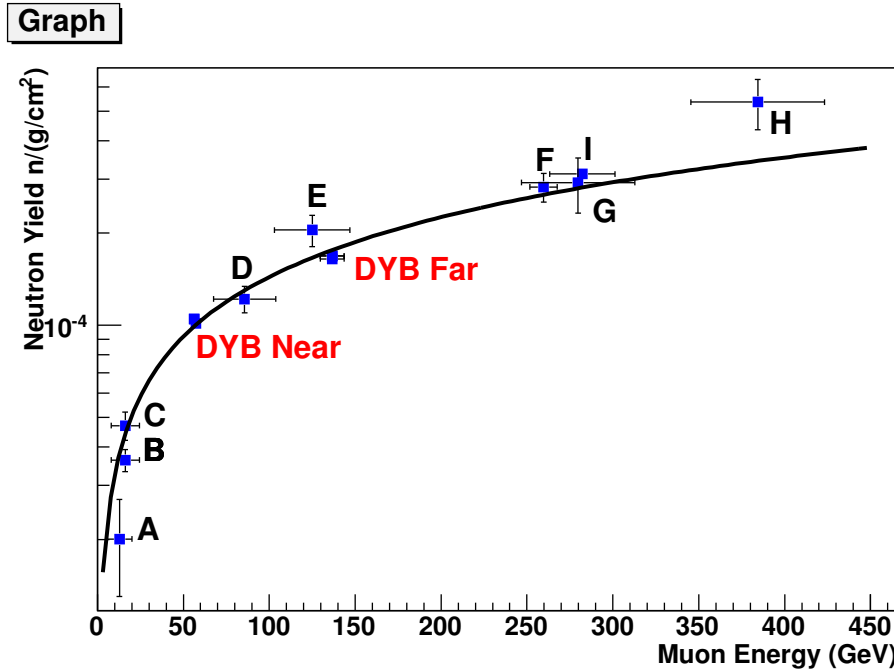


Figure 6.25: Measurement of the neutron production rate as a function of the mean muon energy. The experimental points, with abscissa corresponding to the average energy at the experiment's depth: A) 20 meter water equivalent (m.w.e.) [67], B) 32 m.w.e by the Palo Verde experiment[68] C) 25 m.w.e. [69], D) 316 m.w.e. [69], E) 570 m.w.e [70], F) 2700 m.w.e by KamLAND experiment [71], G) 3650 m.w.e. by the LVD experiment at Gran Sasso [65], H) 3800 m.w.e by the Borexino experiment at Gran Sasso [66], I) 5200 m.w.e. by the LSD detector at Mont Blanc [72] and the data points from the Daya Bay experiment. The black curve is the fitted function. Our measurements are denoted by DYB Near and DYB Far, respectively.

Chapter 7

Conclusion

We have measured the neutron production rate induced by cosmic-ray muons in the Daya Bay experiment. A semi-releastic MC simulation is performed for calculating the correction factors, the efficiencies for various cuts and their associated uncertainties. The number of detected muons is measured and the correction is applyed at the high energy region. The number of detected neutrons is measured by applying the energy and timing selection criteria. The average track length of cosmic-ray muon is estimated both by MC simulation and deposited energy of muon, and the difference of these two methods is taken to be the uncertainty. Table 7.1 shows the averaged neutron yield in the 3 EHs. By comparing with FLUKA

	Overburden	E_μ	Y_n
EH1	250	57	$(1.0510 \pm 0.0026) \times 10^{-4}$
EH2	265	58	$(1.0166 \pm 0.0033) \times 10^{-4}$
EH3	860	137	$(1.6845 \pm 0.0054) \times 10^{-4}$

Table 7.1: Summary of the neutron yield in the 3 EHs where the overburden is given in the unit of m w.e., the average energy of muon E_μ is given in the unit of GeV and the neutron yield is given in the unit of $n/\mu/(\text{g/cm})^2$.

simulation, the neutron yields are larger than simulation results by $\sim 15\%$ at near halls, while the neutron yields agree well with the simulation result at the far hall.

For the comparison with GEANT4 simulation, the data are consistently larger than the simulation results by $\sim 12\%$. The neutron production rate as a function of the mean muon energy can be parameterized by fitting experimental data with different overburdens [65, 66, 67, 68, 69, 70, 71] and the data points from the Daya Bay experiment presented in this thesis. We obtain

$$Y_n = (7.46 \pm 1.03) \times 10^{-6} \times E_\mu^{0.64 \pm 0.03} \text{ n}/\mu/\text{(g/cm}^2\text{)}, \quad (7.1)$$

with $\chi^2/NDF = 1.22$.

Bibliography

- [1] F. A. Scott, Phys. Rev. **48**, 391, (1935).
- [2] W. Pauli, letter to physicist's gattering at Tubingen, December 4, 1930, reprinted in *Inward Bound* by Paris, Oxford University Pres, p. 315.
- [3] Y. Ashie *et al.* [Super-Kamiokande Collaboration], Phys. Rev. D **71**, 112005 (2005) [arXiv:hep-ex/0501064].
- [4] Y. Ashie *et al.* [Super-Kamiokande Collaboration], Phys. Rev. Lett. **93**, 101801 (2004) [arXiv:hep-ex/0404034].
- [5] E. Aliu *et al.* [K2K Collaboration], Phys. Rev. Lett. **94**, 081802 (2005) [arXiv:hep-ex/0411038].
- [6] M. H. Ahn *et al.* [K2K Collaboration], Phys. Rev. D **74**, 072003 (2006) [arXiv:hep-ex/0606032].
- [7] K. Eguchi *et al.* [KamLAND Collaboration], Phys. Rev. Lett. **90**, 021802 (2003) [arXiv:hep-ex/0212021].
- [8] T. Araki *et al.* [KamLAND Collaboration], Phys. Rev. Lett. **94**, 081801 (2005) [arXiv:hep-ex/0406035].
- [9] X. Guo *et al.* [Daya Bay Collaboration], arXiv:hep-ex/0701029.
- [10] A. Ferrari, P. R. Sala, A. Fasso and J. Ranft, “FLUKA: A multi-particle transport code (Program version 2005),”

- [11] Y. F. Wang, V. Balic, G. Gratta, A. Fasso, S. Roesler and A. Ferrari, Phys. Rev. D **64**, 013012 (2001) [arXiv:hep-ex/0101049].
- [12] V. N. Ivanchenko [Geant4 Collaboration], Nucl. Instrum. Meth. A **502**, 666 (2003).
- [13] T. Mahmood, A. A. Zafar, T. Hussain and H. Rashid, AIP Conf. Proc. **888**, 301 (2007).
- [14] H. M. Araujo, V. A. Kudryavtsev, N. J. C. Spooner and T. J. Sumner, Nucl. Instrum. Meth. A **545**, 398 (2005) [arXiv:hep-ex/0411026].
- [15] M. Apollonio *et al.* [CHOOZ Collaboration], Eur. Phys. J. C **27**, 331 (2003) [hep-ex/0301017].
- [16] F. Boehm *et al.* (Palo Verde), Phys. Rev. **D64**, 112001 (2001), hep-ex/0107009.
- [17] Soo-Bong Kim *et al.* (RENO), Phys. Rev. Lett. **108**, 191802 (2012), arXiv:1204.0626 [hep-ex].
- [18] K. Abe *et al.* (T2K), Phys. Rev. Lett. **107**, 041801 (2011), arXiv:1106.2822 [hep-ex].
- [19] Y. Abe *et al.* (DOUBLE-CHOOZ), Phys. Rev. Lett. **108**, 131801 (2012), arXiv:1112.6353 [hep-ex].
- [20] B. Pontecorvo, Sov. Phys. JETP, 6, 429, 1957.
- [21] Z. Maki, M. Nakagawa, and S. Sakata, Prog. Theor. Phys., 28, 870, 1962.
- [22] F. P. An *et al.* [DAYA-BAY Collaboration], Phys. Rev. Lett. **108**, 171803 (2012) [arXiv:1203.1669 [hep-ex]].
- [23] F. Reines, C. L. Cowan, F. B. Harrison, A. D. McGuire, and H. W. Kruse, Phys. Rev., 117, 159–173, 1960.

- [24] G. Danby *et al.*, Phys. Rev. Lett., 9, 36–44, 1962.
- [25] K. Kodama *et al.* [DONUT Collaboration], Phys. Lett. B **504**, 218 (2001) [hep-ex/0012035].
- [26] B. T. Cleveland *et al.*, Astrophys. J., 496, 505–526, 1998.
- [27] Q. R. Ahmad *et al.*, Phys. Rev. Lett., 89, 011301, 2002, nucl-ex/0204008.
- [28] S. Hatakeyama *et al.* [Kamiokande Collaboration], Phys. Rev. Lett. **81**, 2016 (1998) [hep-ex/9806038].
- [29] R. Clark *et al.*, Phys. Rev. Lett., 79, 345–348, 1997.
- [30] B. Aharmim *et al.* [SNO Collaboration], Phys. Rev. C **81**, 055504 (2010) [arXiv:0910.2984 [nucl-ex]].
- [31] P. Adamson *et al.* [MINOS Collaboration], Phys. Rev. Lett. **106**, 181801 (2011) [arXiv:1103.0340 [hep-ex]].
- [32] Abe S *et al.* (KamLAND collaboration). Phys. Rev. Lett., 2008, 100: 221803
- [33] X. Guo *et al.* [Daya-Bay Collaboration], hep-ex/0701029.
- [34] C. Gaspar, M. Dönszelmann, Ph. Charpentier, DIM, a portable, light weight package for information publishing, data transfer and inter-process communication, Computer Physics Communications, Volume 140, Issues 1–2, 15 October 2001, Pages 102–109
- [35] <http://www.mysql.com/>
- [36] A. Valassi et al., LCG Persistency Framework (CORAL, COOL, POOL): Status and Outlook, CHEP 2010, Taipei, <http://iopscience.iop.org/1742-6596/331/4/042043>

- [37] P. Jenni, M. Nessi, M. Nordberg and K. Smith, ATLAS high-level trigger, data-acquisition and controls : Technical Design Report, ATLAS-TDR-16, 2003
- [38] <http://www.timesys.com/embedded-linux/linuxlink>
- [39] Z. Yu, PMT Gain Calibration TechNote, Daya Bay Doc-7093, 2012.
- [40] Z. Wang, RollingGain Not, Daya Bay, Doc-7198, 2011.
- [41] E. H. Bellamy et al., Absolute calibration and monitoring of a spectrometric channel using a photomultiplier, Nucl. Instrum. Meth. A bf 339, 468, 1994
- [42] L. Wen et al, Summary of Flasher Events Rejection, Daya Bay Doc-7434, 2012
- [43] Formaggio J.A., Martoff C.J., Annu. Rev. Nucl. Part. Sci., 54, 361, 2004
- [44] P. Adamson *et al.* [MINOS Collaboration], Phys. Rev. D **76**, 052003 (2007) [arXiv:0705.3815 [hep-ex]].
- [45] F. P. An *et al.* [Daya Bay Collaboration], Chin. Phys. C **37**, 011001 (2013) [arXiv:1210.6327 [hep-ex]].
- [46] D. Mei and A. Hime, Phys. Rev. D **73**, 053004 (2006) [astro-ph/0512125].
- [47] Z. Wang, Muon and cosmogenic background generator, MuonPhophet, Daya Bay Doc-4153, 2009.
- [48] Guofu, Cao, A cross check for H/Gd ratio, Daya Bay Doc-7730, 2012.
- [49] W. Q. Jiang et al., Chinese Physics C 36, (2012) 235-240; S. Jetter et al., Chinese Physics C 36, (2012) 733-741.
- [50] V. A. Kudryavtsev, N. J. C. Spooner and J. E. McMillan, Nucl. Instrum. Meth. A **505**, 688 (2003) [hep-ex/0303007].

- [51] Thomas K. Gaisser, Cosmic Rayr and Particle Physics, p. 77, Cambridge University Press, 1990.
- [52] T. Ullrich and Z. Xu, arXiv:physics/0701199v1
- [53] F. P. An et al. (Daya Bay Collaboration), Nucl. Instr. and Meth. A 685, 78 (2012).
- [54] V. A. Kudryavtsev, Muon simulation codes MUSIC and MUSUN for underground physics, arXiv:physics/0810.4635
- [55] CORSIKA (COsmic Ray SImulations for KAscade) is a physics computer software for simulation of extensive air showers induced by high energy cosmic rays, <http://www-ik.fzk.de/corsika/>
- [56] R. W. Hackenburg, The Muon System of the Daya Bay Reactor Antineutrino Experiment, Daya Bay Doc-7795, 2013.
- [57] Jilei Xu, personal communication.
- [58] A. Empl, R. Jasim, Ed Hungerford and P. Mosteiro, (2012), arXiv:1210.2708.
- [59] A. Fassò and A. Ferrari and J. Ranft and P. R. Sala, Proceedings of the MonteCarlo 2000 Conference, Lisbon , 159 (2001).
- [60] A. Fassò and A. Ferrari and J. Ranft and P. R. Sala, Proceedings of the "Specialists' Meeting on Shielding Aspects of Accelerators, Targets & Irradiation Facilities, Arlington" (1995).
- [61] A. Ferrari and and P. R. Sala, Proceedings of Workshop on Nuclear Reaction Data and Nuclear Reactors Physics, Design and Safety, Trieste (1998).
- [62] G. Battistoni and others, Proceedings of 11th International Conference on Nuclear Reaction Mechanism, Varenna (2006).

- [63] M. Brugger, A. Ferrari, S. Roesler, and L. Ulrici, NIM in Physics Research A562, 814 (2006).
- [64] N. Y. Agafonova and A. S. Malgin, arXiv:1304.0919 [nucl-ex].
- [65] LVD Collaboration, R. Persiani, poster at the Workshop in Low Radioactivity Techniques LRT 2013, LNGS Assergi (AQ), Italy, April 10-12, (2013).
- [66] G. Bellini *et al.* [Borexino Collaboration], arXiv:1304.7381 [physics.ins-det].
- [67] R. Hertenberger, M. Chen, and B. L. Dougherty, Phys.Rev. C 52, 3449 (1995).
- [68] F. Boehm *et al.*, Phys. Rev. D. 62(2000) 092005.
- [69] L. B. Bezrukov *et al.*, Sov. J. Nucl. Phys. 17, 51 (1973).
- [70] R. I. Enikeev *et al.*, Sov. J. Nucl. Phys. 46, 1492 (1987).
- [71] S. Abe *et al.*, Phys. Rev. C 81, 025807 (2010).
- [72] M. Aglietta *et al.*, Nuovo Cimento C 12, 467 (1989).
- [73] Dong-Ming Mei, PhD thesis, University of Alabama, 2003.